

Dissertation  
submitted to the  
Combined Faculties for the Natural Sciences and for Mathematics  
of the Ruperto-Carola University of Heidelberg, Germany  
for the degree of  
Doctor of Natural Sciences

presented by  
M.Sc. Mol. Biotechnology Henning Johannes Falk  
born in Alsfeld  
Oral examination: 11th of April, 2018



**IMAGING THE ONSET OF THE  
SEGMENTATION CLOCK DURING  
MOUSE GASTRULATION**

Referees: Dr. François Spitz  
Prof. Dr. Christof Niehrs



# Abstract

A fundamental requirement for embryonic development is tight spatiotemporal coordination between a steadily increasing number of cells. A notable example of highly coordinated cellular activity occurs during body axis segmentation of the vertebrate embryo. Organized oscillatory signaling activity produces regular waves of gene expression that traverse the tissue. These oscillations are thought to define the timing of segmentation and the positioning of embryonic segments, the somites. The striking rhythmicity of the process is ascribed to a molecular oscillator in undifferentiated cells, the “segmentation clock”, involving the Notch, Wnt and FGF signaling pathways in mouse. While the segmentation clock and its intercellular coordination mechanism have been studied in some detail, the start of the process, the establishment of an initial synchrony between several hundreds of presomitic cells, remains largely unknown.

I chose a live imaging approach to examine the onset of synchronous signaling oscillations in the developing embryo. To this end, I established a mounting and culture method to enable long-term multi-sample post-implantation mouse embryo imaging on a light-sheet microscope. This new setup enables routine embryo culture and imaging from early gastrulation on embryonic day 6.5 for up to two days, closely recapitulating *in utero* development. Using genetically encoded signaling reporters to visualize the cellular oscillation status, I was able to capture the very first observable coherent oscillations of the cyclic gene *Lfng* as well as the preceding dynamics. I found concurrent upregulation of *Lfng* expression across nascent mesoderm and the primitive streak at mid gastrulation, marking the first synchronous activity pattern of this segmentation clock gene. This expression pulse was also seen for the FGF signaling target *Dusp4* but not the Wnt target *Axin2*. Despite *Lfng* being a Notch signaling target in the context of somitogenesis, I found the *Lfng* pulse to occur in the presence of Notch signaling inhibitor DAPT as well as in the absence of Notch transcription factor RBP-J  $\kappa$  and the Notch signaling core oscillator HES7. These findings argue for an initial synchronization signal independent of the Notch pathway. Quantification of early wave dynamics identified a gradual buildup of phase waves and revealed that a period gradient, which is present from the very first observable oscillation onwards, functionally underlies the establishment of waves in the gastrulating embryo.

Taken together, this study provides detailed and quantitative insight into the dynamics of the early segmentation clock in the mouse embryo, pioneering future studies on the molecular mechanism of the synchronization process. The post-implantation embryo culture and imaging method described here opens up new possibilities for the study of the gastrulation-to-organogenesis stages, which in the past have been difficult to follow in real time. Further technical developments of multi-sample mammalian embryo microscopy, which I also discuss in this work, will continue to make an important contribution to the investigation of the establishment of the segmentation clock, and beyond can help to better understand many aspects of mammalian embryonic development.

# Zusammenfassung

Für die erfolgreiche Entwicklung eines Embryos ist die Koordination einzelner Zellen im Kontext des Gesamtorganismus entscheidend. Ein eindruckliches Beispiel dafür liefert die Somitogenese bei Vertebraten. Dieser entwicklungsbiologische Prozess, bei dem die Körperachse eines Embryos in einzelne Segmente gegliedert wird, ist von gleichmäßigen Genexpressionswellen begleitet. Diese wandern durch das undifferenzierte Gewebe und sind für die Positionierung von Segmenten und für den zeitlichen Ablauf der Somitogenese verantwortlich. Als Taktgeber dieses äußerst rhythmischen Vorgangs fungiert auf zellulärer Ebene ein Netzwerk molekularer Oszillatoren, die „Segmentierungsuhr“. In der Maus ist dieses Netzwerk sowohl aus Komponenten des Notch-, als auch des Wnt- und FGF-Signalwegs aufgebaut. Eine Reihe von Studien hat sich bereits mit der zellulären Segmentierungsuhr, sowie mit dem interzellulären Kommunikationsmechanismus befasst. Wenig ist allerdings darüber bekannt, wie hunderte von Zellen zu Beginn des Segmentierungsprozesses ihre Genexpression synchronisieren und die ersten Oszillationen initiieren.

Um dieser Frage auf den Grund zu gehen, habe ich eine Methode entwickelt, die es erlaubt Mausembryonen nach der Nidation für längere Zeit bei weitgehend ungestörter Entwicklung zu mikroskopieren. Dazu habe ich die Kulturbedingungen und die Probenaufhängung an einem Lichtblattnikroskop auf die Bedürfnisse der Embryonen angepasst. Die Methode gestattet nun eine zuverlässige Observation von Embryonen beginnend von Tag 6.5 der Embryonalentwicklung über die Dauer von bis zu zwei Tagen. Mit genetisch kodierten Fluoreszenzreportern, die es ermöglichen die Signalisierungsaktivitäten der Zellen zu visualisieren, konnte ich die ersten erkennbaren Oszillationen des zyklisch exprimierten Gens *Lfng*, wie auch die dynamische Entwicklung vor dieser ersten Welle im lebenden Embryo beobachten. Zu den wichtigsten Erkenntnissen dieser Studie zählt die Entdeckung des ersten synchronen Expressionsmusters von *Lfng* vor der ersten Welle: Zellen des neu gebildeten Mesoderms und des Primitivstreifens erhöhen gleichzeitig ihre Expressionsaktivität in einer Art Puls, welcher auch im Expressionsprofil von *Dusp4*, einem Zielgen des FGF-Signalwegs, zu sehen ist. Im Gegensatz dazu zeigt *Axin2*, Teil der Wnt-Signalkette, keine vergleichbare Dynamik. Obwohl *Lfng* während der Somitogenese durch den Notch-Signalweg kontrolliert wird, stellte sich

heraus, dass der Puls auch dann auftrat, wenn der Signalweg durch die Gabe des Inhibitors DAPT blockiert wurde. Auch die genetische Unterbrechung der Notch-Signalkette durch Ausschalten des Transkriptionsfaktors *Rbp-jk*, sowie des *Hes7*-Gens, welches für die Generierung der Oszillationen verantwortlich gemacht wird, hatte keinen offensichtlichen Einfluss auf den *Lfng*-Puls. In der Summe legen diese Resultate daher nahe, dass die initiale Synchronisation einzelner Zellen im Mausembryo unabhängig von Notch-Signalen abläuft. Weiterhin konnte durch quantitative Analyse der Wellendynamik der graduelle Aufbau von Phasenwellen beschrieben werden. Als Grund für die Entstehung von Wellen konnte ein Periodengradient identifiziert werden, der bereits mit der ersten erkennbaren Welle auftrat.

Zusammenfassend lässt sich festhalten, dass die hier vorliegende Studie einen detaillierten Einblick in die Dynamiken um den Start der Segmentierungsuhr gewährt und somit den Grundstein für weitergehende Forschung zu diesem Thema legt. Die hier vorgestellte Technik zur Langzeitmikroskopie von Mausembryonen eröffnet neue Möglichkeiten zur detaillierten Studie entwicklungsbiologischer Aspekte im bisher für Lebendmikroskopie wenig zugänglichen Zeitraum der Gastrulation. Technische Weiterentwicklungen der Embryonenmikroskopie, wie ich sie ebenfalls in dieser Arbeit beschreibe, werden sowohl zum Thema der Etablierung der Segmentierungsuhr als auch darüber hinaus einen wichtigen Beitrag zu unserem Verständnis der Säugetierembryonalentwicklung leisten.



# Contents

<b>Abbreviations</b> .....	<b>III</b>
<b>Figures</b> .....	<b>IV</b>
<b>Introduction</b> .....	<b>1</b>
<b>1. Light-sheet microscopy in developmental biology</b> .....	<b>3</b>
1.1 Basic principles of light-sheet microscopy .....	4
1.2 Light-sheet imaging of mammalian embryos .....	8
<b>2. Gastrulation of the vertebrate embryo</b> .....	<b>11</b>
<b>3. Signaling dynamics in somitogenesis</b> .....	<b>14</b>
3.1 Somitogenesis .....	14
3.2 A model for clock-based segmentation.....	15
3.3 Topology of the mouse oscillator .....	18
3.4 Signaling gradients and the wavefront.....	21
3.5 Oscillation synchronization across the tissue .....	22
3.6 The making of waves .....	24
3.7 Alternative segmentation models.....	26
3.8 Initiation of the segmentation clock.....	27
<b>4. Aims of the study</b> .....	<b>32</b>
<b>Chapter I   A toolkit for early post-implantation mouse imaging</b> .....	<b>35</b>
<b>1. Results</b> .....	<b>36</b>
1.1 Customized mounting and culture protocol for long-term imaging of the mouse gastrula.....	36
1.2 Multi-sample imaging with SPIMfor4.....	38
1.3 Single-cell tracking in the embryo with mosaic labeling.....	40
<b>2. Discussion</b> .....	<b>43</b>
2.1 Updating a commercial light-sheet microscope for mouse embryos.....	43
2.2 Tracking of sparsely labeled cells and its application .....	45
2.3 Outlook: multi-embryo multi-angle post-implantation imaging.....	46
<b>Chapter II   Prelude to somitogenesis: start of the segmentation clock</b> .....	<b>51</b>
<b>1. Results</b> .....	<b>52</b>
1.1 <i>Lfng</i> expression from gastrulation onset to formation of the first waves .....	52
1.2 First somites and early wave dynamics .....	56
1.3 Spatial and temporal pattern of the pre-segment pulse.....	59
1.4 Disruption of Notch signaling in the context of initial synchronization.....	61

1.5	Activity of <i>Dusp4</i> and <i>Axin2</i> during pre-segment stage .....	65
1.6	Gradients and waves—what comes first? .....	69
<b>2.</b>	<b>Discussion .....</b>	<b>71</b>
2.1	Comparison of early Notch signaling patterns in mouse, fish and chick.....	71
2.2	Spatiotemporal patterns preceding segmentation .....	72
2.3	<i>Lfng</i> activation during the pre-segment pulse .....	75
2.4	Early oscillations in the absence of RBP-J $\kappa$ .....	77
2.5	The onset of synchrony .....	78
	<b>Conclusion.....</b>	<b>83</b>
	<b>Materials and methods.....</b>	<b>87</b>
<b>1.</b>	<b>Animals .....</b>	<b>87</b>
1.1	Mouse lines .....	87
1.2	Genotyping.....	88
<b>2.</b>	<b>Embryo methods.....</b>	<b>89</b>
2.1	Embryo dissection and mounting for live imaging.....	89
2.2	Rotating bottle embryo culture .....	90
2.3	DAPT treatment experiments .....	90
2.4	<i>In situ</i> hybridization .....	90
<b>3.</b>	<b>Embryo culture system on the Z.1.....</b>	<b>91</b>
<b>4.</b>	<b>Light-sheet imaging .....</b>	<b>93</b>
<b>5.</b>	<b>Data analysis .....</b>	<b>94</b>
5.1	Time series registration and embryo segmentation .....	95
5.2	Expression and oscillation dynamics .....	96
<b>6.</b>	<b>Mosaic labeling and single cell tracking .....</b>	<b>100</b>
	<b>Acknowledgements.....</b>	<b>101</b>
	<b>Supplementary movies.....</b>	<b>103</b>
	<b>Bibliography.....</b>	<b>105</b>

## Abbreviations

<b>OB</b>	no allantois bud
<b>AVE</b>	anterior visceral endoderm
<b>DSL</b>	digital scanned laser light-sheet fluorescence microscopy
<b>E</b>	embryonic day
<b>EB</b>	early allantois bud
<b>EHF</b>	early head fold
<b>ES</b>	early streak
<b>FEP</b>	fluorinated ethylene propylene
<b>hpf</b>	hours post fertilization
<b>ID</b>	inner diameter
<b>IQR</b>	interquartile range
<b>ISH</b>	<i>in situ</i> hybridization
<b>LB</b>	late allantois bud
<b>LHF</b>	late head fold
<b>LOWESS</b>	locally weighted scatter plot smoothing
<b>LS</b>	late streak
<b>MEMO</b>	multi-embryo multi-orientation
<b>MIP</b>	maximum intensity projection
<b>MS</b>	mid streak
<b>NA</b>	numerical aperture
<b>NLS</b>	nuclear localization signal
<b>OD</b>	outer diameter
<b>PS</b>	primitive streak
<b>PSF</b>	point spread function
<b>PSM</b>	presomitic mesoderm
<b>RA</b>	retinoic acid
<b>SPIM</b>	selective plane illumination microscopy
<b>VE</b>	visceral endoderm

## Figures

Fig. 1: The basics of light-sheet microscopy.....	7
Fig. 2: Light-sheet imaging of post-implantation mouse development. ....	10
Fig. 3: Gastrulation of the mouse embryo. ....	13
Fig. 4: Segmentation and resegmentation of the vertebrate body axis. ....	15
Fig. 5: Waves of <i>HAIRY1</i> expression in the chick PSM.....	17
Fig. 6: Oscillatory signaling networks in the mouse PSM.....	21
Fig. 7: Period distribution in the PSM. ....	25
Fig. 8: First clock-gene oscillations in chick and fish. ....	31
Fig. 9: Optimization of light-sheet microscopy for multi-sample live imaging of mouse embryos from gastrulation to organogenesis. ....	39
Fig. 10: Tracking of sparsely labeled cells in the post-implantation embryo. ....	42
Fig. 11: The MEMO sample holder concept for light-sheet imaging.....	48
Fig. 12: LuVeLu expression patterns during gastrulation. ....	54
Fig. 13: Validation of <i>Lfng</i> expression dynamics. ....	55
Fig. 14: Characteristics of the first waves and somite boundaries.....	58
Fig. 15: Temporal and spatial structure of the pulse.....	60
Fig. 16: LuVeLu dynamics in <i>Hes7</i> -null background. ....	63
Fig. 17: Disruption of Notch signaling during pre-segment and early segment stages. ....	64
Fig. 18: Comparison of <i>Dusp4</i> and <i>Lfng</i> expression dynamics during pre-segment and early segment stages. ....	67
Fig. 19: Comparison of <i>Axin2</i> and <i>Lfng</i> expression dynamics during pre-segment and early segment stages. ....	68
Fig. 20: <i>Dusp4</i> gradient build-up during pre-segment and segment stages.....	70
Fig. 21: Summarizing the start of the segmentation clock.....	74
Fig. 22: Alternative models explaining early <i>Lfng</i> activity in the context of disrupted Notch signaling. ....	81

# Introduction

What does it take to understand communication? Let us imagine we want to follow the conversation of two colleagues in the hallway. Since it is a busy day, we only pass by occasionally when we cross the hallway to get from the office into the laboratory. How much of the information content of the conversation would we be able to gather? We would know qualitatively, there *was* communication, we could also name the two colleagues that were involved, and maybe roughly the duration of the chat. However, the actual content would be lost to us due to our busy day and our poor time sampling rate.

To decipher a high content signal, it needs an adequately high temporal resolution. This is not only true for verbal exchanges but also for intercellular communication *via* molecular interactions. An increasing number of examples demonstrates that cellular signaling has several layers of information encoding beyond the static view of integrated absolute levels. Experiments indicate that discrete cellular responses can be provoked by the dynamic properties of an incoming signal such as delay, duration, fold-change or frequency (reviewed in Sonnen and Aulehla, 2014).

During embryonic development, when cell fate decisions have to be tightly coordinated in space and time across an entire organism, the need for extensive communication between cells and tissues is especially perceptible. We are only beginning to decipher the

dynamic levels of this organization beyond the classic picture of long-range signaling gradients and local lateral inhibition patterns. To monitor and appreciate the dynamics of cellular signaling, techniques allowing for high sensitivity and high temporal frequency sampling, such as live fluorescence microscopy, are of critical importance.

The aim of the work presented in this thesis is to shine a light on the very beginning of the highly dynamic and extremely well-coordinated cellular mechanisms underlying the rhythmic patterning of the vertebrate body axis during the process of somitogenesis. I describe the onset of synchronized signaling dynamics preceding somitogenesis during mouse embryo gastrulation using genetically encoded signaling reporters. To this end, I developed a customized culture and mounting system for light-sheet microscopy to enable long-term observation of signaling dynamics in the developing organism.

The following introductory sections aim to give an overview of the technical and biological background of this study. I will start with the basics of light-sheet microscopy and its application in developmental biology. I will then review the state of research on somitogenesis and its underlying molecular signaling dynamics.

# 1. Light-sheet microscopy in developmental biology

Fluorescence microscopy in concert with genetically encoded reporters is a powerful tool for biological imaging in space and time. However, live microscopy of developmental processes in intact organisms imposes special requirements on the imaging system. Compared to cultured cells, developing organisms often have complex three-dimensional shapes and may be several millimeters in size, like a zebrafish larva or an *Arabidopsis thaliana* seedling. This requires special specimen mounting strategies, large fields of view and good axial sampling capacity. Further, the temporal scale of developmental processes may be in the range of milliseconds, as for neuronal activity recordings with calcium sensors (Chhetri et al., 2015), or the beating of an embryo's heart (Arrenberg et al., 2010; Mickoleit et al., 2014). The imaging system therefore has to be able to acquire large 3D image volumes at very high temporal resolution, often over a long period of time. Finally, any observation technique should be minimally harmful to the process of interest. Thus, in many time-lapse imaging applications in developmental biology the most crucial constrain is the need to keep phototoxicity at a dose the specimen can tolerate despite high frame rate, fine 3D sampling and long experiment duration.

Light-sheet fluorescence microscopy has emerged in the last 20 years as a powerful technique for imaging of developmental processes because it can deliver high frame rates with large fields of view and good optical sectioning at relatively low light doses. The basic technique was pioneered by Zsigmondy and Siedentopf already at the beginning of the 20<sup>th</sup> century for examining colloidal suspensions (Siedentopf and Zsigmondy, 1902). 90 years later, Voie and colleagues developed the first light-sheet setup for fluorescence imaging in biological specimens (Voie et al., 1993). Ernst Stelzer's laboratory finally introduced light-sheet microscopy to developmental biology,

demonstrating 3D time-lapse imaging of living *Drosophila* embryos (Huisken et al., 2004).

## 1.1 Basic principles of light-sheet microscopy

The basic concept of light-sheet microscopy is to separate illumination and detection paths such that they are essentially perpendicular to each other. Both paths overlap in the focal plane of the detection objective where the sample is placed (Fig. 1A). The illumination beam is shaped as a flat sheet, intended to excite fluorophores only in one plane of the specimen at a given instance. The light-sheet is either made using a cylindrical lens in the illumination beam path that focuses light along one axis, or a focused Gaussian laser beam that is scanned along one direction to generate a “virtual” light-sheet (Fig. 1B). The implementation with a static light-sheet is known as selective plane illumination microscopy (SPIM; Huisken et al., 2004), while digital scanned laser light-sheet fluorescence microscopy (DSLM) refers to techniques using a scanned light-sheet (Keller et al., 2008). However, SPIM has found use as general synonym for light-sheet microscopy and will be used as such later in this work as well.

What is the advantage of using decoupled beam paths for illumination and detection compared to a conventional epifluorescence setup? In widefield, confocal or multiphoton epifluorescence microscopes, one lens is used for excitation and fluorescence detection. This means that as the excitation light passes through the sample, it excites fluorophores in each plane along the optical axis. The confocal microscope performs optical sectioning by discriminating out-of-focus light with a pinhole, thereby still exciting the entire specimen but discarding most of the fluorescence coming from out-of-focus planes (Fig. 1C). Decoupling of excitation and detection in light-sheet microscopy, in contrast, allows for optical sectioning on the excitation side as only the plane of interest is illuminated (Fig. 1C). This way an *in toto* imaged sample is exposed to 2–3 orders of magnitude less light energy compared to the same sample being imaged on a confocal microscope with comparable resolution (Keller et al., 2008).

Further, in light-sheet microscopy out-of-focus light is prevented by selective illumination, such that detection can be parallelized with a camera (Greger et al., 2007), allow-



ing frame rates in the range of 100 Hz with latest scientific complementary metal-oxide semiconductor (sCMOS) camera technology (Arrenberg et al., 2010). Confocal microscopy, in contrast, relies on point detection and sequential pixel readout, which is intrinsically slower, taking in the range of seconds, depending on the field of view and the pixel resolution. Parallelization approaches like spinning disk confocal microscopy increase the image acquisition speed, however, this is at the expense of some resolution, especially in axial direction because pinholes on the disk are generally larger than in a single-point scanning system (Peterson, 2010; Stelzer, 2015; Wang et al., 2005).

When it comes to optical resolution, confocal microscopy is superior to light-sheet microscopy. Theoretically, the use of a pinhole improves lateral and axial resolution by a factor of  $\sqrt{2}$  compared to widefield detection (Cox and Sheppard, 2004). In practice, some additional resolving power in light-sheet microscopes is usually sacrificed for a long working distance of the detection objective to reach through thick, three-dimensional samples. The longer the working distance, the smaller the half-angle of light collection  $\theta$ , which directly determines the lateral resolution  $r_{\text{lat}}$ , given by  $r_{\text{lat}} = \lambda_{\text{em}} (2n \sin \theta)^{-1}$ .  $\lambda_{\text{em}}$  is the emission wavelength and  $n$  the refractive index of the imaging buffer.

In axial direction, the resolution of a light-sheet microscope is the product of the illumination and detection point spread functions (PSF; Fig. 1E). The thinner the light-sheet the better the axial resolution, however, refraction dictates that a tightly focused beam (i.e. a beam focused with high numerical aperture; NA) rapidly diverges (Power and Huisken, 2017). Thus, there is a trade-off between the length of a Gaussian light-sheet and its thickness. Usually the length of a light-sheet  $z_{\text{ls}}$  is defined as the region in which the minimum thickness of the sheet  $\omega_0$  grows no more than by a factor of  $\sqrt{2}$  (Fig. 1D). It is given according to the Rayleigh length by  $z_{\text{ls}} = \pi(2\omega_0)^2(\lambda_{\text{exc}})^{-1}$ , with  $\lambda_{\text{exc}}$  being the excitation wavelength (Gao et al., 2014). For example, a light-sheet of 4  $\mu\text{m}$  thickness is needed to cover a 100  $\mu\text{m}$  field of view at  $\lambda_{\text{exc}} = 514 \text{ nm}$ . Axial resolution  $r_{\text{ax}}$  of the widefield detection path is given by  $r_{\text{ax}} = \lambda_{\text{em}} (n(1 - \cos \theta))^{-1}$ , which is  $\sim 1.2 \mu\text{m}$  in the example (with  $n = 1.33$  for water and  $\text{NA} = n \sin \theta = 1$ , thus  $\theta = 49^\circ$ ). Consequently, for large fields of view of 0.1–1 mm the axial resolution of a light-sheet microscope is similar to that of a widefield microscope and  $\sqrt{2}$  lower than for a confocal microscope (Gao et al., 2014).

To generate longer and thinner light-sheets and improve axial resolution, Bessel beams and Airy beams have been implemented as alternatives to the Gaussian beam profile (Gao et al., 2014; Vettenburg et al., 2014).

Due to the angular objective configuration in a light-sheet microscope, “standard” mounting on a microscope slide is difficult to realize. This drawback has evolved into one of the big strengths of the technology. An array of alternative mounting configurations has been developed to specifically meet the needs of a given application (Power and Huisken, 2017). Many variants, like mounting in a cylinder or capillary perpendicular to the illumination-detection plane, allow for sample rotation to enable subsequent imaging of different parts of the specimen. This is beneficial if scattering and optical density of the tissue limit penetration (Huisken et al., 2004). Alternatively, to increase speed, several illumination and detection paths are arranged around the specimen to acquire multiple views without sample rotation (Krzic et al., 2012; Schmid et al., 2013; Tomer et al., 2012). Computational fusion of the image stacks after acquisition is used to generate *in toto* datasets of large specimen with almost homogenous resolution (Fig. 1F; Weber and Huisken, 2011).

Owing to the relatively simple optical setup of a light-sheet microscope, an impressive collection of custom-built setups has been developed in recent years with different illumination strategies (summarized in Stelzer, 2015) and diverse numbers and/or configurations of objectives to meet various demands imposed by the samples (Power and Huisken, 2017).

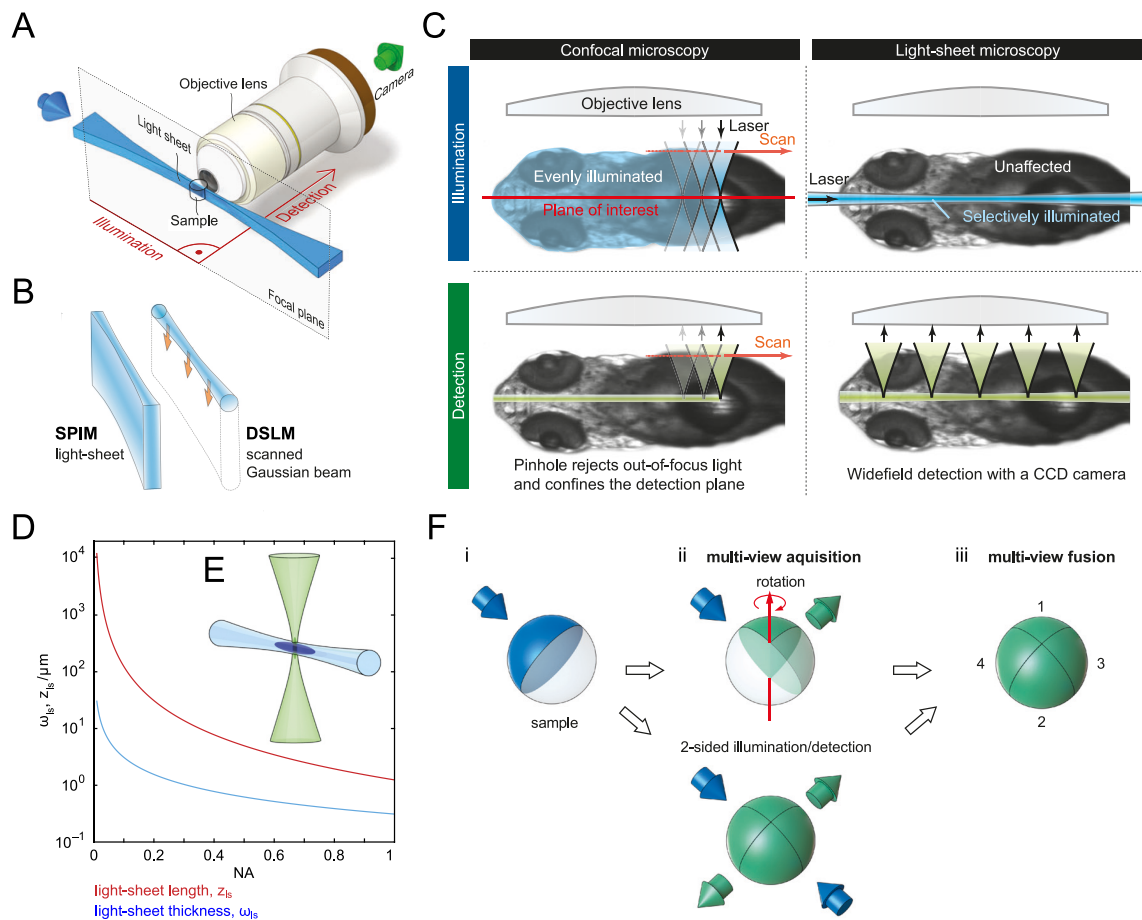


**Fig. 1: The basics of light-sheet microscopy.** (A) Optical paths for illumination and detection are decoupled and arranged at a right angle with respect to each other. The sample is placed at the intersection of these paths, in the focus of the detection objective, and fluorescence is captured on a camera. (B) Light-sheets can be generated by focusing a Gaussian beam in one dimension with a cylindrical lens (for SPIM) or by scanning a focused beam along the axis of the sheet (for DSLM). (C) Comparison of principles of confocal and light-sheet microscopy illumination (upper row, blue) and detection (lower row, green). In confocal microscopy, the excitation focus is scanned over the field of view through the objective lens, illuminating the entire sample (depicted here as the upper body of a zebrafish larvae) also above and below the plane of interest. Optical sectioning is performed on the detection side by rejecting out-of-focus light with a pinhole. Light-sheet microscopes perform optical sectioning by selectively illuminating the plane of interest from the side, leaving all other planes unaffected. Detection of the entire plane is done simultaneously, and the signal is imaged onto a camera. (D) Relation of light-sheet length ( $z_{ls}$ ) and light-sheet thickness ( $\omega_{ls}$ ) to the NA of the illumination optics. (E) The effective PSF of a light-sheet microscope is the product of the lateral component of the illumination PSF (dark blue) and the axial component of the detection PSF (dark green). (F) Multi-view imaging and reconstruction of a large specimen. (i) Due to scattering and absorption, only the side of a sample orientated towards the light sheet (blue arrow) is optimally illuminated (depicted by the blue hemisphere). (ii) Similarly, detection quality decreases with increasing distance to the detection objective (green arrow), leaving only about one quadrant of the image volume with optimal resolution. To compensate for the image quality loss, several image stacks are acquired from different angles, either by sample rotation or by using several illumination/detection paths arranged around the sample. (iii) The image stacks are then

computationally combined to generate one 3D dataset. Adapted from Huisken and Stainier (2009) with permission from Elsevier, Power and Huisken (Power and Huisken, 2017) with permission from The Company of Biologists Ltd, and Weber and Huisken (2011) with permission from Springer Nature.

## 1.2 Light-sheet imaging of mammalian embryos

Light-sheet microscopy has been applied very successfully to imaging of externally developing embryos including fish, *Drosophila* and other insects (Huisken et al., 2004; Keller et al., 2008; Strobl and Stelzer, 2014). Long-term live imaging of mammalian embryos harbors additional challenges since these embryos are not directly accessible in the uterine environment. This environment has to be recapitulated as well as possible on the microscope, including the implementation of careful atmospheric control and specific medium composition. Further, due to the viviparous nature of their development, mammalian embryos are not adapted to tolerate light and their photosensitivity is therefore extremely high (Garcia et al., 2011; Nowotschin et al., 2010; Strnad et al., 2016).

On a dedicated light-sheet setup, Strnad and colleagues managed to capture mouse pre-implantation development ranging from zygote to blastocyst *in toto*. They achieved a temporal resolution that allowed full lineage tracing from 1 to 64 cells over three days of development, setting new standards for mouse embryo microscopy (Strnad et al., 2016). For post-implantation mouse embryo imaging, the microscopist faces a number of additional complications: First, the large size of 200–600  $\mu\text{m}$  in combination with optically unfavorable tissue properties makes *in toto* imaging from a random angle impracticable. Consequently, the embryo has to be mounted in such a way that the region of interest can be orientated in respect to the objectives. Second, because of substantial growth, gel embedding of the embryo is problematic as it negatively impacts on development. Last, long-term embryo culture requires a substantial amount of primary serum in the culture medium, which has non-favorable optical properties.

Ichikawa and colleagues solved the mounting problem by inserting the ectoplacental cone in small holes of a custom-made sample holder, leaving the embryo room to expand (Fig. 2A). Using this holder the researchers followed cell migration in embryonic day (E)5.5 and E6.5 embryos at 1.5 min imaging intervals on a light-sheet microscope

(Fig. 2B,C). However, phototoxic effects limited the observation period to 3 h, highlighting the extreme photosensitivity of post-implantation embryos (Ichikawa et al., 2013). An alternative mounting approach in a hollow agarose cylinder was pursued by Udan and colleagues (Fig. 2D,E). They cultured and imaged E6.5 and E7.5 embryos and reported no obvious developmental defects after 24 h of light-sheet imaging (Fig. 2F; Udan et al., 2014).

Beyond day 8 of embryonic development, *in toto* imaging becomes impracticable as the mouse embryo reaches several millimeters in size, the tissue gets very opaque and several membranes around the embryo hinder optical access. Live imaging of certain aspects of the embryo, however, is still possible. Imaging studies on the development of the heart at late E7.5 (Ivanovitch et al., 2017), or neural tube closure (Pyrgaki et al., 2010) and vasculature development in E8.5-9.5 embryos (Jones et al., 2005; Lucitti et al., 2007) have been performed using confocal microscopy. Since photosensitivity becomes less of a problem after E7.5, confocal or two-photon microscopy remain a good option for the recording of superficial structures in organogenesis stage embryos. The next years will show whether light-sheet microscopy with its unique advantages will also establish as a standard live imaging technique during these late embryonic stages.

In summary, light-sheet microscopy has become the method of choice to conduct live studies on large, complex specimen. The unique potential of the technique to acquire large 3D datasets fast and at low light levels has opened up new possibilities to explore embryonic development at unprecedented detail and in a quantitative manner.

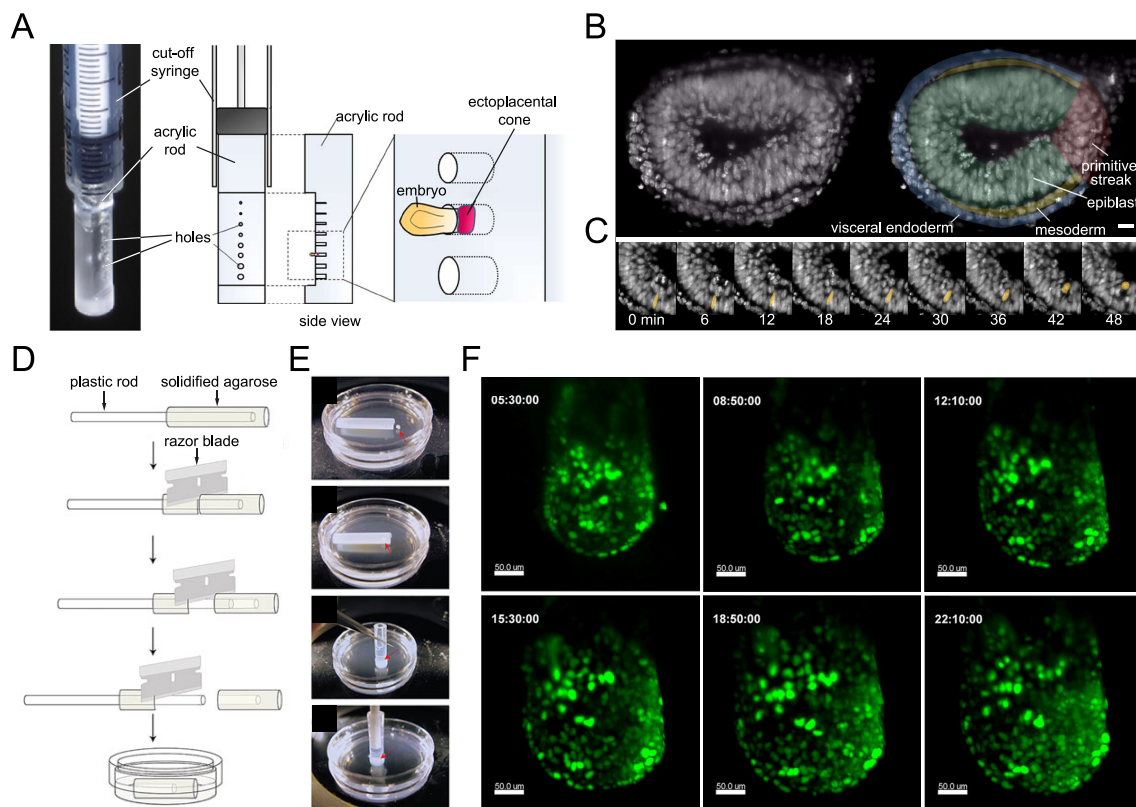


**Fig. 2: Light-sheet imaging of post-implantation mouse development.** (A) Mounting and imaging described by Ichikawa and colleagues for E5.5 and E6.5 embryos. A 1 ml syringe with the tip cut off holds an acrylic rod with small holes of different sizes. The ectoplacental cone of embryos is inserted into the holes, leaving the embryos free to grow in the medium (left, picture of the actual sample holder; right, schematic drawing). (B) Nuclear-labeled E6.5 embryo imaged over time using the holder described in (A). A transverse section through the egg cylinder is shown (left) and with tissue layers labeled and colored (right), posterior points to the right. Scale bar: 20  $\mu\text{m}$ . (C) Time series of a detail of the embryo shown in (B). One nucleus labeled in yellow migrates through the epiblast in apical direction. (D) Manufacturing of an agarose cylinder for mounting E6.5 to E8.5 embryos as described by Udan and colleagues. An agarose cylinder is cast around a plastic rod. After cutting the cylinder to the right height, the rod is removed, and the hollow cylinder is incubated in culture medium. (E) An embryo (red arrow) is moved into the cylinder, then the cylinder is closed with the plastic rod. In this configuration, the rod with the agarose cylinder is mounted in the light-sheet microscope. (F) Still frames from a 24 h time-lapse experiment of an E6.5 embryo using the agarose cylinder mounting method. Embryo expresses TCF/LEF-H2BeGFP, marking cells that activated the canonical Wnt pathway. Adapted from Ichikawa *et al.* (2013) and Udan *et al.* (2014) with permission from The Company of Biologists Ltd.

## 2. Gastrulation of the vertebrate embryo

Somites are formed from precursor cells in the mesoderm tissue. The mesoderm first appears during gastrulation, the process in which bilaterian embryos reorganize into the three germ layers: ectoderm, endoderm, and mesoderm. From early gastrulation to the organogenesis phase, in which somites are formed, the embryo's morphology changes drastically as complexity increases. To help the understanding of later chapters, this section will give a brief overview of the morphological events of mouse gastrulation. Compared to the stereotypic discoid shape of avian and most mammalian embryos, the mouse gastrula has a rather complex cup-shaped form and undergoes gastrulation in an "inside-out" configuration with the ectoderm on the inside and endoderm on the outer surface (Tam and Gad, 2004).

In mouse, gastrulation begins on the sixth day of development, two days after the blastocyst has implanted into the uterine wall. At this "egg-cylinder" stage, the embryo is a hollow sphere, elongated in proximodistal direction (proximal being the end where the embryonic tissue contacts maternal tissues). The proximal half gives rise to extra-embryonic material while the distal half constitutes the embryo proper. The egg cylinder consists of two cell layers, visceral endoderm (VE) on the outside and the epiblast on the inside. The central proamniotic cavity defines the later dorsoventral polarity: The cavity wall becomes dorsal, while the outer surface of the VE corresponds to the ventral side (Fig. 3A). Only after gastrulation is finished, an inversion brings the ectoderm to the outside on day 8 of embryonic development (Tam and Behringer, 1997).

With the onset of gastrulation at E6.5 the anteroposterior axis of the egg-cylinder becomes morphologically evident. The anterior visceral endoderm (AVE) thickens while on the posterior proximal pole, epiblast cells begin to converge to form the primitive streak (PS; Fig. 3B). The PS is the transition zone in which epiblast cells delaminate, undergo an epithelial-mesenchymal transition and then ingress in-between epiblast and VE to become mesoderm, or integrate into the VE layer to form definite endoderm (Fig. 3C; Tam and Behringer, 1997). The PS progressively expands distally until it reaches

the distal tip of the embryo after 36 h (Arnold and Robertson, 2009). The distal extent of the streak during this period is used to stage embryos from early streak (ES) over mid streak (MS) to late streak (LS; Downs and Davies, 1993). At LS stage, when the PS is maximally extended, the organizer (a structure capable of inducing the formation of an embryo axis when transplanted to an ectopic location), called the “node” in mouse, becomes apparent, marking the distal end of the PS (Fig. 3D; Beddington, 1994).

Fate mapping studies have shown that during distal expansion of the streak, extra-embryonic tissue ingresses first through the proximal PS. Lateral plate, cardiac and paraxial mesoderm emerge slightly later from the intermediate and distal levels of the streak. The area of the node located at the extreme distal tip gives rise to axial mesoderm and the definite endoderm lineage (Lawson et al., 1991; Tam and Beddington, 1987). The nascent mesoderm spreads as wings around the egg cylinder, fully enveloping the epiblast at early allantois bud (EB) stage at E7.5 (Kinder et al., 2001). Mesoderm cells move essentially as a cohesive sheet in anterior and distal direction (Nakatsuji et al., 1986). In late gastrulation, the PS regresses again, and a new structure, the tailbud, forms from posterior paraxial mesoderm. During this stage, the node moves posteriorly and is eventually absorbed into the tailbud. The tailbud remains as growth zone at the very posterior end of the embryo until axis elongation is completed.



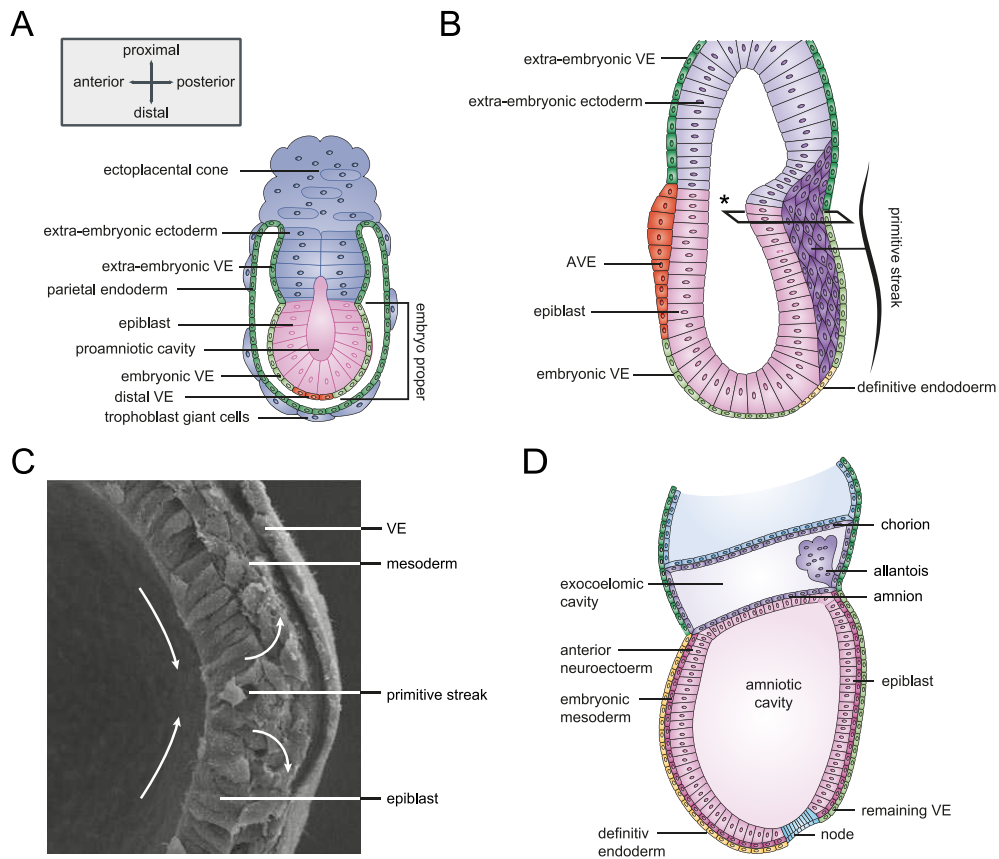


**Fig. 3: Gastrulation of the mouse embryo.** (A) E5.5 pre-streak stage mouse embryo, (B) E6.5 mid streak stage embryo. (C) Electron micrograph of a cross-section through the posterior of an embryo as indicated in (B; asterisk) showing the loosening of the epithelial tissue during epithelial-mesenchymal transition in the PS. (D) At early allantois bud stage, the entire egg-cylinder is surrounded by mesoderm and the node is visible at the distal tip of the embryo. (A,B,D) are oriented according to the panel in (A). *Adapted from Arnold and Robertson (2009) with permission from Springer Nature.*

## 3. Signaling dynamics in somitogenesis

### 3.1 Somitogenesis

Unifying and class-defining feature of all vertebrates is the spinal column, which is characterized by a concatenation of repetitive elements—or metameres. The precursors of the regular body segments of vertebrates and cephalocordates are somites, tissue blocks, which are sequentially formed during embryogenesis in the process of somitogenesis. During somitogenesis the paraxial mesoderm on both sides of the neural tube is rhythmically segmented in a tightly coordinated, bilateral fashion in a head-to-tail direction. Concomitant with the elongation of the embryo body axis, a new pair of somites is added at regular intervals, for example every 90 min in chicken (Palmeirim et al., 1997), 120 min in mice (Tam, 1981) and 30 min in zebrafish (Schröter et al., 2008). The total number of somites in different vertebrates is highly variable, for example frogs have ~10, humans have 33 and snakes have up to several hundred somites (Gomez et al., 2008; Richardson et al., 1998).

In mouse, the source of the paraxial mesoderm changes over the period of somitogenesis. At the beginning, during late gastrulation, it is fed from cells that have ingressed through the distal portion of the PS (Tam and Beddington, 1987). With progressing segmentation the PS disappears and the tailbud provides the material for paraxial mesoderm as well as neural tube elongation (Henrique et al., 2015; Tzouanacou et al., 2009). At tailbud stage, the paraxial somite-precursor tissue is referred to as presomitic mesoderm (PSM).

The first morphological sign of a new somite is the formation of a cleft in the anterior region of the PSM, one somite length away from the last somite boundary (Fig. 4). Cells anterior to the cleft epithelialize and form a sphere with anterior-posterior identity (Chal and Pourquié, 2009). Somite compartmentalization continues by the acquisition of ventral and dorsal identities. The dorsal aspect becomes the dermomyotome, eventually giving rise to skeletal muscles, and back dermis. The ventral part of a somite, the sclero-

tome, undergoes a resegmentation process in which each somite splits and the posterior and anterior compartments of two adjacent somites fuse (Fig. 4; Christ and Scaal, 2008). The resegmented sclerotome forms the basis of the vertebrae. Thus, the initial position of somite clefts and the intervertebral discs between vertebrae are shifted by half a somite length.

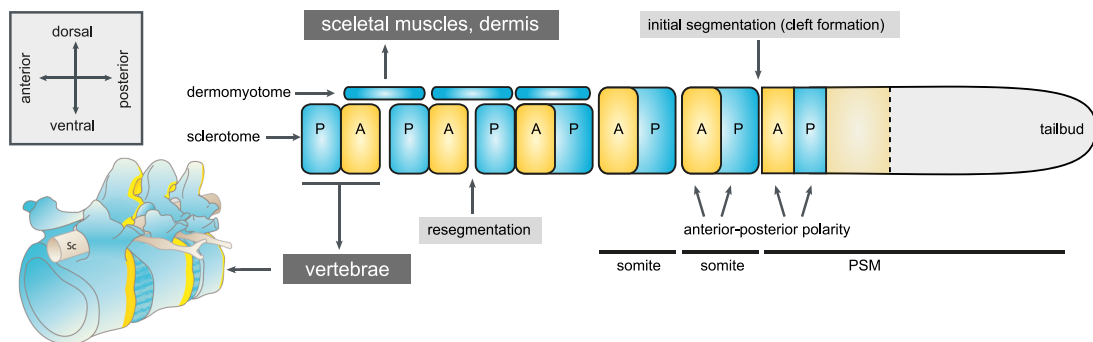


**Fig. 4: Segmentation and resegmentation of the vertebrate body axis.** Somites with antero-posterior polarity get defined at the anterior end of the PSM and separate from unsegmented tissue with a morphological cleft. During further somite development, they acquire a ventro-dorsal polarity separating dermomyotome, destined to form skeletal muscles and dermis, and sclerotome. The sclerotome resegments and differentiates to vertebrae. A vertebra thus consists of the former posterior and anterior compartments of two adjacent somites. (A) anterior, (P) posterior, (Sc) spinal cord. *Adapted from Chal and Pourquié (2009) with permission from Cold Spring Harbor Laboratory Press, and Saga and Takeda (2001) with permission from Springer Nature.*

### 3.2 A model for clock-based segmentation

In 1976, Cooke and Zeeman proposed the “clock and wavefront” model for somite segmentation, specifically to explain segment scaling. Scaling refers to the observation that the total number of somites is largely invariant between larger and smaller embryos while the size of the individual segments depends on the total size of the organism. Cooke and Zeeman reasoned that the segmentation machinery has to consist of two components, one that takes into account the overall size of the tissue and one that regulates the number of segments independently of the tissue size (Cooke and Zeeman, 1976). In the clock and wavefront model, segmentation timing and localization is therefore determined by the integration of a molecular clock that ticks in the cells of the unsegmented tissue, and a wavefront, also referred to as determination front, that moves slowly from anterior to posterior in the PSM. The model predicts that when the deter-

mination front moves across cells at a specific oscillation phase, these cells abruptly change their properties and initialize the formation of a somite boundary. The antero-posterior length of the segment is thus determined by the number of cells that were crossed by the front within one cycle.

Inspired by the work of Wolpert (Wolpert, 1969; Wolpert, 1971) Cooke and Zeeman proposed that somite size is regulated by changing the propagation velocity of the determination front, which may be realized in the form of a morphogen gradient, while the clock keeps an invariant rhythm (Cooke and Zeeman, 1976).

### *Oscillatory pathways in the PSM*

Experimental evidence for the existence of a segmentation clock was delivered by the discovery of the oscillatory expression of the segmentation gene *HAIKY1* (Homolog of hairy 1) in chick, which belongs to the *HES* (Hairy and enhancer of split)/ *HER* (HES-related) family of transcription factors that act mainly as Notch effectors (Palmeirim et al., 1997). In each cycle, *HAIKY1* expression starts as broad domain at the tailbud, travels anteriorly as increasingly narrow stripes left and right of the neural tube and stops just posterior to the last formed somite (Fig. 5).

In the following years, additional genes across several species have been identified that show oscillatory expression patterns in the PSM. Most cyclic genes can be attributed to the Wnt (Wingless and INT-1), FGF (Fibroblast growth factor) or Notch signaling pathways in the PSM. In all vertebrate species studied, one or several members of the *HES/HER* family were found to oscillate, implying a fundamental role of these transcription factors in the segmentation clock (Bessho et al., 2001; Holley et al., 2002; Kusumi et al., 2013; Oates and Ho, 2002).

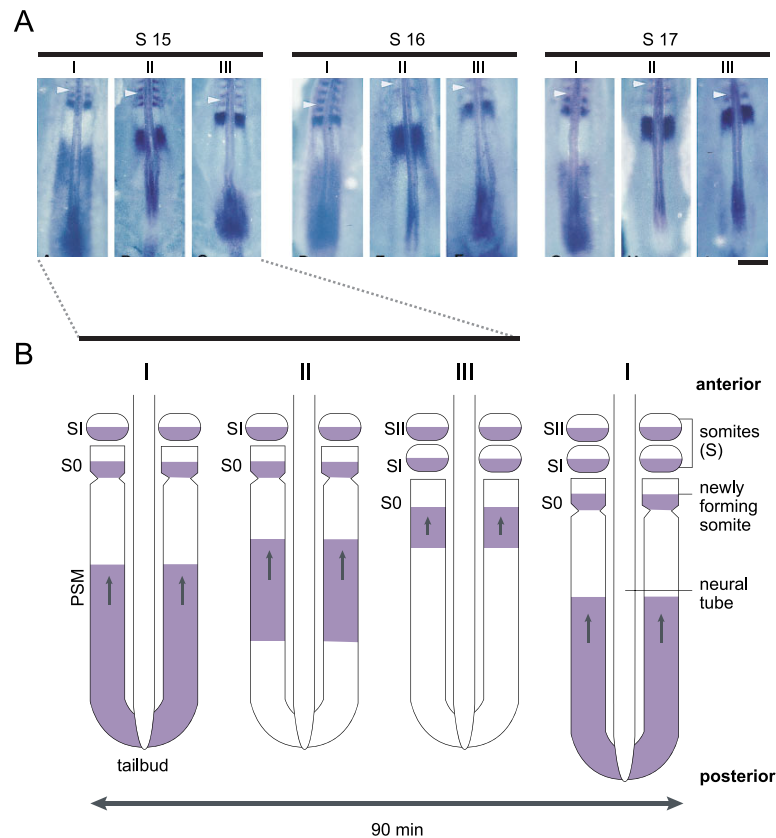


**Fig. 5: Waves of *HAIRY1* expression in the chick PSM.** (A) *HAIRY1* expression patterns between formation of somite (S) 15 and 17 are shown. The position of the last formed somite is marked with an arrowhead. Patterns can be sorted into three groups (I–III) according to the position of the expression domain along the PSM. Scale bar: 200  $\mu\text{m}$ . (B) Schematic of *HAIRY1* waves sweeping from the tailbud anteriorly, marking the position of the next somite boundary. Adapted from Palmeirim *et al.* (1997) with permission from AAAS, and Saga and Takeda (2001) with permission from Springer Nature.

### *Molecular loops to generate oscillations*

How can sustained oscillations arise at a molecular level? A simple mechanism to achieve such dynamic profiles is a negative feedback loop with delayed inhibition, as it was proposed for the HES/HER oscillator (Fig. 6A; Lewis, 2003). HES1/7 in mice and Her1/7 in zebrafish can auto-inhibit their own transcription and the required delay is fulfilled by the time it takes from transcription to the active, repressive protein. Several studies identified splicing and nuclear export as key steps for introducing the delay (Harima *et al.*, 2013; Hoyle and Ish-Horowicz, 2013; Takashima *et al.*, 2011). In addition, sustained, high amplitude oscillations of delayed negative feedback loops require fast degradation kinetics of cyclic mRNA and proteins (Lewis, 2003). The half-lives of

*Hes1* mRNA and HES1 protein in mouse, for example, are 24 and 22 min, respectively (Hirata et al., 2002), indicating that this requirement is met in the PSM.

### 3.3 Topology of the mouse oscillator

Members of the HES/HER protein family have the potential to generate sustained oscillations, but is this insight enough to fully explain the somite-clock work? No—the segmentation clock in mouse, which we will focus on throughout this work, integrates several pathways, which form multiple potential delayed negative feedback loops. To date, no definite hierarchy between these oscillators could be established. In the following, I will cover the signaling topology of the three known oscillatory pathways of the mouse PSM: Notch, FGF and Wnt.

#### *Notch signaling*

The core of the Notch signaling oscillator contains the delayed negative feedback loop around the *Hes* transcription factor family. Three paralogs are present in the mouse genome, *Hes1*, 5 and 7, but only a *Hes7* knockout results in strong segmentation defects (Bessho et al., 2001; Kageyama et al., 2007). Persistent *Hes7* expression leads to somite fusion (Hirata et al., 2004), and removal of *Hes7* introns affects somite number and size (Harima et al., 2013). These findings emphasize the requirement of finely tuned dynamic *Hes7* expression for a functioning segmentation clock.

HES7 protein does not only repress its own transcription, but also that of other Notch target genes. One of these is *Lfng* (Lunatic fringe), a glycosyltransferase that has been shown to negatively regulate Notch signaling activity. The precise mechanism of regulation, however, is under debate. LFNG has been proposed to modulate Notch receptor activity by glycosylation (Brückner et al., 2000; Moloney et al., 2000). Other studies propose a model in which LFNG modulates the Notch ligand DLL1 (Delta-like 1), thereby repressing Notch activity in neighboring cells (Okubo et al., 2012). These models are not mutually exclusive, thus LFNG may play a role both intra- and intercellularly.

It was shown that *Lfng* oscillations depend on periodic transcriptional repression by HES7: Absence of HES7 causes constitutive *Lfng* expression, conversely, stabilization of the HES7 protein results in non-dynamic repression of *Lfng* (Bessho et al., 2001; Bessho et al., 2003).

*Hes7* and *Lfng* are induced *via* Notch signaling. Upon activation of Notch, the Notch-intracellular domain (NICD) is cleaved off by the  $\gamma$ -secretase and translocates into the nucleus, where it complexes with the transcriptional repressor RBP-J  $\kappa$  (Recombination signal binding protein for immunoglobulin  $\kappa$  J region; Morales et al., 2002). RBP-J  $\kappa$  constitutively binds to Notch target promoters and in combination with NICD it becomes a transcriptional activator (Fig. 6B). Also NICD has been found to oscillate in the PSM (Huppert et al., 2005; Morimoto et al., 2005). Potentially, Notch and *Hes7* oscillations are coupled through *Lfng* which may periodically inhibit Notch (Okubo et al., 2012), however, the exact mode of action of *Lfng* remains to be clarified (Serth et al., 2003). In addition, also the Notch receptor DLL1 was shown to oscillate both on mRNA and on protein level in phase with *Lfng* and *Hes7* (Bone et al., 2014).

### *FGF signaling*

Targets of the FGF/ERK (Extracellular signal-regulated kinase) pathway show cyclic activation and also the phosphorylation state of ERK was shown to change periodically in the PSM (Dequéant et al., 2006; Niwa et al., 2007). Notch and FGF targets oscillate in-phase in the posterior PSM and seem to be linked by *Hes7*. This is based on the observation that FGF signaling is required for *Hes7* oscillations in the posterior PSM, and conversely, in the absence of oscillatory *Hes7* the cyclic activity of pERK, *Dusp4* (Dual specificity phosphatase 4) and *Spry2* (Sprouty homolog 2) is lost (Fig. 6C; Hayashi et al., 2009; Niwa et al., 2007; Niwa et al., 2011). Whether stable FGF signaling would be sufficient or whether FGF pathway oscillations are required for *Hes7* dynamics is unclear (Hubaud, 2016). However, the absolute level of FGF signaling does impact on the oscillation dynamics in the PSM as I will discuss in Introduction, section 3.6.

### *Wnt signaling*

Wnt targets oscillate out of phase with Notch and FGF targets in the tailbud (Aulehla et al., 2003; Dequéant et al., 2006; Krol et al., 2011; Sonnen et al., 2017). While FGF and Notch pathway oscillations are closely connected, Wnt signaling seems to follow an independent oscillator. This view is based on the findings that the Wnt target *Axin2* oscillates in *Hes7*-null mutants as well as other mutants defective for Notch signaling (Aulehla et al., 2003; Feller et al., 2008; Ferjentsik et al., 2009; Hirata et al., 2004). However, Notch and Wnt signaling oscillations are not completely independent of each other, as demonstrated by Sonnen and colleagues. They managed to entrain PSM oscillations to an external frequency by cyclic administration of pharmacological modulators. Administration of a Notch inhibitor did not only entrain *Lfng* but also *Axin2* oscillations and conversely, cyclic activation of Wnt signaling entrained *Axin2* as well as the Notch target (Sonnen et al., 2017). On molecular level the interaction between Notch and Wnt pathway may involve the Notch ligand *Dll1* which was shown to be Wnt regulated (Bone et al., 2014).

In general, canonical Wnt signaling is thought to be mediated by the degradation kinetics of  $\beta$ -catenin (*Ctnnb1*; Fig. 6C). When the Wnt ligand binds its receptor Frizzled, the  $\beta$ -catenin destruction complex is inhibited,  $\beta$ -catenin accumulates in the nucleus and activates Wnt target gene transcription. Wnt target *Axin2* is also part of the destruction complex, thereby negatively regulating Wnt pathway activity. To test if the  $\beta$ -catenin–*Axin2* loop constitutes a delayed feedback oscillator responsible for Wnt oscillations, Aulehla and colleagues examined PSM oscillations in embryos harboring the  $\beta$ -catenin<sup>del(ex3)</sup> gain-of-function allele which lacks a crucial recognition site for the destruction complex (Aulehla et al., 2008; Harada et al., 1999). However, Wnt targets were still expressed dynamically in the presence of a high level of stable  $\beta$ -catenin, a finding that does not support oscillating (nuclear)  $\beta$ -catenin levels as sole mechanism to generate Wnt target oscillations. Alternatively, Wnt signaling oscillations might be generated by cyclic recruitment of cofactors to the genomic enhancer/promoter locus of Wnt targets or post-translational modifications (Aulehla et al., 2008; Sierra et al., 2006).

Summarizing the current state of knowledge, oscillations of cyclic genes in the PSM may not originate from a single, central pacemaker but rather integrate dynamic input



from several interconnected oscillatory loops, which influence each other without a clear hierarchy.

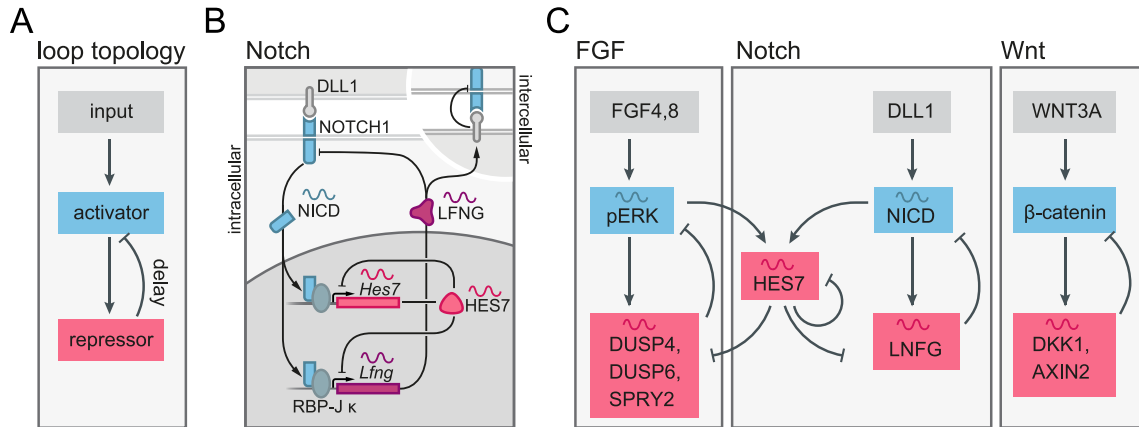


**Fig. 6: Oscillatory signaling networks in the mouse PSM.** (A) Topology of a delayed negative feedback loop to generate oscillations. Color code is maintained in (B) and (C). (B) Interconnected signaling loops in the Notch pathway. Upon activation, NOTCH1 is cleaved and NICD translocates to the nucleus where it binds RBP-J  $\kappa$  and activates transcription of Notch targets like *Hes7* and *Lfng*. HES7 auto-represses its own transcription, but also that of *Lfng*, generating sustained oscillations. LFNG is thought to modulate Notch activity intracellularly by inhibiting NOTCH1 and intercellularly by inhibiting NOTCH1 in neighboring cells through direct or indirect modification of DLL1. Components known to be cyclic are marked with a wave. (C) Feedback loops of FGF, Notch and Wnt signaling pathways. Binding of FGF ligands to their cognate receptor results in the activation of the ERK pathway and downstream activation of *Dusp4*, *Dusp6* and *Spry2*, which inhibit the FGF pathway. FGF and Notch oscillations are linked via *Hes7* which can be activated by pERK in posterior PSM and represses FGF downstream targets. The Wnt pathway appears to function as an independent oscillator. Pathway activation leads to  $\beta$ -catenin mediated transcription of oscillatory genes *Axin2* and *Dkk1* which negatively regulate the pathway by promoting  $\beta$ -catenin degradation. Components that have been shown to oscillate are marked with a wave. (A,C) Adapted from Hubaud and Pourquié (2014) with permission from Springer Nature.

### 3.4 Signaling gradients and the wavefront

According to the clock and wavefront model, oscillations are translated into a regular pattern of boundaries by a spatial component: the determination front. Several members of the FGF and Wnt as well as retinoic acid (RA) pathways show a graded distribution within the PSM (Aulehla and Pourquié, 2010). While FGF and Wnt activity gradients peak in the posterior PSM and are low in the anterior, RA displays a complementary gradient orientation, being highest in somites, decreasing towards the posterior PSM. Since alterations of these gradients affect the positioning of somite boundaries along the

anteroposterior axis, these morphogen gradients have been proposed as determination front candidates (Aulehla and Pourquié, 2010).

For FGF signaling, it has been shown that FGF8 overexpression delays segmentation and PSM differentiation and ectopic activation or repression locally shifts the position of boundary formation anteriorly or posteriorly, respectively (Dubrulle et al., 2001; Sawada et al., 2001). Similarly, over-activation of the Wnt pathway by expressing stabilized  $\beta$ -catenin from the  $\beta$ -catenin<sup>del(ex3)</sup> allele maintains clock oscillations for longer, shifting the region of somite differentiation further anteriorly (Aulehla et al., 2008). Thus, FGF and Wnt signaling gradients seem to have similar effects on the timing of somite differentiation. A clear attribution of the role as determination front to one of the two pathways is difficult because of crosstalk between them. In fact, stabilized  $\beta$ -catenin expression induces an anterior expansion of the FGF8 gradient and Wnt signaling loss in  $\beta$ -catenin-null mutants decreases FGF8 levels (Aulehla et al., 2008; Dunty et al., 2008). Conversely, double *Fgf4/8* mutants have decreased expression of *Wnt3a* (Boulet and Capecchi, 2012; Naiche et al., 2011).

In addition, the opposing RA gradient also influences the FGF gradient. Reduction of anterior RA levels shift the FGF gradient anteriorly (Diez del Corral et al., 2003; Moreno and Kintner, 2004; Vermot and Pourquié, 2005). However, the role of RA is not fully understood, since loss-of-function mutants for *Cyp26a1*, a cytochrome p450 enzyme involved in RA degradation in the PSM and thereby generation of the gradient (Sakai et al., 2001), do not show a posterior shift of segment differentiation markers (Morimoto et al., 2005).

### 3.5 Oscillation synchronization across the tissue

Macroscopic PSM waves are the result of synchronized oscillations of thousands of individual cells, raising the question, how such synchrony is achieved. Interestingly, communication between cells is dispensable for maintaining coherence and synchrony among cells, at least for a certain time. This aspect is demonstrated by the observation that cutting of the PSM tissue into pieces, thereby physically separating cells, does not impede wave propagation (Lauschke et al., 2013; Masamizu et al., 2006; Palmeirim et

al., 1997). These experiments shaped the view of the PSM as an assembly of autonomously oscillating cells. The PSM waves do not carry any matter or information but behave as “kinematic waves” which are the result of a gradual phase shift between oscillatory units in the direction of wave propagation.

Molecular evidence for self-sustained oscillatory gene expression loops as described in Introduction, section 3.2, for the *HES/HER* gene family supports the autonomous oscillator concept. However, while cells continue to oscillate in synchrony in the absence of communication for a certain period, the study of Notch signaling mutants and pharmacological disruption of the Notch pathway in fish (Jiang et al., 2000) suggest that intercellular communication mediated by Notch signaling is necessary to ensure tight coordination of cyclic activity for the prolonged period of several days, which somitogenesis takes to be completed. In zebrafish, Notch signaling mutants display asynchronous and noisy oscillations (Delaune et al., 2012; Horikawa et al., 2006). Furthermore, the concept of gradual desynchronization of independent oscillators in fish receives support from studies showing a lag time between the introduction of pharmacological Notch signaling disruption and the onset of morphological segmentation defects (Ozbudak and Lewis, 2008; Riedel-Kruse et al., 2007). Notch signaling-mediated synchronization appears to be conserved in mouse, involving *LFNG*, which represses Notch signaling in neighboring cells, possibly by inhibiting *DLL1* activity (Fig. 6B; Okubo et al., 2012). Further support for the importance of intercellular Notch signaling for synchronization in mouse comes from experiments using an *in vitro* assay of randomized PSM cells: Under normal conditions, cells manage to resynchronize their oscillations within a few hours, as monitored by a fluorescent *Lfng* reporter. In contrast, under pharmacological inhibition of Notch intercellular communication, using  $\gamma$ -secretase inhibitor DAPT (Dovey et al., 2001), cells fail to synchronize, yet continue to oscillate individually (Tsiairis and Aulehla, 2016).

As Wnt targets were shown to oscillate synchronously in mouse Notch mutants (Aulehla et al., 2003; Feller et al., 2008; Ferjentsik et al., 2009), it is conceivable that a Notch independent synchronization mechanism exists. However, studies addressing the synchronization of Wnt signaling oscillations in the PSM in the presence or absence of Notch signaling have not been conducted so far.

### 3.6 The making of waves

Having reviewed the potential mechanisms of oscillation synchronization, let us focus on the nature of the traveling PSM waves.

If all cells in the PSM are regarded as individual oscillators which had the same period and were synchronized in their oscillation phase, the entire tissue would pulse together. The presence of traveling waves demonstrates that oscillations along the direction of wave propagation are slightly phase shifted in respect to each other (Lauschke et al., 2013; Ross et al., 1988). One way to achieve the buildup of such phase waves is a period gradient: If elements at one side of the oscillatory field oscillate faster than on the other side, their phase gradually drifts apart (Fig. 7A; Kopell and Howard, 1973).

Indeed, as measured for *Lfng* in mouse (Tsiairis and Aulehla, 2016) and indirectly shown for *her1* and *her7* in zebrafish (Giudicelli et al., 2007; Gomez et al., 2008), the oscillation period in the PSM is not uniform but increases from posterior to anterior. In posterior cells, the oscillation period matches the somite segmentation period. Due to growth at the posterior and segmentation at the anterior end of the tissue, the relative position of a cell in the PSM changes: Cells therefore “move” from posterior to anterior. In parallel to the anteriorward relocation, cells progressively slow down their oscillations. This results in a mismatch between oscillation period of anterior cells and the segmentation rate, which is compensated by the anterior-to-posterior progression of the segmentation front, effectively shortening the relative anterior period, as illustrated in Fig. 7B–D (Soroldoni et al., 2014).

A period gradient is sufficient to build up waves, but how is the oscillation period change regulated in the PSM? A possible mechanism links the period gradient with the PSM signaling gradients. Preliminary data from our laboratory indicate that the addition of FGF8 to *ex vivo* cultured PSM cells does not only affect the determination front but also changes *Lfng* oscillation dynamics. Under elevated FGF8 levels, anterior PSM cells maintain a shorter oscillation period, i.e. the cells slow down less during their passage through the PSM. The observed anterior shift of segment formation observed in the presence of FGF signaling over-activation could therefore reflect a prolongation of an undifferentiated, fast oscillating cell state. Further, support for a tight link between sig-

nalizing gradients and oscillation period distribution is provided by the study of *in vitro* cultures of mixed PSM cells by Tsiairis and colleagues. The authors demonstrated that cells re-establish synchronous waves after mixing. The period gradient builds up in parallel with a Wnt activity gradient as shown by the distribution of nuclear  $\beta$ -catenin levels (Tsiairis and Aulehla, 2016).

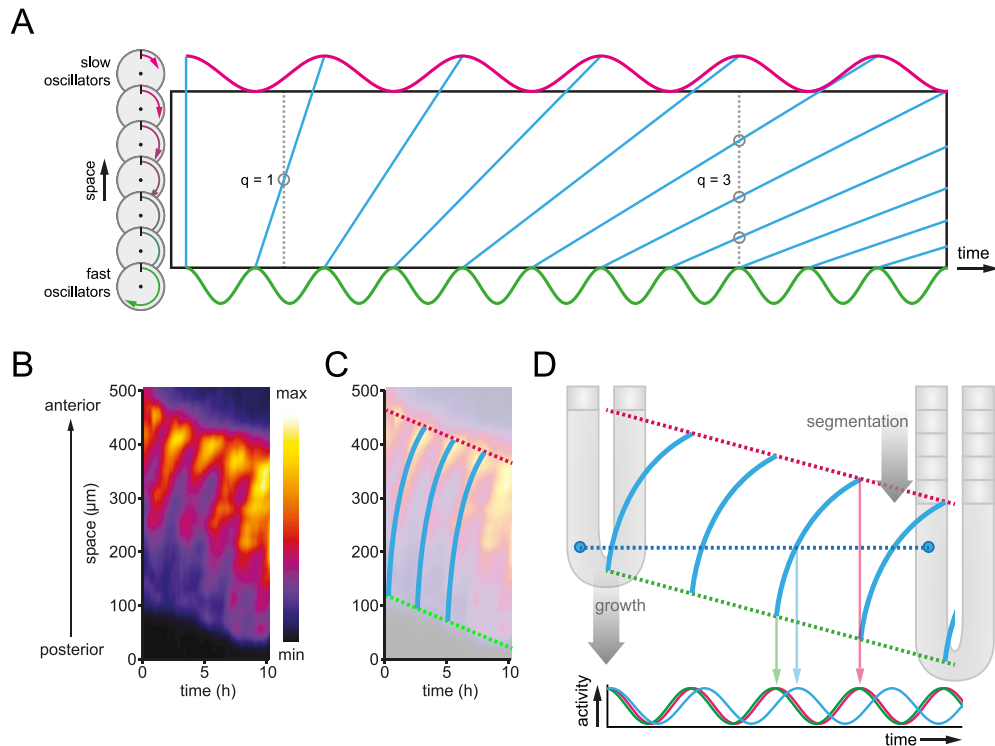


**Fig. 7: Period distribution in the PSM.** (A) Buildup of a phase gradient from an initial period gradient. Oscillators with different oscillation periods (depicted as clocks) are lined up along a spatial dimension (space) in a way that the period along the axis gradually increases. If all oscillators start simultaneously to cycle in phase, oscillations gradually drift out of phase, as illustrated by the “wave maxima” (blue) connecting the oscillatory signals at both ends of the oscillatory field (green and red). Note that at early time points only one wave traverses the field, while later, several waves travel at the same time. This property is expressed by the wave number ( $q$ ) which will be discussed further in Chapter II, section 0. (B) Kymograph along the posterior-anterior axis of a mouse embryo tail expressing a *Lfng* activity marker. Formation of a segment is marked by a bright fluorescence domain at the anterior end of the oscillating field. (C) Growth rate (green dashed line) and segmentation rate (red dashed line) are similar so that the total PSM length remains stable over several waves. The wave slope (blue lines) decreases towards the anterior, indicative for wave slowing. (D) Schematic to illustrate the occurrence of different oscillation periods in the PSM. While oscillations at a relative position in the posterior PSM (green) and close to the segmentation front at the anterior (red) have the same period, the period in an individual cell (=absolute position) moving through the unsegmented tissue (blue) grows progressively. The oscillation plot (bottom) illustrates the period difference when comparing relative and absolute PSM positions. (A)

*adapted from Kopell and Howard (1973) with permission from AAAS, (B,C) adapted from Lauschke et al. (2013) with permission from Springer Nature.*

### 3.7 Alternative segmentation models

Not all observations made in the context of PSM waves and gradients can be readily explained by the clock and wavefront model which inspired a number of modifications and alternative models.

As described above (Introduction, 3.2), the clock and wavefront model was introduced to explain scaling, predicting that the wavefront velocity adapts to the size of the tissue while the rhythm of the clock stays the same. The model was challenged by experiments done by Lauschke and colleagues in an *ex vivo* culture assay for PSM explants in which elongation of unsegmented tissue is inhibited, thus the tissue size gets progressively reduced by the formation of segments. In this setup the authors could show, using real-time reporters, that the Notch signaling waves, i.e. the clock, adapt to the shrinking size of unsegmented tissue. More precisely, Lauschke and colleagues found that the magnitude, or slope, of the phase gradient of *Lfng* scales with the size of newly formed segments (Lauschke et al., 2013). An effect of tissue size on the clock cannot readily be explained by the clock and wavefront model, leading the authors to propose that the phase gradient, independent of a determination front, could carry positional information and convey scaling.

It remains unclear from this study, how cells along the phase gradient could readout their relative position. Theoretically, Goodwin and Cohen proposed that the local phase relationship between two oscillators which have a different phase distribution along space could serve as mechanism to encode positional information in biological systems (Goodwin and Cohen, 1969): If two independent phase waves emanated from the same position in space but propagated with different phase delays from one element to the next, their oscillation phase relationship will change continuously along the direction of propagation. Such a local phase shift could be used within cells to determine their position.

In the context of the mouse PSM, such model receives support from the observation that not all clock genes display the same wave dynamics. Live imaging of *Lfng* and *Axin2* in the *ex vivo* PSM culture system mentioned above showed that the phase relationship between Wnt and Notch signaling oscillations change from out-of-phase to in-phase at the positions corresponding *in vivo* to posterior and anterior PSM, respectively (Sonnen et al., 2017). Thus, the phase shift between both oscillators changes along the axis due to different period gradients of both oscillations, fitting to the model proposed by Goodwin and Cohen. Importantly, experimental manipulation of the phase shift in the region corresponding to the anterior PSM by oscillation entrainment to an external rhythm indeed affected segmentation (Introduction, 3.3), providing first experimental support for a two-oscillator model (Sonnen et al., 2017).

The clock and wavefront and the two-oscillator model rely on a clock mechanism to convey periodicity of somitogenesis. However, the need for a clock in somitogenesis is challenged by the fact that segmentation is not completely abrogated in mutants affecting the core elements of the oscillation machinery, like in the *Hes7*-null mutant (Bessho et al., 2001). Further along this line, Dias and colleagues could show in chick that cells from the posterior PS that were grafted elsewhere in the embryo, outside the oscillating PSM, formed ectopic somite-like epithelial structures when treated with *Noggin*, a promoter of paraxial mesoderm fate (Dias et al., 2014). However, how much the observed structures, which formed in the absence of apparent oscillatory activity, actually resemble somites or rather represent a general self-organization potential of pseudo-stratified epithelial structures remains under debate (Hubaud and Pourquié, 2014).

### 3.8 Initiation of the segmentation clock

The previous sections highlight the complexity of the segmentation clock in the PSM: The system features phase and period gradients, integrates at least three partially interconnected oscillating signaling pathways of which two also form morphogen gradients across the tissue and it manages to synchronize gene activity in several thousand cells in the context of permanent growth. Taking all this into account, an intriguing question

remains how such a complex dynamic mechanism is started and how synchrony initially emerges.

### *Clock gene expression before segmentation*

Some insight into the dynamic patterns of clock genes immediately before the onset of somitogenesis comes from studies of mRNA expression snapshots in chicken and fish embryos. In chick, Jouve and colleagues found the oscillating genes *HAIKY1/2* and *LFNG* to be dynamically expressed in coherent patterns before the first somite boundary is defined (Jouve et al., 2002). Dynamic expression of cyclic genes in chick starts in parallel with the ingression of the paraxial mesoderm territory from the epiblast into the PS. Two consecutive, chevron-like expression domains initiate in the posterior PS and travel towards the node (Fig. 8A). While the tip of these chevrons show expression in PS as well as in the laterally adjacent epiblast and mesoderm layers (Fig. 8B), the extended wings consist only of epiblast tissue (Fig. 8C). The first and second chevron-like waves take about 5 h and 2 h to be completed, respectively. Following this early phase, regular posterior-to-anterior waves with a 90 min period, as described previously (Palmeirim et al., 1997), are observed in a domain including PS, mesoderm and epiblast adjacent to the PS. Each of these short-period waves is followed by a somite boundary, whereas the first two long-period patterns are not. Thus, in chick the start of segmentation seems to be preceded by two wave-like expression patterns, which are characterized by a longer period than later waves but already show spatial and temporal coherence among cells (Jouve et al., 2002).

Also in zebrafish, synchronized oscillations of Notch target genes prior to the onset of segmentation were described (Riedel-Kruse et al., 2007). At ~5.25 hours post fertilization (hpf), at the time when mesoderm induction starts (Fig. 8D), a first pulse of *her7* expression is seen in a ring of presumptive mesoderm. In total, five oscillations with ~30 min period precede the first segmentation wave at 8.7 hpf resulting in the first somite boundary (Fig. 8E,F).

Interestingly, both studies describe spatiotemporally organized induction and oscillatory expression of segmentation clock genes even before segmentation starts, prompting the question for the underlying signal. Also, it remains unclear whether cellular communi-



cation during this early phase is needed or whether cells react autonomously to an external cue.

#### *A Notch signaling independent segmentation start?*

As discussed in Introduction, section 3.2, the Notch pathway is an integral component of the segmentation clock in all studied species and is required for oscillation synchronization between cells in fish and mouse. However, in the context of initiation of synchronized PSM oscillations, Notch signaling seems to be dispensable, at least in fish. Zebrafish mutants for Notch pathway components share a phenotype of severely disrupted segmentation, yet the severity of mis-segmentation increases from anterior to posterior. The first 5–8 somites are formed relatively normally, pointing towards a Notch independent clock initiation (Jiang et al., 2000; Jülich et al., 2005; van Eeden et al., 1996). Similarly, while perturbation of Notch-mediated cell communication with DAPT during ongoing somitogenesis leads to disruption of segmentation with a fixed delay dependent on the time of DAPT addition (Introduction, 3.5), the first six somites always form normally (Riedel-Kruse et al., 2007).

In mouse, the situation is less clear. Notch signaling is needed for synchronization but has also been implicated in several other aspects of segmentation, such as refinement of segment boundaries (Koizumi et al., 2001; Morimoto et al., 2005; Takahashi et al., 2000), assignment of an anteroposterior segment polarity (Feller et al., 2008) or even as a part of the oscillation mechanism itself (Ferjentsik et al., 2009). Thus, analyzing the emergence of initial synchrony in the absence of the Notch pathway is difficult. Pathway redundancy further complicates the interpretation of mutant phenotypes. *Notch1*, *Dll1*, *Dll3* and *Lfng* loss-of-function mutants show a severe segmentation phenotype, including irregular and poorly polarized somites. However, the gradual loss of segmentation in an anterior-to-posterior direction, as seen in fish, is not so obvious in mouse (Conlon et al., 1995; Evrard et al., 1998; Hrabě de Angelis et al., 1997; Kusumi et al., 1998; Zhang and Gridley, 1998). The best-known example for an anterior-to-posterior decay of segmentation in mouse is the double knockout of *Notch1* and *Notch2*, the two Notch receptors expressed in the PSM. This mutant is reported to produce 7–9 irregular anterior somites and an unsegmented extended posterior region, thereby resembling

Notch mutants in fish (Huppert et al., 2005). Similarly, embryos lacking the Notch transcription factor RBP-J  $\kappa$  make 5–8 rudimentary anterior somites before segmentation stops. However, axis elongation is severely affected in these embryos, making it difficult to attribute the somite phenotype to the segmentation clock alone (Oka et al., 1995).

#### *Potential initial clock synchronization signals*

If Notch signaling is required for keeping cells synchronized but is dispensable for setting up initial synchrony, another signal must be responsible for starting the clock.

The expansion of FGF signaling in the mesoderm has been discussed as a potential candidate in this context. In mouse, the analysis of *Fgfr1* (Fibroblast growth factor receptor 1), *Rbp-j $\kappa$*  and *Dll1* mutants suggest that FGF signaling is required for *Hes7* oscillations in the posterior PSM while Notch signaling seems to be dispensable (Niwa et al., 2007). Further, addition of FGF to murine cell lines was shown to induce *Hes1* oscillations (Nakayama et al., 2008). In fish, the timing of the first boundary-correlated wave (wave 6 according to Riedel-Kruse et al., 2007) correlates with anterior expansion of the FGF gradient, visualized through the FGF-signaling target *spry4*. The FGF gradient expansion was estimated to occur at a similar velocity as the first somitic waves, suggesting that an FGF activation threshold traveling in anterior direction could generate the initial phase gradient of oscillations (Ishimatsu et al., 2010). Other initial synchronization signals are possible, including Wnt signaling, BMP (Bone morphogenetic protein) signaling or the mechanical and cell morphological changes imposed by gastrulation itself, but experimental evidence for any of these scenarios is lacking.

In summary, experimental results in fish and mouse argue for a Notch signaling independent initial synchronization event. In chick and fish, with the limited temporal resolution of *in situ* hybridization (ISH) snapshots, initial clock gene expression was shown to occur in a temporally coordinated pattern in mesoderm and mesoderm precursors in the PS in chick and the blastoderm margin in fish. In both species, clock genes undergo several rounds of oscillations with different dynamics before the start of segmentation. However, data on pre-segmentation clock gene dynamics in a mammalian system are completely missing to date.

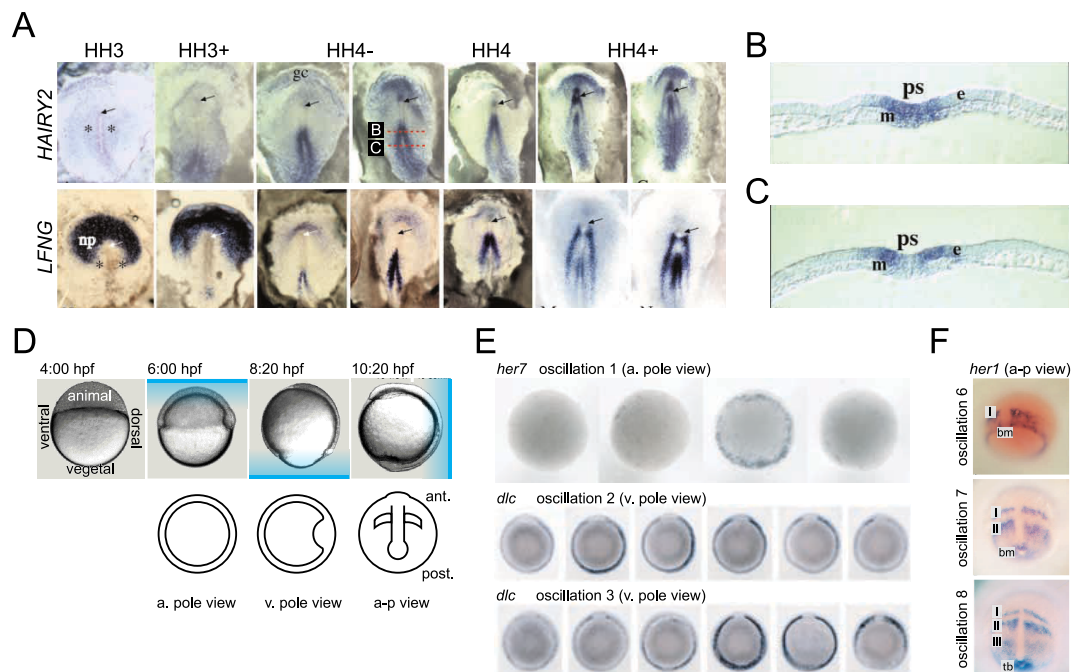


**Fig. 8: First clock-gene oscillations in chick and fish.** (A) Onset of *HAIRY2* and *LFNG* expression in paraxial mesoderm precursors of the chick embryo (anterior at the top). At stage HH3 (according to the developmental table of Hamburger and Hamilton (HH); Hamburger and Hamilton, 1992), *HAIRY2* and *LFNG* are not expressed in the presumptive territory of the paraxial mesoderm in the epiblast lateral to the PS (\*), *LFNG* shows transient expression in the neural plate (np). From HH3+ to HH4, a chevron-like expression domain of *HAIRY2* and *LFNG* sweeps from posterior to anterior along the PS. When it reaches the node (arrow) at HH4, a second chevron initiates at mid-PS and moves anteriorly towards the node. (B) Cross section at the position indicated in (A) shows that *HAIRY2* expression at the center of the first chevron includes primitive streak (ps), overlaying mesoderm (m) and adjacent epiblast (e). (C) The wings of the chevron appear to be only in epiblast. (D) Zebrafish development from blastula to the first somite to help understanding of the embryo orientations in (E,F). First row shows bright-field micrographs of the embryo in side view. Bottom row cartoons depict a projection in the direction marked with blue gradients in the row above (a., animal; v., vegetal; a-p, anterior-posterior). (E) First three oscillations of *her7* and *dlc* (*delta like C*). Note that embryos stained for *dlc* in vegetal pole view are rotated 90° compared to the cartoon in (D). (F) Snapshots of the first segmentation waves visualized by *her1* RNA. Roman numbers mark position of segmentation waves, not including the first five oscillations which do not lead to a segment (bm, blastoderm margin; tb, tailbud). (A–C) adapted from Jouve et al. (2002), and (F) from Müller et al. (1996) both with permission from The Company of Biologists Ltd; (D) modified from <https://msu.edu/~bentle48/Katie%20Graham.html> (accessed Nov 11, 2017); (E) adapted from Riedel-Kruse et al. (2007) with permission from AAAS.

## 4. Aims of the study

How does the clock start ticking? Little is known about the early dynamics of the segmentation clock in vertebrate embryos. The coarse order of events has been described for fish and chick, indicating that segmentation clock genes are active—and dynamic—long before the first somite is defined. However, the actual processes of oscillation initiation, synchronization and wave formation are poorly understood.

The high temporal and spatial resolution that can be reached with live imaging may help to understand these early clock-gene dynamics and the hierarchy of events in more detail by discovering transient patterns overlooked so far with classical methods. Further, by introducing an absolute time axis to the system, quantitative measurements of oscillation and wave characteristics such as period and phase profile can be performed, potentially advancing our understanding of the oscillator model and its coupling.

The central aim of this work was a quantitative description of the initiation of the segmentation clock in the context of the living, gastrulating mouse embryo, making use of the potential of fluorescence imaging. To achieve this, my goal was to establish a reliable experimental setup for long-term live microscopy of post-implantation mouse embryos. The setup should enable uninterrupted observation of embryos over more than 1.5 days from early gastrulation to the onset of somitogenesis at close to *in utero* quality. Knowing that mouse embryonic development is a slow process and that variability between embryos is quite large (Tam, 1981), this imaging method should further be designed for simultaneous multi-sample imaging.

Using this culture and imaging method, my aim was to describe the dynamics of signaling reporters before and during formation of the first somites to assemble a dynamic and quantitative picture of the earliest clock-gene expression patterns in the mouse. Further, I wanted to compare signaling patterns between cyclic pathways in the paraxial mesoderm, namely Notch, FGF and Wnt signaling, to assess the connectivity between those pathways during segmentation clock establishment. Finally, I aimed to challenge the

system genetically and pharmacologically to gain insight on the mechanistic level of the initial clock synchronization.

I hope the technical improvements for live mouse embryo imaging that I describe in Chapter I will be a valuable contribution for the future study of post-implantation mouse embryos in various contexts. The insight I obtained into the early dynamics of the segmentation clock, which are summarized in Chapter II, may help our understanding of the versatile ways of cellular communication and serve as an entry point for further investigations.



# **Chapter I | A toolkit for early post-implantation mouse imaging**

# 1. Results

## 1.1 Customized mounting and culture protocol for long-term imaging of the mouse gastrula

Mouse embryonic development from the onset of gastrulation to organ and somite formation takes two days. With the goal of covering the entire period by live imaging, a customized culture system and mounting method for early post-implantation mouse embryos was developed on the basis of a commercially available light-sheet microscopy system (Lightsheet Z.1, Carl Zeiss; Fig. 9A).

First, I introduced an additional embryo culture chamber into the standard Z.1 sample chamber (Fig. 9B) to reduce volume and surface of the medium body. The culture chamber has a 180° window covered with a 50 µm-thin fluorinated ethylene propylene (FEP) membrane to allow illumination light to reach the sample and fluorescence to be collected by the detection objective. FEP is routinely used as tubes (Kaufmann et al., 2012) or membranes (Strnad et al., 2016) to facilitate mounting in light-sheet microscopy because of its refractive index which is close to that of water. In my hands, the additional chamber, which can be cleaned effectively with ethanol, dramatically reduced early experiment termination or failure due to medium contamination. In addition, only the embryo culture chamber was filled with culture medium while the outside sample chamber contained PBS. The reduced volume helped to keep experiment costs down as mouse embryos at gastrulation stage are routinely cultured in 50–100% of costly primary rat serum.

Second, to ensure a controlled, gradient-free gas distribution within the medium column, the embryo culture chamber was connected to a closed-cycle medium-perfusion system. The medium was pumped through a gas equilibration chamber in which the saturation with N<sub>2</sub>, O<sub>2</sub> and CO<sub>2</sub> was fully controlled, before entering the embryo culture chamber (Fig. 9C). Availability of O<sub>2</sub> during development in the uterus changes from



hypoxic conditions during pre-implantation, to normoxic conditions after the placenta has fully developed. Accordingly, best culture results are achieved in rotating bottle culture by adjusting the O<sub>2</sub> content of the gas mix to the age of embryos (Rivera-Pérez et al., 2010). I adapted this for the microscope and cultured embryos at E6.5 in 6% O<sub>2</sub> and switched to 20% O<sub>2</sub> on day seven.

Finally, the sample mounting strategy was modified to allow for unperturbed growth of the embryo. Within two days from early gastrulation, the mouse embryo grows from about 300 µm to >2 mm in diameter. Classical mounting in a stiff gel column inhibits growth and is thus not feasible for post-implantation mouse embryos. I employed a mounting method in which only the ectoplacental cone at the proximal tip of the embryo is embedded in an agarose gel, while the actual embryo is freely immersed in medium, like a lightbulb in its socket. This configuration was achieved by first embedding the entire embryo in low melting agarose and subsequently peeling off any agarose around the embryonic body (Fig. 9D). While the tissue of the ectoplacental cone does not significantly grow during culture, the embryo could expand freely and was in direct contact with the surrounding medium. As an additional benefit, the light path was not impeded by a gel or tube.

Using this modified mounting and culture setup for a light-sheet microscope, I successfully cultured and imaged embryos for 40 hours, from early gastrulation at E6.5 to up to 10 somites at E8.5 (Fig. 9E; Movie 1). The quality of embryo development on the microscope was assessed using morphological and molecular markers. Cultured and *in utero* developed embryos generated somites, head fold, heartbeat and vasculature at comparable proportions. Further, they showed characteristic expression patterns of *Msgn1* (Mesogenin 1), a marker for paraxial and presomitic mesoderm, *Shh* (Sonic hedgehog), a neural marker expressed in notochord and basis of the neural tube, and *Uncx4.1* (UNC homeobox) marking the anterior–posterior subdivisions of the somites (Fig. 9F). The comparison of embryos developed *in utero* and cultured on the microscope to E8.5 further indicated that no major developmental delay was inflicted by our protocol, given the naturally occurring variation of developmental progress even among embryos of the same litter (Tam, 1981).

Combined, this customized, yet simple to implement, setup enables long-term culture and imaging of gastrulation-to-organogenesis stage mouse embryos.

## 1.2 Multi-sample imaging with SPIMfor4

A bottleneck of long-term imaging studies on a light-sheet microscope like the Z.1 is the low throughput of generally one sample per experiment. This not only limits the amount of data collected per experiment but also prevents comparative studies between different samples in the same experiment. Two publications have addressed this issue for plant root and E6.5 mouse embryo imaging by developing multi-sample holders that are compatible with the Z.1 mounting method (de Luis Balaguer et al., 2016; Ichikawa et al., 2013). However, both approaches lack the possibility to adjust the sample orientation after mounting on the microscope. This is essential for mouse embryos after E6.5 as the tissue becomes highly scattering, preventing whole embryo imaging from an arbitrary orientation. For example, imaging expression dynamics at the posterior side of an embryo requires this side to be turned towards the detection objective.

I developed “SPIMfor4”, a multi-sample holder that holds up to four samples in separate capillaries, each of which can be turned individually to orientate the samples prior to imaging (Fig. 9G). The four sample capillaries are arranged in a revolver that can be inserted into the sample holder disc for syringes that comes with the Z.1. With the help of a tube cap and the respective key, each capillary is turned manually to adjust the position of the sample relative to the objectives. Importantly, the SPIMfor4 is compatible with the embryo culture chamber described above. The configuration of sample tubes ensures that while one sample is imaged, none of the other samples blocks the light-sheets or detection path (Fig. 9H). Switching between samples is accomplished by the standard rotation drive of the Z.1 microscope stage and takes ~2 sec. I surveyed the influence of revolving the sample holder on positional stability of each sample and could confirm that no noticeable additional movement was introduced relative to single-embryo imaging (Fig. 9I).

Thus, the SPIMfor4 is a simple device to quadruplicate the data acquired per time-lapse experiment without compromising data quality and is readily compatible with the Light-sheet Z.1 microscope.

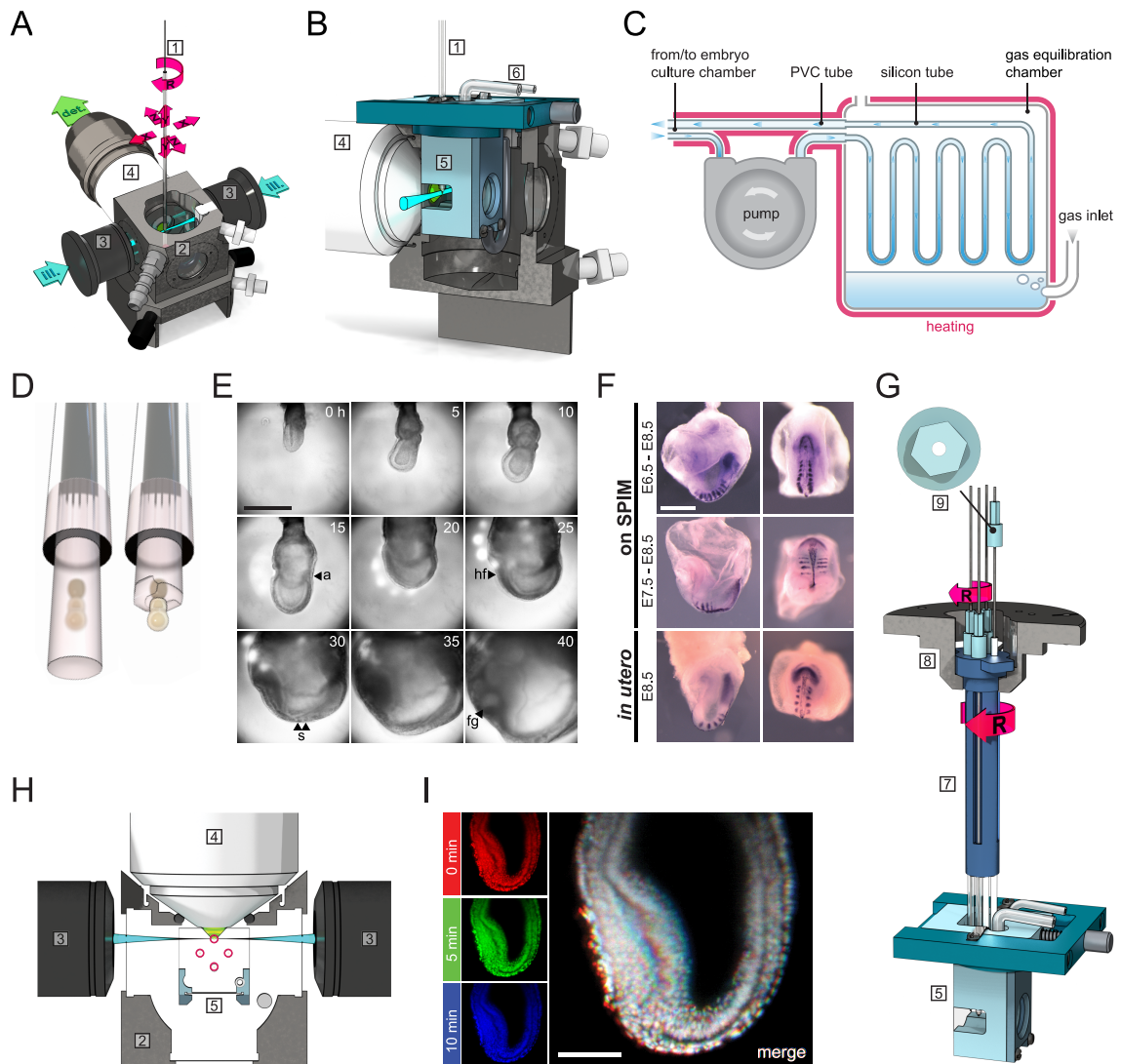


**Fig. 9: Optimization of light-sheet microscopy for multi-sample live imaging of mouse embryos from gastrulation to organogenesis.** (A) Objective and sample mounting assembly of the Lightsheet Z.1 from Zeiss. Samples are mounted in a tube or capillary (1) installed on a translation (X,Y,Z) and rotation (R) stage and suspended into a liquid-filled sample chamber (2). Two illumination (ill.) lenses (3) produce light-sheets from either side of the sample; one detection objective (4) collects the fluorescence. (B) Horizontal section view through the sample chamber with inserted embryo culture chamber (5). The embryo culture chamber consists of a chamber lid (dark blue) and the chamber body (light blue) with membrane-covered windows for the light paths. It is connected *via* tubes (6) to the closed-cycle perfusion system depicted in (C) to circulate and equilibrate the culture medium. (C) From the embryo culture chamber, medium is pumped through a gas equilibration chamber to be saturated with a defined gas mixture. Thin-walled, gas permeable silicon tubes are used inside the equilibration chamber, thick PVC tubes are used outside. The entire system is heated (indicated in red). (D) Two tubes with embryos. (E) Time-lapse sequence of embryo development from 0h to 40h. Labels 'a', 'hf', 's', and 'fg' indicate specific features. (F) Fluorescence images of embryos at different stages: 'on SPIM' (E6.5-E8.5, E7.5-E8.5) and 'in utero' (E8.5). (G) Vertical section view of the sample chamber assembly with numbered components (5-9). (H) Schematic of the light-sheet illumination setup with numbered components (2, 3, 4). (I) Fluorescence images at 0, 5, and 10 minutes, with a 'merge' image and a scale bar.

For mounting, first, embryos are embedded in an agarose gel in a glass capillary (left), then the gel is removed with forceps from most of the embryo, except for the ectoplacental cone to enable growth as shown in (E) for a 40 h time-lapse experiment. (E) Bright-field images of an embryo developing on the customized light-sheet microscope (anterior to the left). Experiment starts at E6.5 during MS stage. Morphological features indicative for stereotypic development are the formation of the allantois (a), the head fold (hf), somites (s), and a foregut pocket (fg). Scale bar: 500  $\mu\text{m}$ . (F) RNA expression pattern in embryos after culture on the microscope in comparison to freshly dissected controls (E6.5-E8.5: n=3; E7.5-E8.5: n=8, E8.5: n=8). All embryos were stained for *Msgn1*, *Shh*, and *Uncx4.1*. Representative embryos are shown in lateral view (left; anterior to the left) and distal view (right; anterior down). Scale bar: 500  $\mu\text{m}$ . (G) The SPIMfor4 multi-sample holder (7) is placed in the Z.1 standard sample holder disc for syringes (8). A capillary cap is glued to the top of each capillary (9; top view shown above). With a hex key, each capillary can be turned individually (small R) and the rotation drive of the microscope stage is used to switch between samples (large R). (H) Horizontal slice view at the sample level (red circles) through the imaging setup with embryo culture chamber and SPIMfor4 in place. (I) Image stability test with multi sample imaging. An E6.5 mouse embryo expressing R26-H2BmCherry was imaged in a multi-sample imaging routine. Three consecutive frames of the same imaging location are shown (left). In between these frames, three other embryos were imaged (not shown). Frames were color coded in red, green, and blue and overlaid (right) to visualize positional stability. Pixels with the same intensity in all three images appear white. The visible shift is due to morphological changes of the embryo. Scale bar: 100  $\mu\text{m}$ . *CAD drawings of Z.1 microscope parts provided by courtesy of Carl Zeiss Microscopy GmbH.*

### 1.3 Single-cell tracking in the embryo with mosaic labeling

One aim of establishing post-implantation mouse embryo imaging on a light-sheet microscope was to monitor development simultaneously on tissue and cellular levels, taking advantage of the high 3D resolving capacity across large fields of view of such system.

In order to follow individual cells over time, it is important to attain unambiguous identification of single cells, as well as high imaging rates to establish track relations between objects in consecutive time frames. Obtaining cellular resolution throughout the tissue layers of the post-implantation mouse embryo is challenging because the tissue is highly scattering, and growth causes optical properties to change over time. In addition, tracking is complicated by the mouse embryo's high photosensitivity which limits achievable frame rates.

To simplify object identification in the densely packed, scattering embryo, I adopted a cell labeling strategy based on mosaic marker expression. As for single molecule localization techniques, localization of fluorescent objects is simple if they are far apart from each other (Sauer and Heilemann, 2017). This approach also increases the reliability of object tracking at comparatively low frame rates, as long as objects move significantly less than the distance to their nearest neighbor between consecutive frames. To obtain sparse cellular labels, I combined the Cre-ERT2 allele, which provides ubiquitous tamoxifen-inducible Cre activity (Ventura et al., 2007), with the R26R-Confetti reporter (Snippert et al., 2010). The R26R-Confetti reporter is based on the Brainbow2.1 cassette, inserted into the ROSA26 locus. Like Brainbow2.1, it creates a stochastic choice of expression between four fluorescent proteins (CFP, GFP, YFP, RFP) under the control of the Cre-loxP recombination system (Livet et al., 2007). With the help from Sonja Nowotschin in the group of Anna-Katerina Hadjantonakis at the Sloan Kettering Institute, New York, I managed to obtain sufficiently sparse cell labeling in embryos from females treated with tamoxifen a low dose of tamoxifen during pregnancy.

Embryos were imaged from multiple angles to ensure high-resolution coverage of the entire sample. In collaboration with Marvin Albert and Christian Tischer (both from European Molecular Biology Laboratory; EMBL), a data processing workflow was developed to combine the image stacks, register the fused dataset, segment labeled cells and finally track these cells over time. Image fusion and registration was done using custom algorithms, for segmentation and tracking I used Ilastik (Sommer et al., 2011) and Imaris (Bitplane), respectively (Materials and methods, 6).

An example of a Cre-ERT2;R26R-Confetti embryo processed with our tracking workflow is shown in Fig. 10. Tamoxifen was injected into the pregnant female on day six *post coitum* and the embryo was dissected and imaged on E7.5 for 15 h from multiple angles (Fig. 10A; Movie 2). I used the RFP label of the R26R-Confetti line for tracking. Resulting tracks of RFP-labeled cells recapitulated the general expansion of the embryo as well as an invagination movement at the anterior, marking the formation of the head fold (Fig. 10B,C; Movie 3). Importantly, 435 tracks with a duration of 7 h or longer were obtained, indicating, that our approach enables us to follow a substantial number of cells over many hours of development (Fig. 10D). The distribution of tracked cell

movement speed peaked at  $0.25 \mu\text{m min}^{-1}$  and for 95% of all tracked location changes between consecutive frames the speed was below or equal to  $0.75 \mu\text{m min}^{-1}$  (Fig. 10E). Consequently, at the chosen time resolution of 8 min, assuming a cell diameter of  $\sim 12 \mu\text{m}$ , most cells moved less than half of their diameter between two frames. This represents an important prerequisite for reliable tracking based on feature overlap, indicating that 8 min imaging interval is appropriate for tracking experiments in the gastrulating mouse embryo.

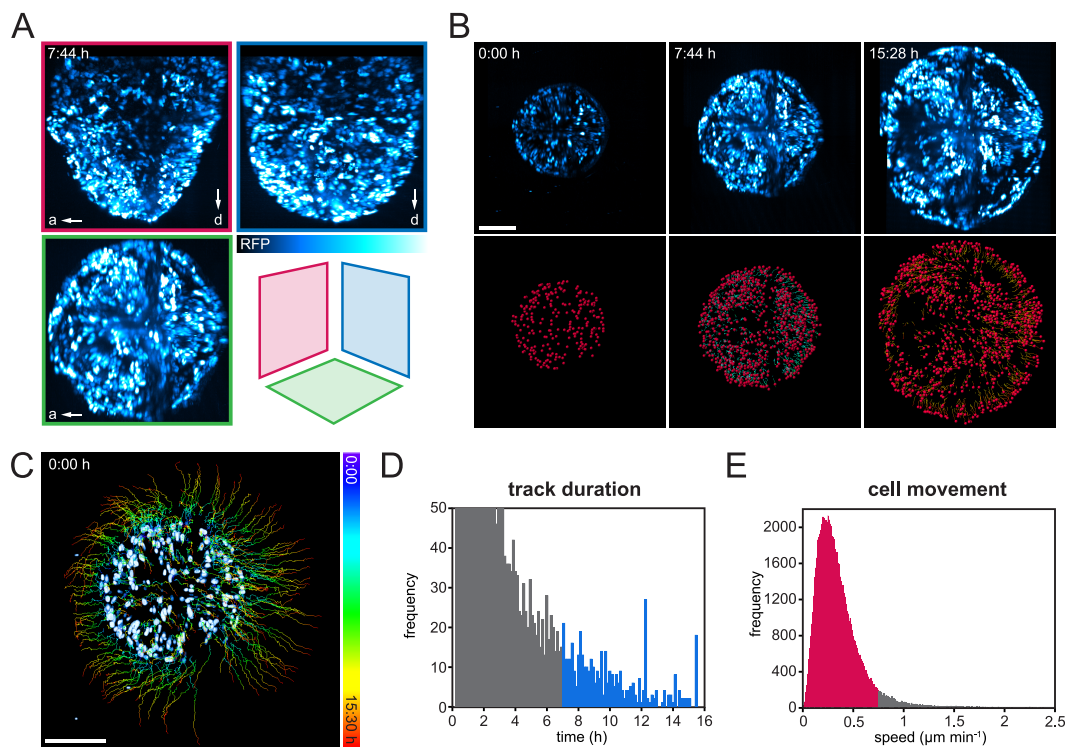


**Fig. 10: Tracking of sparsely labeled cells in the post-implantation embryo.** An E7.5 Cre-ERT2;R26R-Confetti embryo was imaged for 15 h from three angles on the Lightsheet Z.1 microscope. (A) Still frame of the fused and registered 3D dataset, maximum-projected along the three spatial axes as indicated by the frame color. The cytoplasmic signal of RFP is shown, and the embryo projections are oriented as indicated (a, anterior; d, distal). (B) Time series of the dataset shown in (A) in proximodistal projection, anterior to the left. The top row shows the intensity image, the bottom row shows segmented and tracked cell objects with their corresponding tracks over the last 20 frames. (C) The first frame of the dataset as in (B) is depicted together with all tracks longer than 7 h. Tracks are time-color-coded according to the color bar. (D) Histogram of track duration. Tracks longer than 7 h as shown in (C) are marked in blue. (E) Histogram of cell displacement speed of all tracks calculated between consecutive frames. Marked in red are all tracked location changes between consecutive frames in which the speed was below or equal to  $0.75 \mu\text{m min}^{-1}$ . All scale bars:  $200 \mu\text{m}$ .

## 2. Discussion

### 2.1 Updating a commercial light-sheet microscope for mouse embryos

In this chapter, the development of an extension to the commercial Z.1 light-sheet microscope for multi-sample post-implantation mouse embryo imaging has been described. The method enables the continuous observation of development from early gastrulation for up to two days, which is at present unsurpassed in the field.

The use of a commercially available light-sheet microscope as basis for the development grants easy access to the method for application-focused, non-developer laboratories. The embryo-culture chamber and perfusion system I designed are easily integrated into the existing Z.1 framework without any changes to the hardware or software configuration. Because the culture system is entirely isolated from the Z.1 sample chamber, the parallel use with different model systems, e.g. mouse and fish, is possible without extensive cleaning/sterilization of the culture medium-contacting parts. This may be of interest for instance in a microscopy facility with multiple users. The perfusion system guarantees a well-mixed medium body and an efficient control of the gas composition of the medium. The mounting method presented here gives a high degree of control over the embryo orientation and is especially suited to monitor processes along the proximodistal embryo axis. The combination with the SPIMfor4 multi-sample holder enables a substantial increase of experimental throughput for long-term experiments. This makes phenotyping studies on the microscope more feasible and allows for control samples and experimental conditions in the same experiment, as long as all embryos share the same body of medium.

The culture system is readily usable to address diverse biological questions in the gastrulation-to-organogenesis mouse embryo and should also be adaptable to other mammalian embryo systems as well as other *in vitro* culture systems, such as organoids. The

SPIMfor4 may be of use for an even larger light-sheet imaging community, since in principle it is suitable for any sample that can be mounted in a vertical capillary or tube of a diameter  $<3$  mm.

### *Different approaches to post-implantation embryo imaging*

Two other approaches to live post-implantation mouse embryo light-sheet imaging have been developed in recent years (Ichikawa et al., 2013; Udan et al., 2014). Between these two techniques and the one described here, there is little difference in the basic culture conditions which are based on protocols developed for static or rotating bottle embryo culture (Tam, 1998). How these conditions are realized on the microscope, however, is quite different among the three techniques. My aim was to image the PS region of a large number of embryos for the full period from early gastrulation to somitogenesis, which takes  $\sim 1.5$  days. After a number of initial trials, I decided not to adapt and build upon one of the previously published methods for a number of reasons I will summarize in the following.

First, both previously described methods are limited in the freedom to orientate the sample. Ichikawa and colleagues described a sample holder in which multiple samples can be mounted by pushing the embryos' ectoplacental cone into horizontal holes (Fig. 2A). This way, the distal embryo pole points towards the detection objective, a configuration in which the activity at the PS on the posterior side of the embryo is difficult to monitor. Also, it has been reported that samples tend to fall out or distort when cultured for  $>8$  h in such configuration (Udan et al., 2014). Udan and colleagues mounted embryos in little hollow cylinders made from agarose instead (Fig. 2D,E). This way, samples can be rotated using the Z.1 rotation stage, but the side on which the embryo comes to lie in the cylinder is difficult to control, again preventing access to the area of interest in some cases. Further, multi-sample mounting is not provided with this method.

Second, in both methods serum-containing medium is in direct contact with the face of the objectives and the sample chamber which, in my experience, bears a high risk of contamination during experiments, especially when the experiment duration exceeds 20 h. Lastly, without active mixing I found it difficult to achieve a gradient-free gas dis-



tribution in the medium column, which complicates the control of e.g. pH and O<sub>2</sub> concentration in the vicinity of the embryos.

The setup I established addresses many of the aforementioned problems and enabled me to gain detailed insight into signaling dynamics during gastrulation, which I will report on in Chapter II of this work.

## 2.2 Tracking of sparsely labeled cells and its application

I demonstrated a method for single cell tracking on the basis of mosaic cell labeling in the growing mouse embryo. The use of a sparse cell label significantly simplifies cell segmentation in the dense, scattering tissue of the embryo (Ivanovitch et al., 2017), allowing to use “off-the-shelf” segmentation and tracking tools for the analysis. I was able to show that the method is suitable for long-term cell tracking as E7.5 embryos tolerated the light dose imposed by multi-angle imaging for 15 h without visible developmental impairment and the image processing and tracking workflow produced several hundreds of multi-hour cell tracks.

The experiment described in Fig. 10 is to be understood as general proof of concept. An interesting application would be possible in the context of the origin of oscillations in the mouse PSM covered in Chapter II. One important question is how oscillations start at the single cell level. This could be addressed by tracking cells that are double labeled with a sparse cell marker and a dynamic signaling reporter. To reliably identify single cell oscillations with a ~2 h period, long track duration of >4 h are desirable. The tracking workflow presented here is capable of generating a large number of long tracks and is therefore well suited for such an application. A detailed analysis to evaluate the tracking accuracy remains to be done.

For the proof of concept study presented here, the R26R-Confetti was used for labeling. However, for future dual reporter experiments, single-color Cre-inducible cell markers are more suitable. In this context, mouse lines with fluorophores emitting in the infrared spectrum would be especially useful (Filonov et al., 2011; Shcherbo et al., 2010; Shu et al., 2009). Excitation and emission maxima of these fluorophores lie well outside the

spectral range of most popular reporters, allowing high flexibility in the choice of markers to combine. In addition, long-wavelength excitation light is less harmful to the tissue and penetrates deeper than light of the visible spectrum (Pantazis and Supatto, 2014).

There are many other possible applications for the workflow in which it suffices to track a subset of cells. This could include the construction of embryonic fate maps of unmatched detail, the tracing of stem cell and progenitor cell populations, and the study of morphological tissue movements, among many other possibilities.

## **2.3 Outlook: multi-embryo multi-angle post-implantation imaging**

The realization of multi-embryo imaging on the Z.1 discussed in the first part of this discussion is limited in two aspects. First, the spatial constraints of the Z.1 restrict the number of embryos that can be mounted in a configuration like the SPIMfor4 to four only. Second, individual sample rotation is done manually, which means that automatic multi-angle imaging as needed for *in toto* acquisition is not possible for more than one embryo at once. In addition to spatial constraints, limited possibilities to interface with the acquisition software and hardware control of a commercial system like the Z.1 make the implementation of automated multi-sample rotation unfeasible. To satisfy these extended needs, I designed a multi-embryo multi-orientation (MEMO) sample holder for a dedicated post-implantation embryo light-sheet microscope. The basic concept of the MEMO sample holder has been filed for patent recently (Falk et al., 2017a). In this outlook I want to outline the MEMO sample holder concept and a possible implementation.

The general configuration of the Z.1—one detection objective, two illumination objectives arranged in a horizontal plane, and mounting from the top in a vertical capillary or tube—was found to work well for post-implantation embryos and is maintained for the MEMO sample holder concept in a post-implantation embryo light-sheet microscope. Further, in the MEMO sample holder samples are arranged in a revolver, like in the SPIMfor4, which allows for fast switching between samples while sample capillaries are secured in the ducts of the revolver.

To overcome the limitation to four samples only, the first problem was how to arrange a larger number of embryos in relation to the light paths. The space between objectives in a three-objective configuration is very limited, and if many samples are arranged in a revolver with a small diameter, like the SPIMfor4, they interfere with the path of the light-sheets (Fig. 11A). I therefore decided to introduce two levels for keeping the embryos: one in the plane of the light paths for the currently imaged sample, and one above the objectives for the stored samples (Fig. 11B). A vertical stage, also used for positioning of the sample along the Y-axis (for axes orientation, please refer to Fig. 11C), pushes the capillary cap affixed to the top of each sample capillary down against a coil spring, lowering the sample to the imaging position (Fig. 11D–F). To accomplish automated individual sample rotation, a rotation stage is integrated in the Y-translation arm (Fig. 11D). The force generated by pushing the capillary cap down against the coil spring mechanically couples the output element of the rotation arm with the capillary cap and enables rotation of an individual capillary in the imaging position (Fig. 11E,F).

After imaging one sample, the Y-translation arm moves up and the spring pushes the capillary back to the revolver level. The rotation arm output element detaches from the tube cap and a second rotation stage turns the sample revolver to switch to the next sample. The Y-translation/rotation arm and the revolver with its rotation mechanism are arranged together on a horizontal XZ-translation stage. Thus, all samples are moved together in X and Z but only the selected capillary for imaging is rotated and moved in Y (Fig. 11G).

A medium-filled sample chamber encloses the sample holder and the objectives. It also has two levels, one for the samples in the storage position and one at the level of the light paths for the sample in the imaging position (Fig. 11D,F,G).

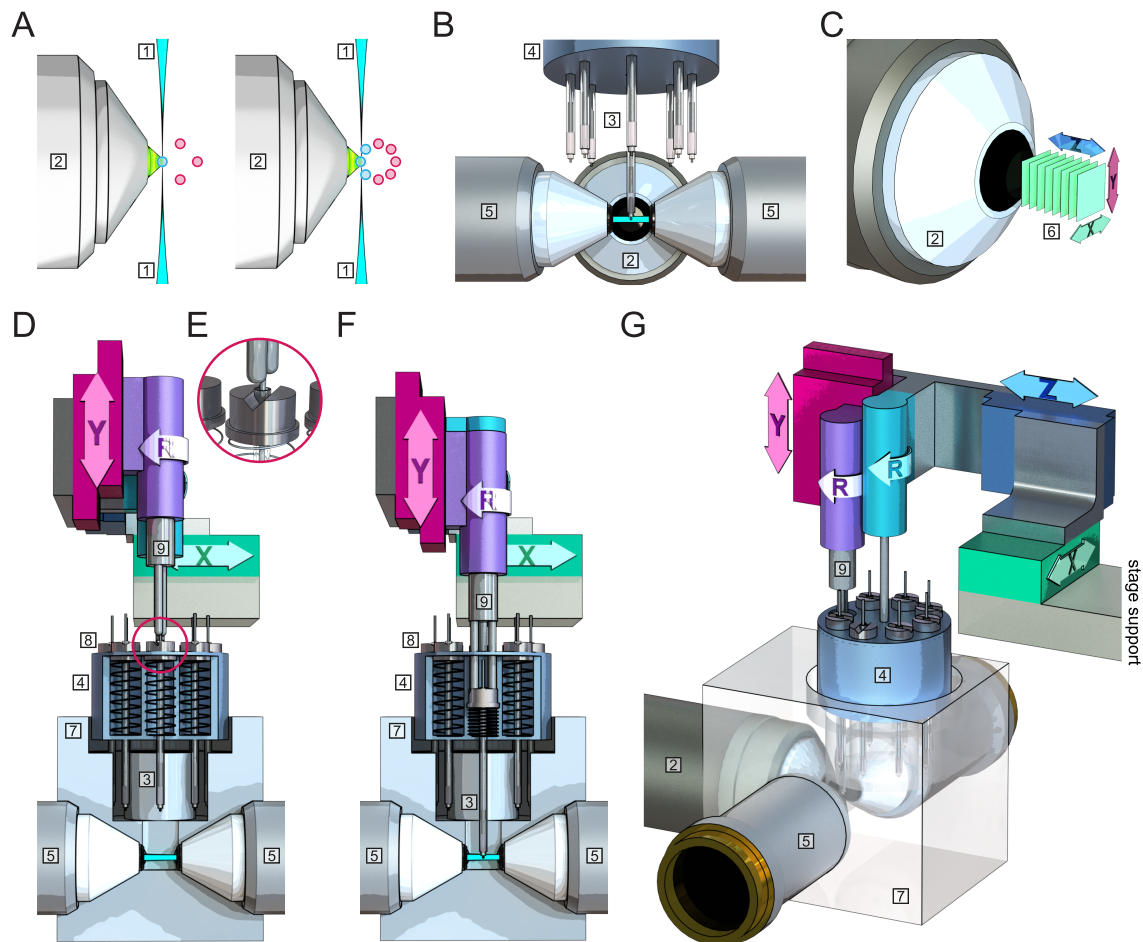


**Fig. 11: The MEMO sample holder concept for light-sheet imaging.** (A) Steric constraints of the SPIMfor4 sample configuration. In the current implementation of the SPIMfor4 multi-sample holder (left), four samples (blue and red circles) are arranged in a small-diameter revolver. The light-sheets (1) illuminate only the sample (blue) which is positioned in the focus of the detection objective (2). With more samples in the revolver (right), the access of light-sheets to the sample in focus would be partially blocked by adjacent samples. (B) Two-level configuration of the MEMO sample holder concept. All sample capillaries (3) are held by a revolver (4). Only the currently imaged sample is positioned at the level of the illumination (5) and detection objectives (2) while the other samples are stored above the objectives. (C) Axes orientation of image stacks (6) in respect to the detection objective (2). (D–F) Individual sample ejection and rotation mechanism with all capillaries (3) on the storage level (D) or one capillary pushed down to the imaging level (F). A cross-section through the sample chamber (7) and the sample revolver (4) is shown from the side of the detection objective. Coil springs in the sample revolver push against the capillary caps (8) on top of each sample capillary to hold the samples on the storage level. The output element (9) of the rotation stage (R; violet) is connected to the Y-translation stage (magenta). With this Y-translation/rotation arm, samples can be rotated and pushed towards the imaging level. (E) shows a detail of the capillary cap and rotation stage output element circled in (D). (G) Overview of the MEMO sample holder arrangement. The Y-translation/rotation arm (magenta, violet) and the rotation stage (cyan) to turn the sample revolver (4) are jointly mounted on a horizontal XZ-translation stage (blue, green). The sample chamber (7; made transparent for display) leaves enough room for the sample revolver to move in the XZ-plane.

Together, the MEMO sample holder would allow imaging of multiple samples from several angles during a time-lapse experiment. In the two-level configuration, the size of the sample revolver and the number of contained samples is virtually not constrained, in practice—depending on the desired imaging interval—8–10 embryos may be feasible. To my knowledge, this design describes the first multi-sample light-sheet microscope implementation enabling such a high degree of flexibility. It could therefore significantly improve high-throughput, high-content embryo imaging, optimizing the use of experiment time and available samples.



**Chapter II | Prelude to  
somitogenesis: start of the  
segmentation clock**

# 1. Results

## 1.1 *Lfng* expression from gastrulation onset to formation of the first waves

I employed the customized embryo culture and mounting protocol in combination with the SPIMfor4 multi-sample holder described in Chapter I, sections 1.1 and 1.2 to examine how the segmentation clock is initialized and when during the gastrulation process synchronized signaling oscillations originate. As clock readout, I used a dynamic Notch signaling reporter mouse line, LuVeLu (Aulehla et al., 2008). The LuVeLu construct consists of a destabilized Venus fluorescent protein (a variant of the yellow fluorescent protein with fast maturation kinetics; Nagai et al., 2002) under the control of the *Lfng* promoter sequence that is known to drive oscillatory expression in the PSM (Cole et al., 2002; Morales et al., 2002). Imaging this reporter on the optimized light-sheet setup, I was able to follow LuVeLu dynamics in time-lapse for more than 35 h starting at early gastrulation. Importantly, this allowed me to monitor the onset of synchronized signaling oscillations during this period (Fig. 12A; Movie 4).

LuVeLu reporter activity in E6.5 embryos was visible as early as the ES–MS stages on the posterior side of the egg cylinder, close to the embryonic/extra-embryonic boundary, suggesting that expression correlates with the induction of mesoderm. Indeed, optical transverse sections through the embryo proper revealed that LuVeLu fluorescence was exclusively found in the PS and nascent mesoderm but not in epiblast (Fig. 12B–D). The expression domain expanded concomitantly with the anterior movement of mesoderm wings, covering most of the egg cylinder at early allantois bud (EB) stage.

In parallel to the progressive area increase of the LuVeLu-positive domain due to mesoderm expansion, the first synchronized activity was detected at EB stage when fluorescence throughout the LuVeLu expression domain suddenly increased. After this increase in activity, referred to as the “pulse” from here on, expression transitioned to a



distinct stripe lateral to the node at late allantois bud (LB) stage. Shortly after, wave-like activity patterns commenced, starting at the root of the allantois and sweeping along the primitive streak towards the distal tip of the embryo, stopping with a bright stripe lateral to the midline at the level of the node (Fig. 12A; Movie 4).

To reduce data dimensionality, kymographs (line intensity profiles over time) along the direction of traveling waves were used for oscillation analysis (Fig. 12E,F). I found the first, faint LuVeLu oscillation to occur 267 min (median; 47 min interquartile range, IQR) after the intensity maximum of the pulse. More oscillations followed at regular  $\sim$  145 min intervals (Fig. 12G,H; Movie 5).

To validate LuVeLu as a faithful reporter for *Lfng* gene activity not only in segmentation stages but also during gastrulation, two strategies were followed. First, endogenous *Lfng* mRNA expression was analyzed in stage-matched mouse embryos collected between E6.5 and E8.5 (Fig. 13A). The *Lfng* expression patterns were found to be similar to the LuVeLu fluorescence patterns described for time-lapse experiments (Fig. 12). Especially strong staining was observed in EB stage embryos, reminiscent of the LuVeLu pulse observed at a similar developmental stage. Similarly, a stripe lateral to the node was observed in slightly older embryos and expression domains of variable strength and position along the proximodistal axis were found among embryos at head fold stages, indicating the occurrence of traveling waves.

Second, I compared dynamic LuVeLu activity to a knockin reporter in the endogenous *Lfng* locus (*LfngT2A3xVenus*) that was generated in our laboratory. *LfngT2A3xVenus* is a C-terminal knockin, consisting of three concatenated mVenus fluorophores (Venus with monomerizing A206K mutation; Rizzo and Piston, 2005) for improved signal strength, joined to a PEST sequence for short protein half-life. The construct is connected to the *Lfng* gene by a T2A sequence to generate two independent proteins from the same mRNA based on a ribosomal skip mechanism (Fig. 13B; Materials and methods, 1.1; Szymczak et al., 2004). While overall reporter intensity was lower for the knockin, expression domains and dynamics matched those observed with LuVeLu with clear evidence for pulse and wave-patterns in PS and nascent mesoderm cells (Fig. 13C–G; Movie 6).

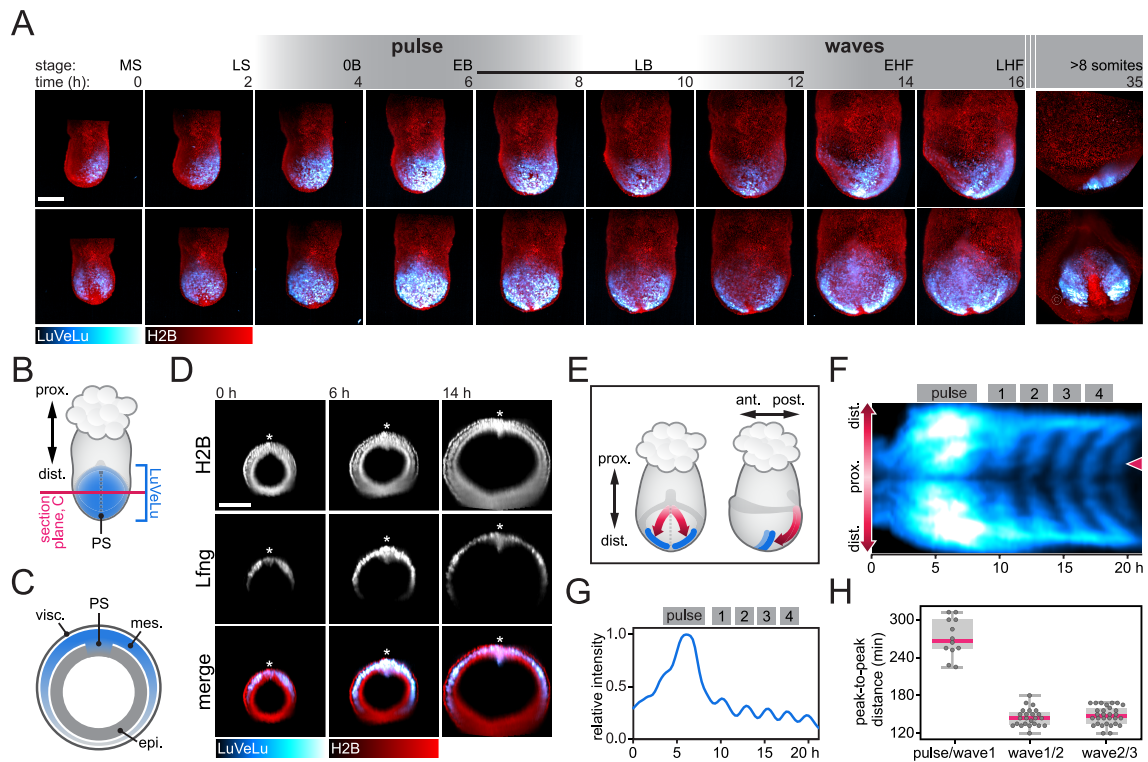


**Fig. 12: LuVeLu expression patterns during gastrulation.** (A) Still frames of a representative LuVeLu;R26-H2BmCherry embryo imaged for 35 h starting at early gastrulation (n=12 similarly imaged embryos). Image stacks are shown as maximum intensity projection (MIP) in lateral orientation (top, anterior to the left) and from posterior (bottom). Embryonic stages specified at the top: mid streak (MS), late streak (LS), no allantois bud (OB), early allantois bud (EB), late allantois bud (LB), early head fold (EHF), late head fold (LHF). LuVeLu intensity peaks after 6 h (pulse) and waves become visible after 14 h. To evaluate the distribution of LuVeLu expression among tissue layers, optical transverse sections through embryos at 50% of the proximodistal (prox., proximal; dist., distal) extend of the LuVeLu domain, as illustrated in (B) and (C), are shown in (D). The embryo at this stage consists of three tissue layers (C): visceral endoderm (visc.), mesoderm (mes.) and epiblast (epi.). At the primitive streak (PS), epiblast cells delaminate and migrate into the mesoderm layer. In (D), the three germ layers can be distinguished in the nucleus (H2B) channel by the gap between layers. The PS (marked with asterisk) is characterized by the loss of mesoderm and epiblast layer separation due to degradation of the basement membrane between both tissue sheets. (E) Cartoon of E7.5 embryo in posterior view (left) and side view (right) to illustrate domain and directionality of early waves (red arrows) in paraxial mesoderm (PS, dotted line). Early somite boundaries are depicted in blue (ant., anterior; post., posterior). (F) Intensity kymograph of LuVeLu expression of another representative embryo along the direction of waves showing the pulse and the first waves. As illustrated by the red double arrow in (E, left), an inverted u-shaped line profile was measured in the embryo and plotted as straight vertical line in the kymograph. The proximal LuVeLu domain thus is in the middle and the distal domains left and right of the PS are displayed above and below. (G) Horizontal line profile through the kymograph in (F) at the position indicated with the red arrowhead. (H) Boxplot showing the peak-to-peak intervals between pulse and the first three waves measured in profiles as shown in (G) for different embryos. Time intervals (given as median with IQR) from pulse peak to wave 1: 267 min (46.5 min, n=12), from wave 1 to wave 2: 144 min (17.7 min, n=24), from wave 2 to wave 3:

147 min (25.2 min, n=30). Sample sizes differ between measurements because the start of the imaging experiment varied in respect to the developmental stage of the embryos. Consequently, some embryos were already too far developed to capture e.g. the pre-segment pulse. All scale bars: 200  $\mu\text{m}$ .

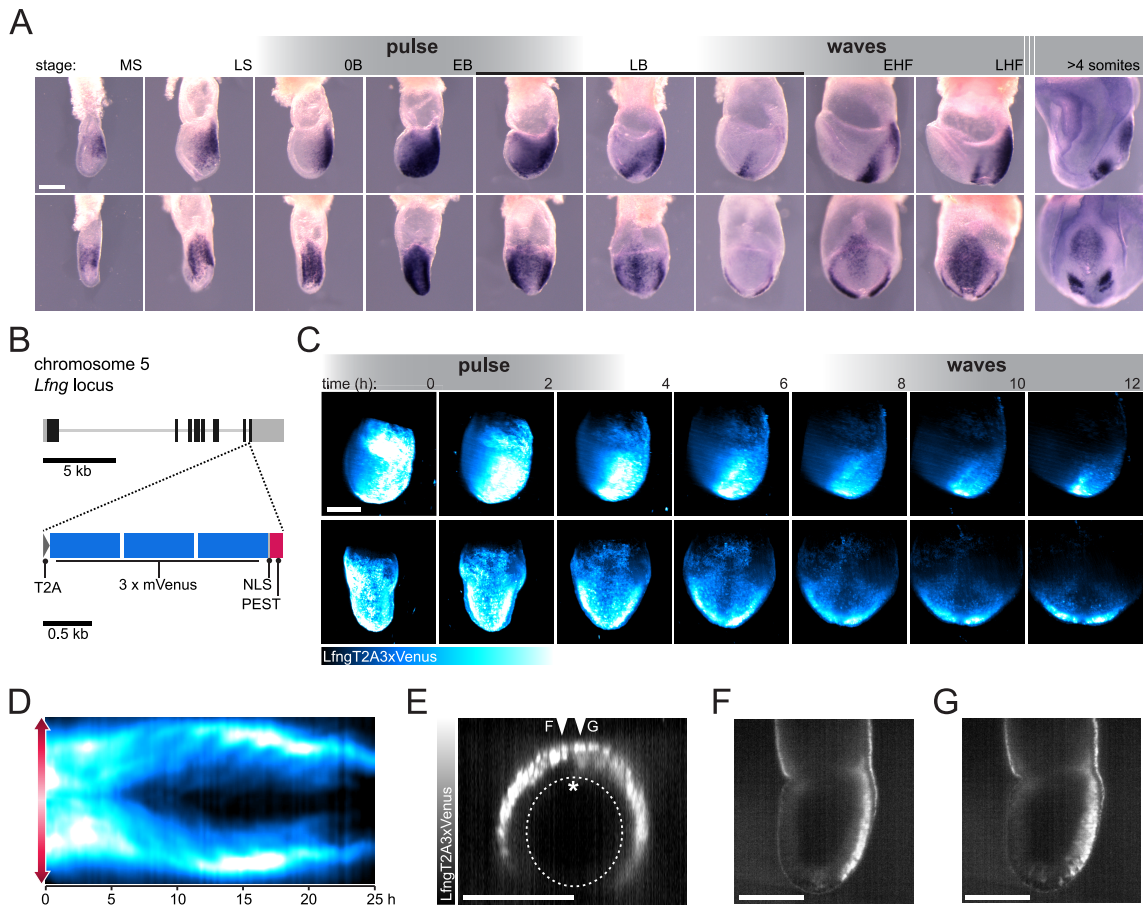


**Fig. 13: Validation of *Lfng* expression dynamics.** (A) Reconstructed time series of *Lfng* mRNA expression between E6.5 and E8.5. The same embryos are shown in a side view (top, anterior to the left) and from posterior (bottom). Number of samples collected for the different stages: MS: 9, LS: 6, OB: 8, EB: 10, LB(1): 16, LB(2): 6, LB(3): 28, EHF: 2, LHF: 2, somites: 8. (B) Schematic representation of the *LfngT2A3xVenus* construct knocked into the *Lfng* locus at the C-terminus (NLS, nuclear localization signal). (C) Still frames of a *LfngT2A3xVenus* embryo imaged from mid-gastrulation onwards. Maximum intensity projections in side view (top, anterior to the left) and from posterior (bottom) are shown. In the first two frames the mVenus signal is partially obscured by strong autofluorescence of the VE. (D) Kymograph along the direction of wave propagation as illustrated in Fig. 12E,F for the embryo shown in (C). (E) Transverse section through a LS embryo showing *Lfng* reporter fluorescence in mesoderm and PS (asterisk; amniotic cavity is outlined for orientation). (F,G) Sagittal sections of the same dataset as in (E) lateral to the PS (F) and at the PS (G) showing that *Lfng* reporter expression in epiblast is restricted to the PS. All scale bars: 200  $\mu\text{m}$ .

Thus, the dynamics observed with the live reporter LuVeLu are very likely to reflect endogenous *Lfng* expression dynamics. Together, I described the earliest dynamics of

the segmentation clock gene *Lfng* in a mammalian embryo model using a live imaging approach. I was able to capture the very first coherent wave and, preceding this wave, a pronounced peak of expression which was unknown to date.

## 1.2 First somites and early wave dynamics

Having identified the dynamic patterns of *Lfng* activity during gastrulation, I next analyzed the start of somite formation in relation to the first oscillations. In order to correlate the onset of oscillations with morphological segmentation, I traced the formation of gaps between the otherwise evenly distributed nuclei using nuclear marker R26-H2BmCherry in double-labeled LuVeLu;R26-H2BmCherry embryos as early sign for somite boundary establishment (Movie 7). I found that after the second oscillation the first cleft formed at the anterior boundary of the oscillatory domain. However, this initial boundary was not very pronounced and became undetectable within the first five oscillation cycles in the majority of analyzed embryos (7/10; Fig. 14A–D). Starting from the third oscillation, a persistent cleft formed with each oscillation cycle at the position where the wave halted in the distal paraxial mesoderm. I therefore categorized the dynamic patterns of LuVeLu activity in the gastrulating embryo into a pre-segment and a segment stage. The pre-segment stage includes the widespread pulse seen in PS and mesodermal wings and the first two oscillations that appear not to result in stable boundaries. The segment stage starts with the initiation of the third wave and definition of the first stable somite boundary (Fig. 14E).

Next, in collaboration with Gregor Mönke from our laboratory at EMBL Heidelberg, I asked if the very first oscillations share fundamental dynamic properties with those of later embryo stages. For segment stage embryos in mouse, fish and chick, travelling waves have been characterized as phase waves in the presence of a period gradient along the PSM, with fastest oscillations occurring in the posterior PSM (Introduction, 3.6; Giudicelli et al., 2007; Gomez et al., 2008; Oates and Ho, 2002; Palmeirim et al., 1997; Tsiairis and Aulehla, 2016).

In the gastrulating embryo we found the very first oscillations in the proximal paraxial mesoderm to occur with a periodicity of ~140 min while distally the oscillation period

was >20 min longer (Fig. 14F), indicating that the period gradient is a fundamental characteristic of segmentation clock oscillations, being present from the very beginning. A persistent period gradient, as we measured for the first four oscillations, is predicted to cause a gradual increase of phase difference between proximal and distal cells (Kopell and Howard, 1973). Indeed, we found that the magnitude of the phase gradient increased over time (Fig. 14G). An alternative way to quantify the wave buildup is the spatial wave number  $q$  (Kopell and Howard, 1973), which specifies how many waves travel along a certain spatial segment at a given time point (Introduction, 3.6; Fig. 7A; Fig. 14H). While the first wave almost appeared as a pulse with a very shallow phase gradient ( $8.4 \times 10^{-3} \text{ rad } \mu\text{m}^{-1}$ , median;  $1.7 \times 10^{-3} \text{ rad } \mu\text{m}^{-1}$ , IQR) and low wave number ( $q=0.37$ , median;  $0.23$ , IQR), both values increased over the next cycles in a gradual manner.

These findings indicate that a period gradient is already present as the very first observable waves sweeps along the proximodistal embryo axis. In contrast, the phase gradient gradually builds up over the first oscillatory cycles. To test, whether the period gradient that was measured is sufficient to drive the build-up of phase waves, Gregor Mönke calculated the expected wave number. We found that, indeed, the measured and the predicted evolution of  $q$  were in good agreement (Fig. 14H), demonstrating, that the period gradient of the pre-segment and early segment stage can fully account for the unfolding phase waves.

Together, these findings emphasize the critical importance of a period gradient for the evolution and maintenance of phase waves from the very first observable wave throughout embryo segmentation. Interestingly, the period gradient is already fully expanded at the time of the first wave, indicating that both, its polarity and amplitude are defined during early pre-segment stage, prior to the first wave. I therefore decided to analyze the dynamics of the pre-segment pulse, preceding the first wave, to ask whether the spatiotemporal characteristics of the first waves may originate during this stage.

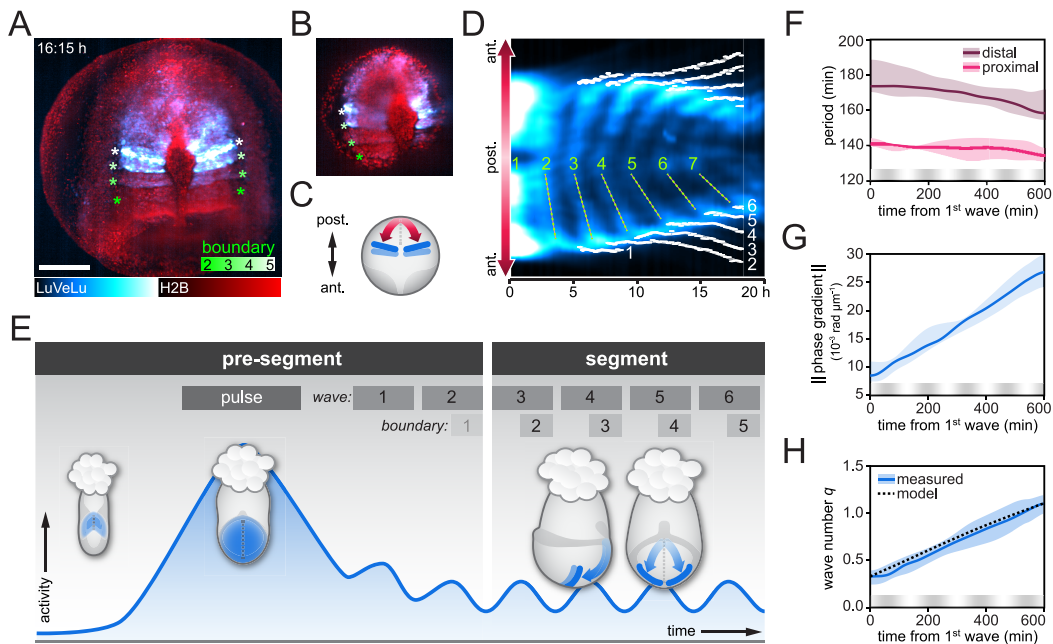


**Fig. 14: Characteristics of the first waves and somite boundaries.** (A) MIP of a representative LuVeLu;R26-H2BmCherry embryo imaged from distal pole (posterior top) to monitor segment boundary formation ( $n=10$  similarly imaged and analyzed embryos). Boundaries are visible as clefts between nuclei (color coded asterisks). Scale bar:  $200 \mu\text{m}$ . (B) Single plane of the dataset shown in (A) to better visualize the clefts between segments. (D) Kymograph of the embryo shown in (A,B) along the direction of wave propagation in the distally imaged embryo as depicted in (C; ant., anterior; post., posterior). The position of each segment boundary was manually traced through the time series. Traces are shown in white. Waves are numbered in green; dotted lines marking the waves were manually placed to guide the eye. The first segment boundary forms after the second wave reaches the distal domain. Note that in the embryo shown, as in the majority of analyzed samples (7/10), the first boundary disappears again while all later boundaries persist. (E) Schematic to summarize the start of the segmentation clock. Expression domains of *Lfng* (blue) during pre-segment and segment stages are depicted in embryos viewed from posterior (during pre-segment stage) or posterior and from the side (during segment stage). *Lfng* dynamics over time are shown as line profile. *Lfng* expression starts with the beginning of gastrulation and shows a marked expression peak (pulse) at EB stage before the first regular oscillations start. A first, transient segment boundary appears at the end of the second wave. Stable boundaries start to form with the third wave. The third wave marks the transition from pre-segment to the segment stage in which somitogenesis takes place. (F) Continuous measurement of oscillation periods in the proximal and distal LuVeLu domain over time, starting from the first wave. (G) Magnitude ( $\|\nabla\|$ ) of the phase gradient along the proximodistal embryo axis plotted over four oscillation cycles, starting from the first wave. (H) Measured and modeled evolution of the wave number  $q$  over time, starting from the first wave. For F–H, approximate oscillation peak positions are indicated as gray shadow above the time axes, solid lines represent median, corridors mark the IQR. The same  $n=9$  embryo kymographs were analyzed for F–H; graphs were prepared by G. Mönke.

### 1.3 Spatial and temporal pattern of the pre-segment pulse

The pre-segment pulse represents a so far unknown activity pattern during gastrulation, which I aimed to investigate in more detail. It constitutes an activity peak throughout the mesodermal expression domain of *Lfng*, but analysis showed that it is not spatially homogenous: The pulse displayed a marked proximodistal intensity gradient, peaking distally (Fig. 15A). Thus, the pulse pattern is polarized along the same axis as the period gradient of early waves.

The detailed analysis of the pulse further revealed that the pulse maximum was not reached at exactly the same time throughout the broad expression domain. I found that the pulse arrived at its maximum first in the proximal LuVeLu-positive domain and then spread distally (Fig. 15B). The time the pulse took to travel along the proximodistal embryo axis was measured to be 66 min (median; 38.25 min, IQR; Fig. 15C). Thus, the pre-segment pulse propagated as wave in proximodistal direction. It is therefore possible that the pulse primes the small phase shift that was observed for the first wave in the embryo (Fig. 14H; Fig. 15D), thereby explaining why the phase waves (with  $q>0$ ) do not start as pulses (with  $q=0$ ). However, the measurement of the proximodistal spreading of the pulse was hampered by the fast propagation of the pulse, its broad peak and the limited time resolution in the experiments. This resulted in a large spreading of data points (Fig. 15C) and therefore does not permit a quantitative comparison of the dynamics of the pulse and the first wave at this point.

To avoid confusion, I would like to point out that, while I have shown that the peak of the pre-segment pulse travels through the embryo essentially as a wave, it is fundamentally different from later waves in the embryo: The pulse is a singular activity peak and not part of an oscillation. Measurements, like phase and period, which assume recurring oscillations, are therefore not applicable to the pulse.

Since the pre-segment pulse occurs in parallel with the spreading of the mesoderm wings around the embryo, one possible explanation for the wave character of the pulse peak would be directed cell migration in the direction of wave propagation. To test this hypothesis, I monitored cell displacement during the pulse. To this end, I took ad-

vantage of the cell-to-cell variability of LuVeLu fluorescence which allowed me to follow traces of especially bright cells through the non-smoothed kymograph. As indicated in Fig. 15E, wave propagation and cell migration occurred on clearly distinct time scales with cell displacement being a much slower process. A significant contribution of cell migration to the temporal pulse propagation is therefore unlikely.

In summary, these results support the hypothesis that the pre-segment pulse, which occurs in a widespread domain in PS and mesodermal wings, might serve as pre-pattern for the waves. The pulse constitutes the first quantifiable synchronous clock gene expression event and displays a spatiotemporal polarity in form of an intensity gradient and a propagation direction along the same axis as the phase and period gradients of the very first waves.

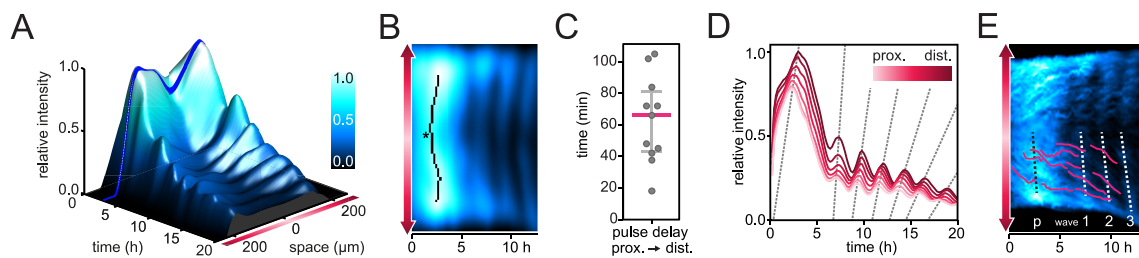


**Fig. 15: Temporal and spatial structure of the pulse.** (A) 3D surface plot of LuVeLu intensity profile along the direction of wave propagation (illustrated in Fig. 12E). The intensity profile at the time of the pulse peak is highlighted by a blue line. (B) Spatiotemporal profile of the pulse peak. In a kymograph of the dataset shown in (A) the maximum of the pulse along space (i.e. the pulse ridge) is shown as black line, the proximal domain is marked with an asterisk. (C) Scatter plot of the time delay at which the pulse peak reaches the distal (dist.) domain after it peaked in the proximal (prox.) domain ( $n=11$ ). Red bar represents the median, whiskers indicate quartiles. (D) Evolution of the oscillation phase shift from the pulse to the first waves. Several intensity profiles along time at different proximodistal positions are plotted to visualize the increasing peak delay (phase shift). Dotted lines extrapolate the delay between proximal and distal profiles for better visualization. (E) Comparison of wave propagation and cell displacement. Same kymograph as in (B) but without smoothing (Materials and methods, 5.2). Trajectories of single, bright LuVeLu-positive cells are visible (some are traced in red for illustration). Dotted lines demarcate the pulse (p) and first waves (1–3).



## 1.4 Disruption of Notch signaling in the context of initial synchronization

To test the hypothesis that the pre-segment pulse might serve as pre-patterning cue for segmentation waves, I challenged the system by disrupting Notch signaling at different levels of the pathway.

Is the pulse an early tick of the clock? To answer this question, I tested whether the negative feedback loop around auto-inhibitory *Hes7*, which is thought to be the core oscillating mechanism of Notch oscillations in the PSM (Introduction, 3.3), is already active at the time of the pulse. To this end, I took advantage of a *Hes7* knockout mouse line (Bessho et al., 2001) in combination with LuVeLu as readout, in order to image the pre-segment-to-segment stage transition on the optimized light-sheet setup.

The first half of the pre-segment stage, including the ascent to the pulse, was found to occur similarly between control and *Hes7* homozygous knockout embryos. The transition to waves, however, was clearly disrupted in mutant embryos: No oscillations were detected and overall intensity gradually decreased across the entire LuVeLu-positive domain (Fig. 16A,B; Movie 8).

With HES7 being a negative regulator of *Lfng* expression, an upregulation of *Lfng* has been described for *Hes7* knockout embryos during segmentation stages (Bessho et al., 2001; Bessho et al., 2003). Interestingly, no upregulation of LuVeLu fluorescence compared to the controls was visible during the pulse in *Hes7* mutants. In contrast to this and in accordance with earlier findings, LuVeLu fluorescence levels in *Hes7* mutant compared to wildtype samples were indeed significantly increased at E10.5, as experiments done by Katharina Sonnen from our laboratory demonstrated using *ex vivo* cultured tailbud explants (Fig. 16C). Thus, it seems that the pre-segment pulse initializes independent of HES7 regulation and that at the time of the pulse either HES7 is not yet expressed at high levels or *Lfng* expression is less responsive to HES7 repression than in later stages during somitogenesis.

To directly address the functional role of Notch signaling in the context of pre-segment pulse activation, I treated embryos with DAPT. If coordination of the pulse depended on

intercellular communication *via* Notch signaling, as it was shown for later stages of somitogenesis (Introduction, 3.5), a strong effect on the pulse would be expected. Embryos at MS to LS stage on E6.5 were cultured and imaged in 50  $\mu$ M DAPT throughout the pre-segment and early segment stages. Surprisingly, we found that also upon DAPT treatment, LuVeLu fluorescence showed a widespread, synchronized pulse in mesoderm and PS cells at EB stage, comparable to control embryos (Fig. 17A,B,D,E; Movie 9). Oscillations, however, were strongly repressed. Amplitude was markedly reduced, oscillations became undetectable after a few cycles and overall intensity gradually dropped to background level in all treated embryos (Fig. 17G,H). In a total of 15 samples, 3 embryos showed no oscillations, 5 embryos had 1–3, and 7 embryos had 4–6 detectable oscillations. Because of the low oscillation amplitude in all DAPT treated samples, quantitative measurements of wave properties were not possible. I further analyzed whether the proximodistal propagation of the pulse peak was impaired in DAPT-treated embryos. Despite the challenges of this measurement (Chapter II, 1.3), I indeed found a significant decrease in the proximodistal delay compared to controls (Fig. 17J), indicating that the DAPT treatment did have a limited effect on the pulse pattern.

To complement the pharmacological disruption of Notch dependent communication, I analyzed LuVeLu activity in an *Rbp-jk* knockout background (Han et al., 2002). Loss of RBP-J  $\kappa$  should result in a loss of all canonical Notch signaling downstream transcription, including *Hes7* and *Lfng* (Introduction, 3.3; Fig. 6). Surprisingly, in *Rbp-jk* knockouts, the pre-segment pulse was present, followed by clear oscillations, which gradually dampened and finally ceased after 4–8 cycles (Fig. 17C,F,I; Movie 9). To validate that expression of the LuVeLu reporter in an *Rbp-jk* knockout background was indeed also true for the endogenous *Lfng* gene, I compared *Lfng* mRNA expression in *Rbp-jk*<sup>-/-</sup> to *Rbp-jk*<sup>+/+</sup>, *Rbp-jk*<sup>+/-</sup> embryos collected between E6.5 and E8.5 (Fig. 17K,L). Both groups expressed detectable amounts of *Lfng* and showed a marked expression peak in EB stage. Expression in *Rbp-jk*<sup>-/-</sup> embryos faded away during segmentation stages, as it was seen in time-lapse experiments of *Rbp-jk*<sup>-/-</sup>;LuVeLu embryos.

Together, the presented results indicate qualitative differences between clock gene regulation during pre-segment pulse and subsequent waves. Early *Lfng* expression appears to be activated independently of the core Notch oscillator HES7 and in the absence of

both, Notch receptor cleavage and Notch transcriptional regulator RBP-J  $\kappa$ . Based on the combined evidence, I conclude that synchronization during the pre-segment pulse is regulated largely independently of Notch signaling. Thus, while being a *bona fide* Notch signaling activity readout during somitogenesis, *Lfng* does not recapitulate Notch signaling during pre-clock stage. I therefore differentiate in the following between results obtained with *Lfng* or LuVeLu during pre-segment and segment stages, assuming that only those for the segment stage apply to Notch signaling in general. Whether this is only true for *Lfng* or also other segmentation clock components classically thought to be under direct control of Notch remains to be clarified.

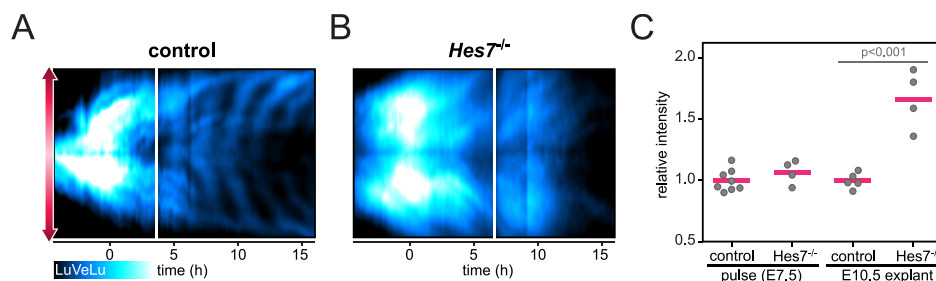


**Fig. 16: LuVeLu dynamics in *Hes7*-null background.** LuVeLu fluorescence intensity kymographs of representative control (A;  $n=8$ ) and *Hes7* knockout (B;  $n=4$ ) embryos from the same experiment along the direction of wave propagation as depicted in Fig. 12E are shown. Time point 0 is set to the peak of the pulse. During the time-lapse experiment  $O_2$  concentration in the culture medium was increased from 5 to 20%, causing a jump in reporter brightness, marked with a white line (Materials and methods, 3). Image brightness and contrast before and after the switch were adjusted independently, to visually compensate for the signal increase induced by the switch. (C) Relative change in LuVeLu reporter intensity in *Hes7* knockout compared to control embryos at an early (E7.5) and late (E10.5) stage. For E7.5, the maximum intensity of the pre-segment pulse was measured in mutant and control embryos and normalized to the average of control values (per experiment; three independent experiments). For E10.5 explants, the fluorescence intensity over several hours of imaging was averaged and compared between mutants and controls. Fluorescence was significantly higher in *Hes7*<sup>-/-</sup> compared to *Hes7*<sup>+/+</sup>, *Hes7*<sup>+/-</sup> embryos at E10.5 ( $p=0.009$ ). The E10.5 data was acquired by K. Sonnen. Normalization to the average intensity of control samples was done as described for the pulse stage (two independent experiments). Red bars represent mean.

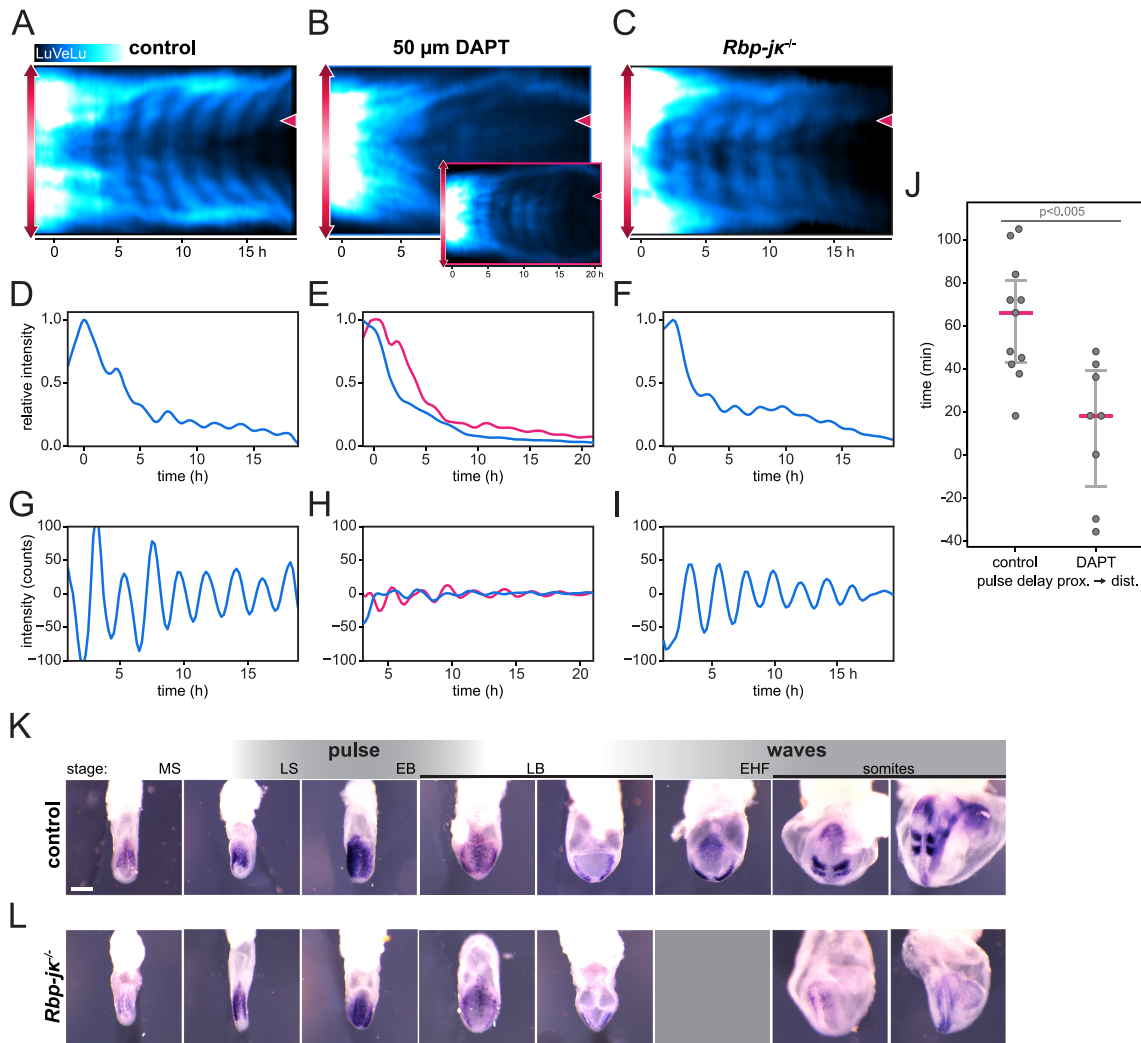


**Fig. 17: Disruption of Notch signaling during pre-segment and early segment stages.** Representative LuVeLu fluorescence intensity kymographs of control (A; n=11), two different embryos treated with 50 μM DAPT from MS–LS stage onwards (B; n=8), and an *Rbp-jκ* knockout mutant (C; n=4) are shown. Line profiles for kymographs were drawn along the direction of wave propagation as depicted in Fig. 12E. Time point 0 is set to the peak of the pulse for all panels in this figure. (D–F) Horizontal intensity profiles through the kymographs in (A–C) at the position indicated (red arrowhead), normalized to the pulse maximum separately for each panel. (G–I) Detrended signal of the intensity profiles shown in (D–F) in raw intensity counts (Materials and methods, 5.2). For DAPT-treated samples (B,E,H) two samples are shown to account for the varying number of residual oscillations. (J) Delay of the pulse peak between the proximal (prox.) and distal (dist.) LuVeLu domain in control and samples treated with 50 μM DAPT. The delay in DAPT treated samples is significantly reduced compared to the controls ( $p=0.0017$ ;  $n(\text{control})=11$ ;  $n(\text{DAPT})=8$ ). Control values are the same as shown in Fig. 15C. Red bars represent median, whiskers indicate quartiles. (K,L) *Lfng* expression in control and *Rbp-jκ* knockout embryos. Control *Rbp-jκ<sup>+/+</sup>*, *Rbp-jκ<sup>+/-</sup>* (K) and knockout *Rbp-jκ<sup>-/-</sup>* (L) embryos came from the same litters and were stained together. Number of control/*Rbp-jκ<sup>-/-</sup>* samples collected for the different stages: MS: 1/3, LS: 6/3, EB: 9/2, LB(1): 12/3, LB(2): 11/1, EHF: 16/0, somites(1): 6/6, somites(2): 8/1. Scale bar: 200 μm.

## 1.5 Activity of *Dusp4* and *Axin2* during pre-segment stage

With the new insight, that Notch signaling is not required for the pre-segment pulse, which alternative signals could be involved? Obvious candidates are FGF and Wnt signaling, the two main other pathways that have been implicated in the mouse segmentation clock. Both play an important role during gastrulation, their graded expression along the PSM is important for proper patterning (Introduction, 3.4) and FGF signaling has been proposed to be involved in the initiation of dynamic signaling in the PSM based on the correlation of expression timing and localization (Introduction, 3.8).

With the aim to review the role of FGF and Wnt signaling during pre-segment stage, I monitored the dynamics of downstream targets of both pathways together with *Lfng* to identify potential correlative patterns indicative of pathway interactions. To this end, I combined fluorescent gene activity reporters for FGF downstream target *Dusp4* and Wnt signaling component *Axin2* each with a reporter for *Lfng*. *Dusp4*T2A3xVenus and *Axin2*T2A3xVenus are knockin reporters in the endogenous loci, generated in our laboratory after a similar strategy as the *Lfng*T2A3xVenus line described above (Chapter II, 1.1). Since both reporters carry the mVenus fluorescent protein, a combination with LuVeLu for two-color imaging was not possible. Instead, I used *Lfng*T2A3xCherry, also generated in our laboratory, to combine with both mVenus lines.

It is important to note that although both *Dusp4* and *Axin2* are known to oscillate in the PSM (Aulehla et al., 2003; Niwa et al., 2007), I could not detect oscillations of the two fluorescent reporters during segment stage in the mouse gastrula. A possible reason may be that the large triple-Venus peptide, which is needed to generate a sufficiently bright readout, hampers its rapid degradation, thereby decreasing the oscillation amplitude to an undetectable level in the embryo (Introduction, 3.2). Nevertheless, the reporters can still convey valuable information on slightly less dynamic expression patterns such as the pre-segment pulse, with a duration of >5 h compared to waves with ~2 h period, and the establishment of signaling gradients. Fortunately, for the *Lfng*T2A3xCherry line, which also expresses a triple fluorophore, low amplitude oscillations were detectable on the light-sheet microscope, likely because the endogenous oscillation amplitude of *Lfng*

is higher than that of *Dusp4* and *Axin2*. Therefore, I was able to put the expression patterns of the FGF and Wnt signaling reporters into relation with pulse and waves of *Lfng*.

Results obtained from imaging both reporter combinations during pre-segment and early segment stage are presented in the following, starting with *Dusp4/Lfng* experiments, followed by those for *Axin2/Lfng*.

#### *Dusp4 pre-segment expression dynamics*

Expression of the *Dusp4* reporter in MS–LS stages was highest in a domain at the distal tip of the egg-cylinder and formed a distal-to-proximal gradient (Fig. 18A). From EB stage onwards the gradient started to invert, an observation I will discuss later in more detail (Chapter II, 1.6). Importantly, at the same time as the pre-segment pulse was observed for the *Lfng*T2A3xCherry reporter, also *Dusp4*TA23xVenus fluorescence peaked (Fig. 18A,B).

To compare the timing and expression domains of the pulse for the two reporters, I generated kymographs of transversal optical section as illustrated in Fig. 18C,D. In this way, fluorescence in mesoderm and epiblast was distinguishable. The analysis revealed that in contrast to mesoderm-restricted *Lfng*, *Dusp4* was expressed in epiblast and mesoderm (Fig. 18E). Using the *Lfng* reporter channel for segmentation, it was apparent that the *Dusp4* pulse occurred in mesoderm and epiblast, synchronously with *Lfng* (Fig. 18F). The proximodistal intensity gradient I described for LuVeLu (Fig. 15A) was qualitatively also reflected in the mesoderm and epiblast expression domain of *Dusp4* (Fig. 18G).

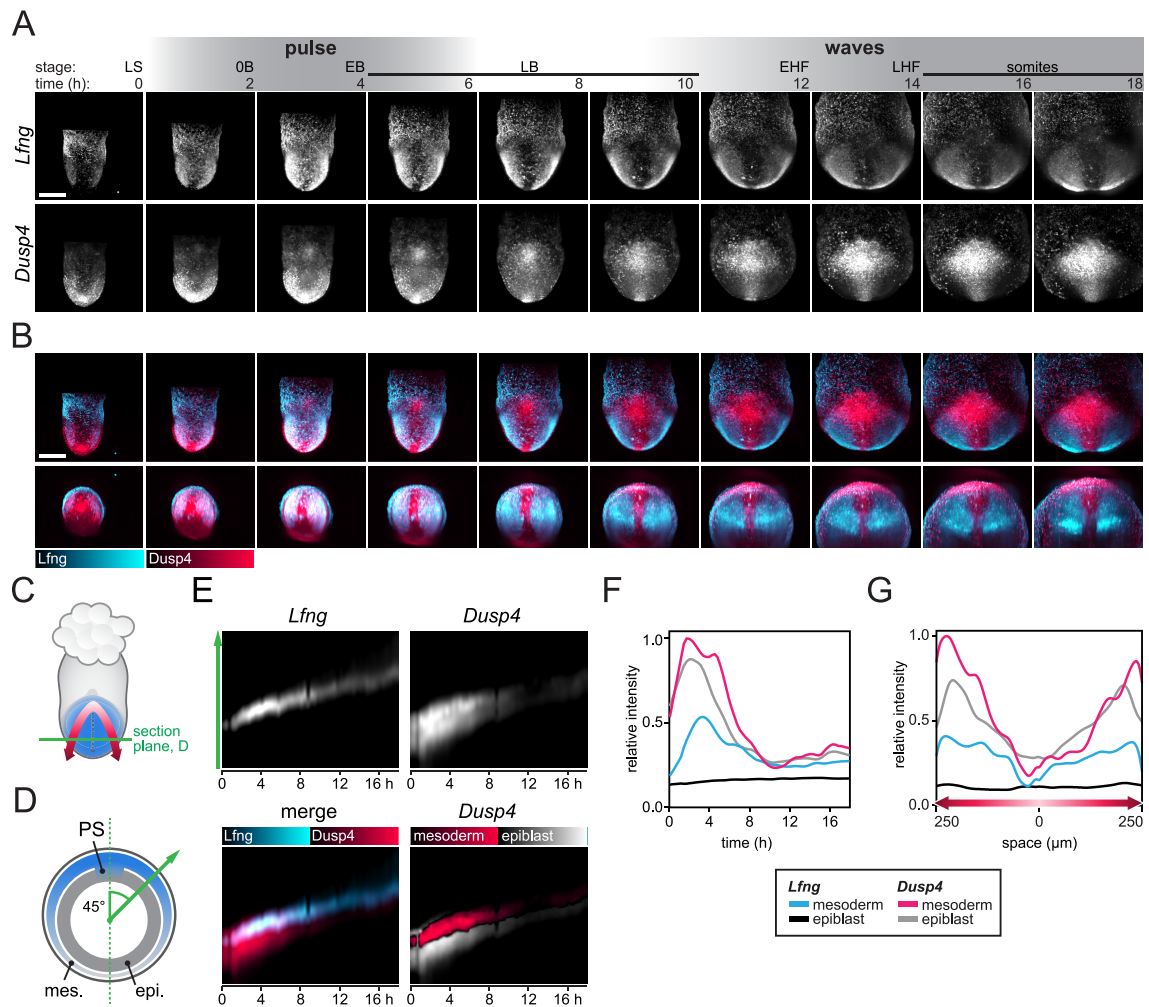


**Fig. 18: Comparison of *Dusp4* and *Lfng* expression dynamics during pre-segment and early segment stages.** (A,B) Still frames of a representative *Dusp4*T2A3xVenus;*Lfng*T2A3xCherry double reporter embryo imaged from LS stage to the onset of somitogenesis (n=8 similarly imaged embryos). In (A) MIPs from posterior direction are shown, the upper row of (B) shows the corresponding merge of both fluorescence channels and the lower row depicts the same dataset from the distal end (posterior up). (C) Cartoon of a mouse gastrula illustrating the position of the transversal optical section (green) depicted in (D) at 70% of the proximodistal extend of the *Lfng* domain. (D) Section kymographs in (E) were generated from line profiles from the center of the embryo section outwards at a 45° angle with respect to the anteroposterior axis (dotted line; PS, primitive streak; mes., mesoderm; epi., epiblast). (E) Section kymographs of total *Lfng* and *Dusp4* reporter fluorescence (upper row) and the merge of both channels (lower left). In the lower right panel, the *Lfng* channel was used to segment mesoderm (red) from other (=epiblast; gray) domains of *Dusp4* expression. (F) Maximum fluorescence intensity along the time dimension of kymographs shown in (E). (G) Fluorescence intensity along the proximodistal direction of later *Lfng* wave propagation as depicted in (C) by the red spline. All graphs are background-subtracted and fluorescence intensity is normalized to the global maximum of the plot. All scale bars: 200  $\mu\text{m}$ .

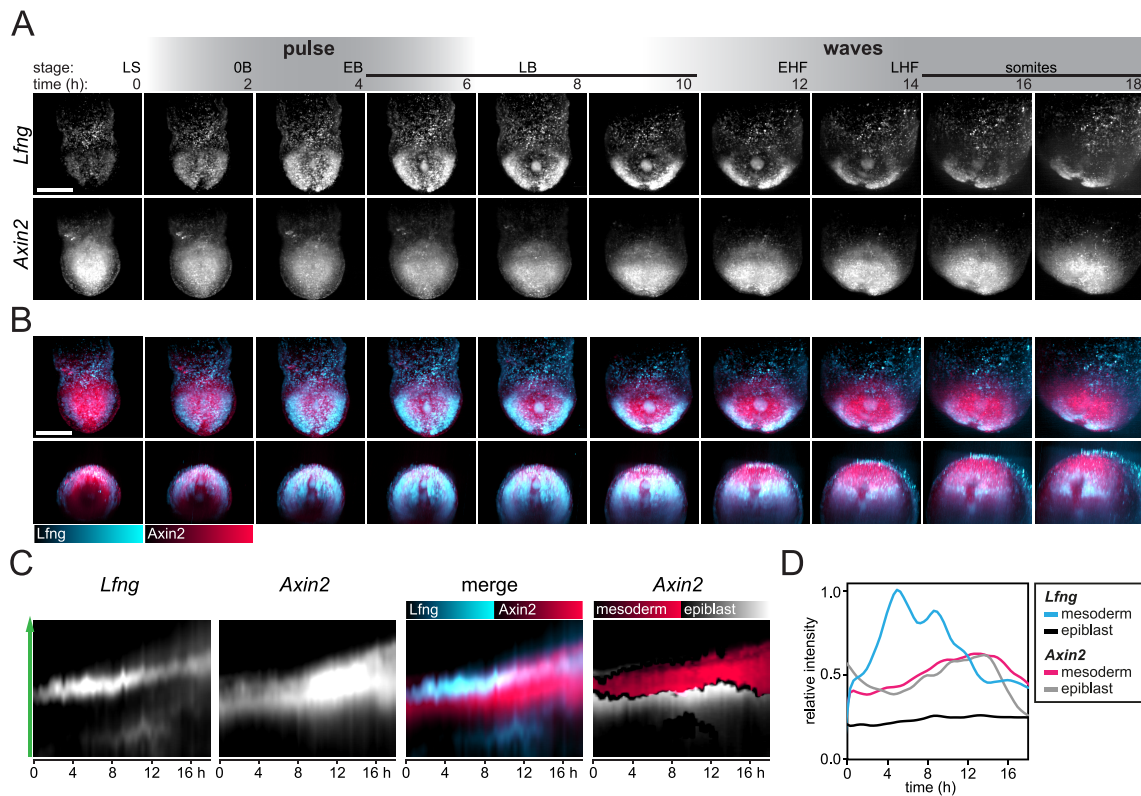


**Fig. 19: Comparison of *Axin2* and *Lfng* expression dynamics during pre-segment and early segment stages.** (A,B) Still frames of a representative *Axin2*T2A3xVenus;*Lfng*T2A3xCherry double positive embryo imaged from LS stage to the onset of somitogenesis (n=5 similarly imaged embryos). In (A) MIPs from posterior direction are shown, the upper row of (B) shows the corresponding merge of both fluorescence channels and the lower row depicts the same dataset from the distal end. (C) Section kymographs generated in the same way as in Fig. 18C–E. Right-most panel shows mesoderm segmentation of *Axin2* signal on the basis of the *Lfng* channel. (D) Maximum fluorescence intensity along the time dimension of kymographs shown in (C), background-subtracted and fluorescence intensity is normalized to the global maximum of all graphs. All scale bars: 200  $\mu$ m.

### *Axin2* pre-segment expression dynamics

Imaging of *Axin2*T2A3xVenus revealed that *Axin2* reporter fluorescence was homogeneously expressed in the posterior embryo with no pronounced proximodistal polarity during pre-segment and early segment stages (Fig. 19A,B). Expression levels gradually increased during the experiment but no pulse-like dynamics were observed around the time of the *Lfng* pre-segment pulse in double labeled embryos. Similar to *Dusp4*, *Axin2* reporter activity was found in mesoderm and epiblast to approximately the same levels (Fig. 19C,D).



Taken together, double imaging of *Lfng* and *Dusp4* gene activity revealed strong spatio-temporal correlation between both genes during pre-segment stage. This indicates that the pulse is a phenomenon which is not limited to *Lfng* and importantly, is not exclusive to mesoderm and PS, based on the observation of *Dusp4* dynamics in the epiblast. In contrast, no indication of a direct correlation between *Axin2* and *Lfng* pre-segment pulse activity patterns was found.

## 1.6 Gradients and waves—what comes first?

Having compared the expression dynamics of *Lfng* and *Dusp4* during the time of the pre-segment pulse, I further used the *Dusp4*T2A3xVenus;*Lfng*T2A3xCherry double reporter data to examine the interplay between signaling oscillations and gradients during the phase of segmentation clock establishment.

FGF8 has been shown to influence the position of oscillation arrest in the PSM (Introduction, 3.4) and is implicated in the control of the posterior-to-anterior period gradient (Introduction, 3.6). Thus, examining the temporal order of events during pre-segment and early segment stage using *Lfng* as readout for oscillations and *Dusp4* as a proxy for the FGF signaling gradient may give valuable insight into the interaction of the two systems.

Imaging of the *Dusp4*T2A3xVenus reporter showed that the *Dusp4* gradient inverts its orientation during gastrulation. In early gastrulation, the gradient ran from distal high to proximal low. Then starting from EB stage, a domain at the root of the allantois at the proximal limit of the embryo proper increased in size and intensity, while intensity in the distal domain dropped. Distal fluorescence did not decrease uniformly but remained stronger along the midline compared to paraxial tissue (Fig. 18A,B).

Analysis of *Dusp4*T2A3xVenus;*Lfng*T2A3xCherry embryos revealed that the *Lfng* pulse occurred when the distal-to-proximal gradient of *Dusp4* peaked, whereas the first two *Lfng* waves happened already during the buildup of the proximal-to-distal gradient, after gradient inversion (Fig. 20). Thus, *Lfng* waves follow the direction of the gradient from high to low as it is known from later segment stage embryos at E9.5–10.5 (Aulehla

and Pourquié, 2010). Conversely, the pre-segment pulse traverses the tissue distally while the *Dusp4* gradient still points the other way. These experiments show that both, the FGF signaling gradient as well as the dynamic patterns of the later Notch signaling target *Lfng*, drastically change from early to late pre-segment stage. Hence, the *Dusp4/Lfng* double imaging experiments did not reveal a clear hierarchy between the initiation of oscillations and gradients but demonstrated that both processes developed in parallel, possibly in a coordinated manner.

In summary, the pre-segment stage I describe in this work is a critical phase during set-up of the segmentation clock in which not only period and phase gradients of later Notch target *Lfng* originate but also the FGF signaling gradient is set up.

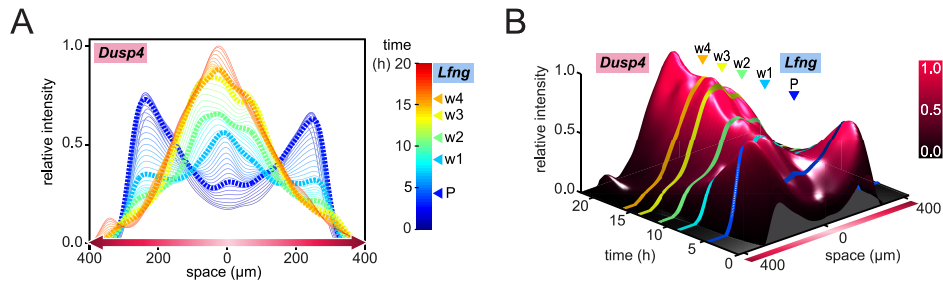


**Fig. 20: *Dusp4* gradient build-up during pre-segment and segment stages.** (A) Intensity profiles of *Dusp4*T2A3xVenus along the proximodistal direction of wave propagation as depicted in Fig. 12E in a representative *Dusp4*T2A3xVenus;*Lfng*T2A3xCherry embryo (n=3 similarly analyzed embryos). Time is color-coded and the occurrence of the pulse (P), and the first four waves (w1–4) measured in the *Lfng* reporter channel are marked in the time-color bar and in the plot by bold, dashed lines. (B) Alternative representation of the data shown in (A) as 3D surface plot. *Lfng* reporter dynamics are highlighted similar to (B) on the *Dusp4* reporter intensity surface.

## 2. Discussion

In Chapter II, I report real-time long-term imaging of segmentation clock gene *Lfng* in post-implantation embryos which led to the discovery of a pronounced, synchronous expression pattern of *Lfng* at mid-gastrulation—the pre-segment pulse. The pulse, which covers PS and mesoderm wings at EB stage, was identified to be largely independent of Notch signaling and was also found in the dynamics of FGF signaling target *Dusp4* but not the Wnt signaling component *Axin2* (Fig. 21). Coherent oscillations commenced directly following the pre-segment pulse, suggesting that the pulse may play a role in the initiation of synchrony among oscillatory presomitic cells. Quantification of early oscillation dynamics following the pulse identified a persistent period gradient to underlie the gradual establishment of phase waves. This demonstrates the existence of an early directional polarity at the onset of the segmentation clock.

### 2.1 Comparison of early Notch signaling patterns in mouse, fish and chick

While results on signaling dynamics in early post-implantation mouse embryos are presented in this study, the initiation of the segmentation clock in zebrafish and chick has been described before (Introduction, 3.8; Jouve et al., 2002; Riedel-Kruse et al., 2007). Despite the very different geometry of the gastrula in these three vertebrate model systems (Solnica-Krezel and Sepich, 2012), some features of early clock gene activity seem to be conserved. First, expression of *bona fide* Notch target genes in presomitic tissue starts early during gastrulation in a domain including the blastopore (the PS in mouse and chick and the blastoderm margin in fish) as well as nascent mesoderm. Second, coherent dynamic patterns precede the first segmentation wave in all three species. Here I described one pulse of expression in PS and mesoderm wings followed by two waves that do not yet lead to stable somite boundaries in mouse embryos (Fig. 12; Fig. 21). Similarly, in zebrafish a pulse followed by four waves were found prior to the

first segmentation wave (Riedel-Kruse et al., 2007). Such pulse-to-wave transition was not described in chick, however. There, two waves precede the first segment-forming wave (Jouve et al., 2002). Third, the first pulses or waves in all three species seem to appear suddenly, with high amplitude, indicating a rapid establishment of synchrony, possibly by a similar mechanism.

Together, this comparison demonstrates that highly dynamic and synchronized clock gene expression patterns preceding somitogenesis are a common feature among diverse vertebrate species. Whether these patterns are the result of a similar underlying synchronization strategy remains to be clarified.

## 2.2 Spatiotemporal patterns preceding segmentation

The directionality of waves in the embryo during somitogenesis is linked to an oscillation period gradient as it was found in mouse, chick and fish (Giudicelli et al., 2007; Gomez et al., 2008; Palmeirim et al., 1997; Tsiairis and Aulehla, 2016). Interestingly, real-time quantifications of signaling dynamics in the mouse gastrula performed together with Gregor Mönke revealed that the very first wave sweeping through the paraxial mesoderm already exhibits a period gradient. This period gradient, which remains relatively stable over the first oscillation cycles we analyzed, can fully account for the buildup of waves as demonstrated by the gradual increase of the phase gradient magnitude and the wave number (Fig. 14F–H). Thus, we identified the period gradient as the fundamental pattern underlying segmentation clock waves from the very beginning of synchronized oscillations onwards.

Of note, the values we measured for the period gradient in the gastrula are quite similar to those measured in E10.5 embryos (Tsiairis and Aulehla, 2016), although earlier studies predicted a faster initial segmentation rate (Tam, 1981). However, the direct comparison of embryos after two days of culture on the microscope to *in utero* developed embryos revealed no obvious developmental delay (Fig. 9F). Thus, I am confident that the dynamics I observed in the mouse gastrula closely reflect the *in utero* situation.

The observation that the period gradient is already fully extended at the time of the first wave demonstrates that a proximodistal polarity is established very early during the buildup of the segmentation clock, prior to the initiation of rhythmic oscillations. This raises the question, what underlies the early polarity.

Signaling gradients along the proximodistal embryo axis are one possible mechanism to organize cellular oscillation periods. For instance, FGF signaling seems to have an influence on the oscillation period, as preliminary data from our laboratory obtained in tissue from E10.5 embryos suggest (Introduction, 3.6). According to these experiments, high FGF signaling activity would maintain a low oscillation period while periods increase with decreasing input from the FGF pathway. Using *Dusp4/Lfng* double reporter imaging I could show, that the *Dusp4* gradient, as readout for FGF signaling activity, changes drastically during pre-segment stage, inverting its polarity from distal-high first to proximal-high later on. The start of waves correlates with the gradual transition to a proximal-high *Dusp4* gradient, while the pulse occurs during the distal-high phase of the gradient (Fig. 20). Thus, if FGF signaling activity was in control of the *Lfng* oscillation phase gradient, a gradual buildup would be more plausible than the stable phase gradient we measured.

An alternative possibility is that the pre-segment pulse has a function as pre-pattern for the waves, laying down the period gradient and maybe also initializing the slight proximodistal phase delay measured for the first wave (Fig. 14G). The detailed quantification of the pre-segment pulse revealed that a proximodistal polarity is already measurable during this early stage. LuVeLu reporter activity was found to be graded from proximal high to distal low and the pre-segment pulse traverses the tissue in proximodistal direction, like the following phase waves (Fig. 15).

To test the hypothesis that the pulse pre-patterns the waves, one would have to manipulate the spatiotemporal polarity of the pulse. Interestingly, I observed a reduction of the wave-like propagation of the pulse in DAPT treated embryos (Fig. 17J). Since the following waves were strongly inhibited in these embryos, I could not directly study the impact of altered pulse dynamics on the waves. However, in future experiments, short-duration DAPT treatment of embryos only before or during the pre-segment pulse may allow to manipulate the pulse while preserving oscillatory dynamics.

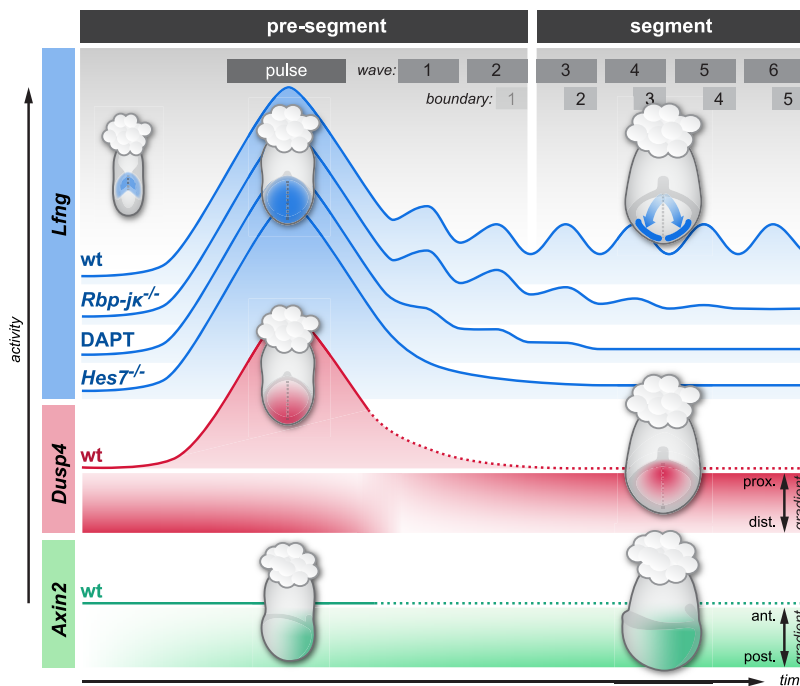


**Fig. 21: Summarizing the start of the segmentation clock.** Expression domains of *Lfng* (blue), *Dusp4* (red) and *Axin2* (green) in wildtype (wt) embryos during pre-segment and segment stages are depicted in embryos viewed from posterior (for *Lfng* and *Dusp4*) or from the side (for *Axin2*). Gene activity dynamics over time are shown as line profiles for *Lfng* in wildtype and three Notch signaling related perturbations and for *Dusp4* and *Axin2* in wildtype embryos. For *Dusp4* and *Axin2* the establishment of signaling gradients along the proximodistal and anteroposterior axes, respectively, are also shown (prox., proximal; dist., distal; ant., anterior; post., posterior). The pre-segment stage of *Lfng* expression is characterized by the synchronous expression pulse in PS and mesoderm wings, followed by two proximodistal waves which do not lead to stable somite boundaries. The third wave marks the start of the segment stage in which each wave is followed by the specification of a boundary. All Notch signaling related perturbations tested did not abolish the pre-segment pulse but affected oscillations to a varying degree. *Rbp-jk*<sup>-/-</sup> mutants showed up to 8 dampening oscillations, DAPT treated embryos showed 0-6 strongly dampened oscillations and in *Hes7*<sup>-/-</sup> mutants no oscillations were detected. The pre-segment pulse was also found for FGF signaling target *Dusp4* but not Wnt target *Axin2*, yet the reporters for both genes did not allow oscillation quantification (indicated by dotted intensity profiles). Overall *Dusp4* expression was observed to be graded proximodistally, inverting the gradient polarity between the pulse and the first *Lfng* wave. *Axin2* was found to be graded along the anterior-posterior embryo axis throughout gastrulation and early somitogenesis.

### 2.3 *Lfng* activation during the pre-segment pulse

I found that the pre-segment pulse of *Lfng* was not abolished by inhibition of the Notch signaling pathway in DAPT treated embryos or null mutants for the transcription factor RBP-J  $\kappa$  (Fig. 17). These experiments strongly indicate that *Lfng* expression during the pre-segment pulse, which represents the first synchronous expression pattern I could observe, is activated independently of Notch signaling. Thus, *Lfng*, an established, direct target of Notch signaling (Cole et al., 2002; Morales et al., 2002), which is commonly used as *bona fide* readout of Notch signaling dynamics in the context of PSM segmentation (Aulehla et al., 2008; Dequéant et al., 2006; Feller et al., 2008; Hubaud et al., 2017), does not act as Notch target at the very beginning of clock gene dynamics. Similar findings were made in zebrafish where the established Notch target *dlc* (Holley et al., 2002; Oates and Ho, 2002) was shown to be expressed in the presence of DAPT and undergo the very first oscillation cycles similar to untreated embryos (Riedel-Kruse et al., 2007). These results are in line with the perspective derived from experiments in fish that Notch signaling maintains synchrony of oscillators but does not create initial synchrony (Introduction, 3.8).

Based on the analysis of segmentation pattern defects in Notch signaling mutants, it has been suggested that, similar to fish, Notch signaling is also dispensable for initial synchronization in mouse (Conlon et al., 1995; Huppert et al., 2005; Lewis et al., 2009). However, since Notch signaling in mouse has been proposed to have a function also in the creation of sharp boundaries (Koizumi et al., 2001; Morimoto et al., 2005; Takahashi et al., 2000) and/or the definition of an anterior-posterior somite polarity (Feller et al., 2008), conclusions on the state of cellular synchrony drawn from observations of the downstream segmentation pattern need to be evaluated carefully. The here presented work now provides direct evidence in mouse for Notch signaling independent initial synchronization of the segmentation clock. Importantly, this conclusion is based on the direct visualization of signaling activity at the onset of synchronized oscillations in the presence of Notch signaling inhibition.

If not Notch, which other signals may act on *Lfng* in mouse or *dlc* in fish during early pre-segment stage? One potential candidate in this context is FGF signaling. In support

of an interaction between *Lfng* and FGF signaling, I was able to show that activity of FGF signaling target *Dusp4* peaked concomitantly with the *Lfng* pre-segment pulse (Fig. 18). On a molecular level it remains unclear how such interactions between FGF signaling and *Lfng* and possibly other *bona fide* Notch targets is realized. It has been shown in mouse that FGF and Notch signaling oscillations are linked by HES7 (Introduction, 3.3; Hayashi et al., 2009; Niwa et al., 2007). However, I found that the pre-segment pulse of *Lfng* occurred even in a *Hes7* knockout background, arguing against a link between FGF signaling and Notch targets mediated by HES7 during this stage. Further studies examining the early pre-segment stage under pharmacological and genetic manipulations of the FGF signaling pathway will need to elucidate the putative interaction between FGF signaling and *bona fide* Notch signaling targets.

Wnt signaling is another pathway that may be involved in the activation of the *Lfng* pre-segment pulse. Wnt signaling has been shown to regulate Notch ligand *Dll1* through transcriptional activation mediated by LEF1 (lymphoid enhancer-binding factor 1; Galceran et al., 2004). Also in the *Lfng* promoter sequence which is included in the LuVeLu transgene I found predicted LEF/TCF (T-cell factor) binding sites, indicating that a similar interaction may be present (based on computational transcription factor binding site matching, using MatInspector; Cartharius et al., 2005; Quandt et al., 1995). However, a pulse similar to the one described for *Lfng* and *Dusp4* was not observed using a reporter for *Axin2* as Wnt signaling readout. Preliminary data I obtained by imaging LuVeLu activity in embryos expressing the stable  $\beta$ -catenin allele  $\beta$ -catenin<sup>del(ex3)</sup>, did not indicate an overt effect of Wnt signaling over-activation on *Lfng* pre-segment and early segment stage dynamics. Therefore, experimental evidence of an involvement of Wnt signaling in *Lfng* pre-segment activation is lacking to date.

The fact that the LuVeLu reporter, which contains a 2.3 kb sequence of the *Lfng* promoter, shows the same activity patterns during pre-segment stage as the full-length *Lfng* gene narrows down the possible genomic interaction sites that may be involved in pre-segment pulse transcription. Systematic shortening of the LuVeLu promoter to identify the transcriptionally active region may therefore be an alternative strategy to examine the early Notch independent activation signal.



Summarizing, a central question for the continuation of this project remains, upon which signals the pre-segment pulse emerges and how it can be manipulated. I presented good evidence that Notch signaling is not the driving force. Understanding and controlling the pulse initiation is key to dissecting the putative role of the pulse in the context of pre-patterning of segmentation waves and could help to identify the nature of the initial synchronization signal.

## 2.4 Early oscillations in the absence of RBP-J $\kappa$

The surprising discovery of *Lfng* activity and dynamics in an *Rbp-jk*-null background throughout pre-segment and early segment stage challenges not only the role of intercellular Notch communication at the time of the pulse, but also during the onset of the first oscillations and waves.

According to the prevailing model, RBP-J  $\kappa$  is required for activation of canonical Notch signaling targets. RBP-J  $\kappa$  is a transcriptional repressor that activates expression of downstream target genes upon binding of NICD (Kopan and Ilagan, 2009; Pursglove and Mackay, 2005). In line with this model, expression of *Lfng* was found to be completely absent in E8.5-9.5 mouse embryos (Ferjentsik et al., 2009; Niwa et al., 2007) although another study reported a few cases of faint *Lfng* stripes in anterior PSM (Del Barco Barrantes et al., 1999). The present work is the first to look at *Lfng* in *Rbp-jk* mutants earlier than E8.5, revealing that *Lfng* activity disappears just before the stages that have been described by others (Fig. 17K,L).

The same studies claiming the absence of *Lfng* at E8.5 in *Rbp-jk* mutants report strongly reduced yet still dynamic expression of *Hes7* in the posterior PSM (Ferjentsik et al., 2009; Niwa et al., 2007). Like *Lfng*, *Hes7* is thought to be activated through NICD/RBP-J  $\kappa$ . The persistent dynamics of *Hes7* and, as we now know, also *Lfng* in the *Rbp-jk* knockout may be explained by three alternative scenarios: First, the genes could be activated independently of Notch signaling, by a so far unknown factor “X”. Second, some RBP-J  $\kappa$ -independent NICD activity may remain, as it was suggested for *Drosophila* (Hori et al., 2004). Third, maternal expression of *Rbp-jk* in the zygote may provide the transcription factor independent of the *Rbp-jk* genotype of the embryo. Differ-

ent activation thresholds of the two genes might explain why *Hes7* expression is maintained longer than that of *Lfng* (Ferjentsik et al., 2009).

The third hypothesis has been tested by Souilhol and colleagues. They found that the phenotype of *Rbp-jκ*<sup>-/-</sup> embryos was independent of the maternal expression status of *Rbp-jκ* in the zygote, arguing against a role of maternal contribution (Souilhol et al., 2006). This leaves two alternative explanations: Either NICD activates expression independent of RBP-J κ (“NICD model”) or a Notch signaling independent factor drives expression (“factor X model”; Fig. 22).

In this context it is interesting to note that oscillations were more affected in DAPT-treated than *Rbp-jκ* mutant embryos (Fig. 17). In principle, this could be explained by both remaining models. According to the NICD model, DAPT prevents Notch cleavage, i.e. the formation of NICD. Without NICD, RBP-J κ represses *Hes7* and *Lfng* expression. Within the framework of the factor X model, we would have to assume that transcriptional repression by RBP-J κ is stronger than the inductive effect of X, resulting effectively in the repression of *Hes7* and *Lfng*.

Treatment of *Rbp-jκ*<sup>-/-</sup> embryos with DAPT may help to discriminate between both models. Under such conditions, within the NICD model I would predict that *Lfng* oscillations were as strongly disrupted as in the DAPT-alone treatment because the bottleneck is NICD production. In the factor X model, however, the removal of transcriptional repressor RBP-J κ may allow X to exert its transcriptional activation effect. Consequently, similar to the *Rbp-jκ* null condition, oscillations should start normally and slowly desynchronize because the synchronization loop *via* NICD was disrupted (Fig. 22). Experimental testing of these hypotheses has not been done yet but the customized culture and mounting setup for embryo imaging is a suitable platform to conduct such a study.

## 2.5 The onset of synchrony

The previous sections discussed the involvement of certain molecular components in the activation of *Lfng* during EB stage, which is of importance for the design of pulse per-

turbation experiments. The more general question remains, however, how synchronous cellular activity is achieved—independent of specific signaling cascades.

One possibility is that synchronous expression of clock genes is downstream of yet another, earlier event during development that synchronizes the cells. Such a trigger event may for instance be the transition from an epidermal to a mesenchymal cell fate during gastrulation. We could show that *Lfng* expression initiates in the PS, thus timing of ingressión may start the clock in individual nascent mesoderm cells, thereby causing the pulse with a certain, fixed time delay. However, the pre-segment pulse and the formation of mesoderm occur on quite distinct time scales: While mesoderm cells take about one day, from ES to EB stage, to fully cover the egg cylinder (Kinder et al., 2001), my real-time quantifications revealed that the pre-segment pulse covers the widespread mesoderm domain in less than 5 h, arguing against synchronization by ingressión timing.

It is interesting to note in this context that the *Dusp4* pulse occurring in parallel with the *Lfng* pulse included not only mesoderm but also epiblast tissue (Fig. 18). Consequently, obtaining a mesodermal identity seems not to be a prerequisite for cells to join in the synchronous expression peak. Thus, signaling events from epiblast to mesoderm or *vice versa* may be involved in the induction of the pulse, shifting the focus away from a mesoderm-centric view.

Alternatively, synchrony may be the result of a gradual, self-organizing process in which individually oscillating cells adapt their own rhythm to the rhythm of their neighbors. Such gradual synchronization has been demonstrated for mixed PSM cells of E10.5 embryos *in vitro* (Tsiairis and Aulehla, 2016). In these experiments, cells were shown to reach in-phase synchrony 5-6 h after randomization, measured by the increasing collective frequency in the cell aggregates. We did not observe such synchronization transients in the gastrula which may be due to a low collective frequency. In future experiments, single cell oscillation tracking throughout the pre-segment phase could reveal if non-synchronous oscillations precede the first waves. The mosaic labeling strategy presented in Chapter I, section 1.3, for long-term cell tracking in the post-implantation mouse embryo provides the means for such a study. However, synchronization *in vitro* was effectively prevented by DAPT treatment (Tsiairis and Aulehla,

2016), arguing for two different mechanisms of synchronization between the gastrula and the randomized cell aggregates from later stage embryos.

Recently, Hubaud and colleagues proposed a quorum sensing mechanism for triggering oscillations in PSM cells (Hubaud et al., 2017). In their model, cell density, communicated *via* YAP signaling, pushes non-oscillatory PSM cells over an activation threshold to initialize oscillations. It is likely that the drastic morphological changes during gastrulation influence cell density or other mechanical properties like tension and deformation which could in turn serve as trigger to activate oscillations. Such a model, in which the segmentation clock is initialized once the mesoderm has reached a certain physical state, is conceptually very appealing. It would allow a direct coupling between the constitution of mesodermal tissue and the initiation of mesoderm patterning.

In contrast to the established model of kinematic PSM waves which result from an oscillation phase shift but do not immediately rely on cellular interactions, Hubaud and colleagues see in their experimental system indications for trigger waves-like behavior: *In vitro* cultured PSM cells directly relapse to high-amplitude, synchronized oscillations after DAPT washout, lacking slow synchronization transients. As discussed earlier, we also did not observe gradual synchronization in the mouse gastrula either but rather an abrupt appearance of a synchronized pulse, followed by waves. An unambiguous way to discern trigger waves and kinematic waves is to disrupt communication between elements. While kinematic waves continue irrespectively of physical separation, trigger waves are predicted to stop at the boundary because they require direct relay of activity. Jouve and coworkers showed that the early chevron-like waves that traverse the pre-segment chick embryo are not hindered by cutting of the tissue, arguing for a kinematic wave nature (Jouve et al., 2002). However, it remains to be verified how comparable the dynamic pre-segment expression patterns between species are on a mechanistic level. Combining live imaging with precise optical manipulation techniques like laser microsurgery or optogenetics may enable similar experiments in *ex vivo* cultured gastrula cells as well as the intact post-implantation mouse embryo in the near future.

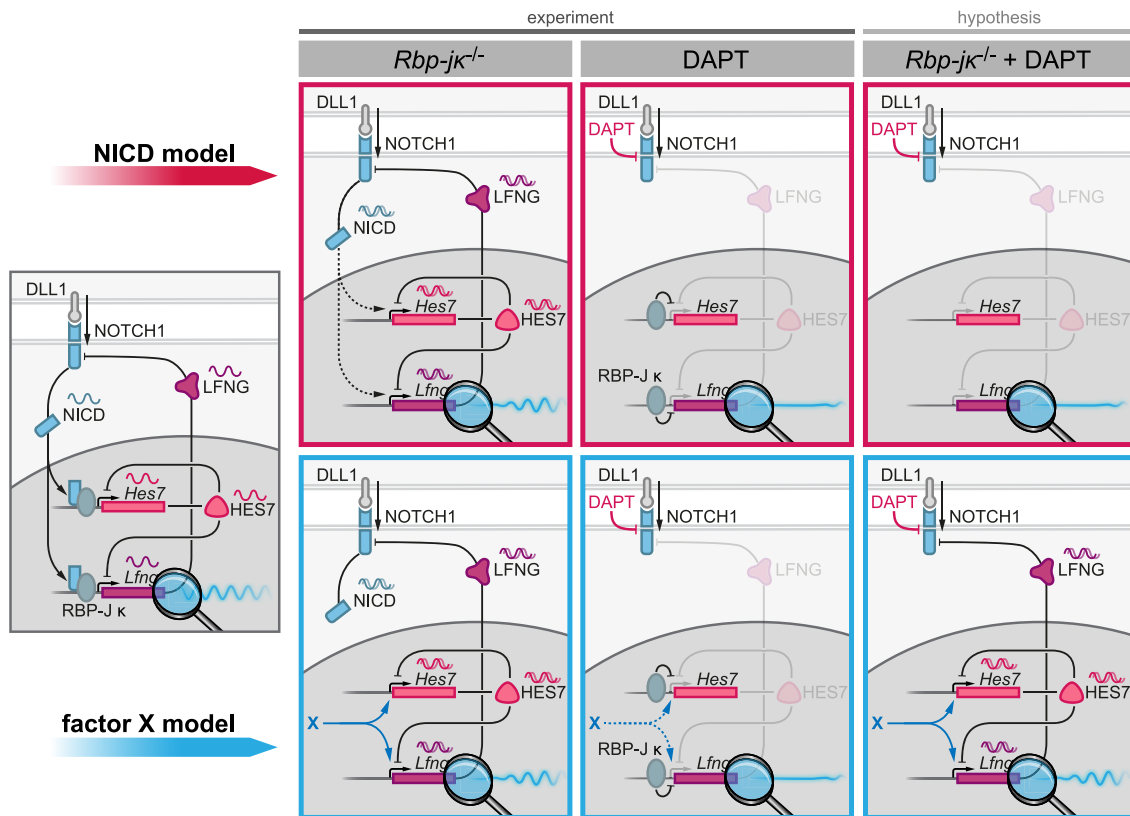


**Fig. 22: Alternative models explaining early *Lfng* activity in the context of disrupted Notch signaling.** On the left, the intracellular oscillatory feedback loops of the Notch oscillator as explained in Fig. 6 are shown. Two different adaptations to this standard model (the NICD and the factor X models) are shown in the panels to the right to account for *Lfng* reporter dynamics (symbolized by a magnification glass and an oscillation trace) found in *Rbp-jk*<sup>-/-</sup> embryos and embryos treated with DAPT. In the NICD model (red, top row), NICD can activate *Lfng* and *Hes7* to a limited extent in the absence of RBP-J  $\kappa$  but the amount of NICD is not sufficient to maintain intercellular synchrony (indicated by shifted wave symbols above the gene/protein symbols), leading to dampening of collective oscillation amplitude of the *Lfng* reporter. In the factor X model (blue, bottom row), an unknown factor X drives expression in the absence of RBP-J  $\kappa$  but since NICD cannot transmit signals from neighboring cells, synchronization also gets lost gradually. DAPT treatment abolishes NICD, thus *bona fide* Notch target genes are not activated in the NICD model and oscillations decay rapidly after the pulse. Assuming that the influence of RBP-J  $\kappa$  as transcriptional repressor in the absence of NICD is stronger than the activating effect by X, the same result on dynamic level is produced by the factor X model. A hypothetical way to discriminate both models would be the combination of the *Rbp-jk*<sup>-/-</sup> genotype with DAPT treatment: The NICD model would predict a DAPT-like phenotype while the factor X model would predict a partial rescue of oscillations due to de-repression by the removal of RBP-J  $\kappa$ .



# Conclusion

How does the clock start ticking? In brief, this is the central question of my work on the onset of signaling oscillations in the mouse embryo presented in this thesis. The aim was to study signaling in the intact embryo by live imaging, taking full advantage of dynamic fluorescent signaling reporters that have been developed in recent years by our laboratory and others (Aulehla et al., 2008; Masamizu et al., 2006). The project consisted of two parts: first, the development of a method to enable long-term post-implantation embryo imaging, which I described in Chapter I, and second, the application of this method to the question of signaling pattern formation in Chapter II.

I managed to establish a post-implantation embryo imaging protocol yielding embryo development of close to *in utero* quality, on a so far unmatched timescale. Importantly, the system is reliable and with the newly developed multi-sample holder provides sufficient throughput to conduct large scale studies: More than 70 post-implantation embryos that directly contributed to the results shown here were imaged for more than 24 h and carefully analyzed in the course of this project. Methods like the customization of the Z.1 light-sheet microscope (Chapter I, 1.1 and 1.2) and the MEMO light-sheet multi-sample holder (Chapter I, 2.3) will improve embryo imaging studies in general. Bigger sample sizes allow more quantitative measurements and the distinction of finer details between experimental groups. Thus, reliable high-throughput imaging methods to-

gether with high-performance data handling and processing strategies will move the field of embryo imaging towards more efficient data collection and quantitative analysis with high statistical power. A bottleneck will remain the complex recovery and preparation of samples. This is why “high throughput” in the context of mammalian embryo imaging, especially post-implantation, refers to rather tens, not hundreds or thousands of samples for the near future.

Making extensive use of the post-implantation embryo live imaging method, I was able to compile a detailed picture of the early segmentation clock dynamics in the mouse. I managed to capture the onset of synchronous signaling oscillations and waves of the clock gene *Lfng* and was able to provide some mechanistic insight into these processes. Several fundamental questions were raised by the discovery of the pre-segment pulse, which may lead the way for further investigations:

I) Is the pulse required for subsequent waves? We hypothesized that the pulse may serve as synchronizer and pre-pattern for the following waves. In search for a method to selectively target the pulse, we discovered the independence of *Lfng* pulse expression from NICD, RBP-J  $\kappa$  and HES7, strongly suggesting that the signaling loops, as we know them for the PSM of later stage embryos undergoing somitogenesis, do not apply early on. This discovery leads to the second question:

II) What signals are responsible for pre-segment *Lfng* expression? The discovery of the pulse of *Dusp4* expression at the same time as the *Lfng* pre-segment pulse indicates the possibility of a functional link to FGF signaling. Moreover, the observation that *Dusp4* pulses in mesoderm and epiblast allows speculations on signaling across tissue layers. Evidence beyond correlations still has to be established on this topic and the hierarchy of putative *Lfng-Dusp4* interactions in the pre-segment stage needs to be clarified.

III) Apart from signaling details, the most fundamental question which had motivated this study in the first place still remains: How is initial synchrony achieved among cells? The descriptive approach of this work has helped to narrow down the remaining possibilities. We found no indication for gradual synchronization of independently oscillating cells. A global time setting by tissue ingression is also unlikely because of the slow and gradual nature of the gastrulation process. Other early synchronization events



upstream of *Lfng* or *Dusp4* expression cannot be excluded. Likewise, an arrangement with features of an excitable system with trigger waves is possible. Answering this central question of how synchrony is established will require the combination of different experimental approaches, including live imaging of genetic signaling mutants and embryos treated with pharmacological modulators, precise regional manipulations of imaged embryos e.g. by laser ablation or optogenetics as well as the study of synchronization behavior of gastrula cells *in vitro*.

In summary, the work presented in this thesis advanced our technical possibilities to observe post-implantation development in real-time and deepened our knowledge on signaling dynamics in a developmental period that has been difficult to access by imaging in the past. It laid the foundation to answer fundamental mechanistic questions, such as that on the onset of oscillation synchrony, in the early post-implantation embryo.



# Materials and methods

## 1. Animals

### 1.1 Mouse lines

Reporter alleles *LfngT2A*, *Dusp4T2A*, and *Axin2T2A*, which were not previously described, were generated with standard gene targeting techniques using R1 embryonic stem cells. *LfngT2A* alleles were generated by targeting the stop codon of the endogenous *Lfng* locus with a construct containing one neomycin selection cassette and two different reporter cassettes (3xVenus and 3xCherry), a NLS and a PEST sequence. Each reporter cassette consisted of three times the fluorescent protein sequence, linked with a short peptide sequence (GSAGS). FRT and loxP sites flanked the reporter cassettes in a way that Cre-mediated recombination yielded the *LfngT2A3xVenus* allele in which the selection cassette and the 3xCherry cassette were excised. In the final *LfngT2A3xVenus* allele the endogenous *Lfng* sequence is directly followed by a T2A sequence connected to the 3xVenus-NLS-PEST sequence (Fig. 13B). Similarly, FLP-mediated recombination removed the selection and 3xVenus cassettes, producing the *LfngT2A3xCherry* allele. A similar targeting strategy was used for *Dusp4T2A* and *Axin2T2A* alleles, yield-

ing *Dusp4T2A3xVenus* and *Axin2T2A3xVenus* alleles after Cre recombination. All mouse lines described above were generated at EMBL Heidelberg. The *LfngT2A* and *Dusp4T2A* lines were generated by Nobuko Tsuchida-Straeten, *Axin2T2A* lines were generated by Jana Kress and targeted embryonic stem cells were injected into blastocysts by Yvonne Peterson.

Following mouse lines used in this study were described previously:  $\beta$ -catenin<sup>lox(ex3)</sup> (Harada et al., 1999), Cre-ERT2 (Ventura et al., 2007; Jackson Laboratory, 008463), Floxed RBP-J (Han et al., 2002; RIKEN RBR, RBRC01071), *Hes7*-null (Bessho et al., 2001; RIKEN RBR, RBRC05983), *Hprt*-Cre (Tang et al., 2002; Jackson Laboratory, 004302), *LuVeLu* (Aulehla et al., 2008), *R26-H2BmCherry* (Abe et al., 2011; RIKEN CDB, CDB0239K), *R26R-Confetti* (Snippert et al., 2010; Jackson Laboratory, 017492), T-Cre (Perantoni and Lewandoski, 2005; IMSR, Tg(T-cre)1Lwd).

Complete deletion of *Rbp-jk* was achieved by mating Floxed RBP-J males with female *Hprt*-Cre mice. Mesoderm-specific expression of stabilized  $\beta$ -catenin in embryos was achieved by mating  $\beta$ -catenin<sup>lox(ex3)</sup> with T-Cre animals. The genotype of animals was verified by PCR.

All mouse lines were kept in an outbred background. Animals were housed in the EMBL animal facilities. All animal experiments were conducted under veterinarian supervision and after project approval by EMBL, following the guidelines of the European Commission, Directive 2010/63/EU and AVMA Guidelines 2007.

## 1.2 Genotyping

Tail tips (for genotyping adult mice) or whole embryos (for genotyping E6.5–8.5 embryos after ISH) were lysed in 50 mM NaOH (300  $\mu$ l for tail tips, 40  $\mu$ l for embryos) for 1 h at 95°C and neutralized afterwards with 1 M Tris-HCl (pH 5; 30  $\mu$ l for tail tips, 4  $\mu$ l for embryos). DNA samples were genotyped by PCR using OneTaq Quick-Load PCR mix (New England BioLabs, M0486S) according to the manufacturer's protocol.

The following genotyping primers were used (5'–3'): *Dusp4T2A3xVenus* forward GCCCGCCAAGGTCCCTAATC, wildtype reverse GGGGGCCGACTCTGGATTTG,

mutant reverse ACGCTGAACTTGTGGCCGTT, Axin2T2A3xVenus forward GTTCTCCATTGGCGAGATGT, wildtype reverse TCCCTCCCTAGGCTTTGTCT, mutant reverse ACGCTGAACTTGTGGCCGTT, LfngT2A wildtype forward CATCCTGTTGCTCCCAATGC, wildtype reverse CACACACATACACATAGCCCTGA, LfngT2A3xVenus mutant forward GCTCAAGCCGGCGATGGCTC, mutant reverse TTGGTCACCTTCAGCTTGG, LfngT2A3xCherry mutant forward TTGGTCACCTTCAGCTTGG, mutant reverse CAGATAGGTGCTAGCACCCC.

For all other lines the primers specified in the original publications were used (Materials and methods, 1.1).

## 2. Embryo methods

### 2.1 Embryo dissection and mounting for live imaging

Embryos were dissected in dissection medium (DMEM with 1 g L<sup>-1</sup> glucose, no phenol red, Thermo Fischer Scientific, 11880028, 15% FCS, 2 mM L-glutamine, 1x Penicillin-Streptomycin, 20 mM HEPES) as described previously (Rivera-Pérez et al., 2010). Before mounting, dissected embryos were washed once in washing medium (dissection medium without HEPES, pre-equilibrated in 5% CO<sub>2</sub>). Embryos were transferred to a drop of mounting agarose (1.8% low melting temperature agarose in Leibowitz's L-15 medium, Thermo Fischer, 41300021) on a heating plate (42°C). Each embryo was imbibed into a separate glass capillary (Brand, 701904) with a Teflon-tipped plunger (Brand, 701932). After allowing the agarose to harden for 5 min, the embryo was partially ejected, submerged in washing medium, and agarose was removed with dissection forceps leaving only the ectoplacental cone in agarose. Depending on the area of interest, embryos were mounted with the proximodistal axis either parallel (e.g. as in Fig. 9D,E) or perpendicular to the long axis of the capillary (as in Fig. 14A). Perpendicular mounting was used to examine the somite boundary formation on the distal tip of the

embryo. For transport to the light-sheet microscope, embryos were pulled back into the capillary with some medium.

## 2.2 Rotating bottle embryo culture

The general setup of rotating bottle embryo culture has been described elsewhere (New and Cockroft, 1979). Here, a rotating bottle incubator from BTC Engineering was used. Bottles were filled with 1.5 ml culture medium (Materials and methods, 3) and up to 10 embryos were placed in each bottle. Gas supply and composition during culture was identical to the microscope culture (Materials and methods, 3).

## 2.3 DAPT treatment experiments

DAPT (Sigma, D5942) was dissolved in DMSO and added to the embryo culture medium at 50  $\mu$ M concentration. Embryos were dissected at E6.5 and incubated over night in DAPT-containing culture medium (Materials and methods, 3) in the rotating bottle incubator. In the morning of E7, embryos were mounted for light-sheet imaging and further cultured and imaged in the microscope as described below (Materials and methods, 3) in fresh, DAPT-containing culture medium.

## 2.4 *In situ* hybridization

RNA ISH was performed as previously described (Wilkinson and Nieto, 1993) with the following published probes: *Msgn1* (Yoon et al., 2000), *Lfng* (Aulehla and Johnson, 1999), *Shh* (Echelard et al., 1993), *Uncx4.1* (Mansouri et al., 1997).

Embryos collected between E6.5 and E8.5 for ISH were staged based on morphological features according to Downs and Davies (1993).

### 3. Embryo culture system on the Z.1

#### *Parts design and manufacturing*

The embryo culture chamber, chamber frame, SPIMfor4 multi-sample holder, capillary caps and the MEMO sample holder concept were designed in SolidWorks (Dassault Systèmes) using CAD models of the Z.1 sample chamber and the sample holder disc for syringes as geometrical references (kindly provided by Carl Zeiss Microscopy GmbH). All parts were manufactured in the EMBL mechanical workshop, Heidelberg. Culture chamber and capillary caps were made from medical grade plastic (PEEK; KTK), SPIMfor4 sample holder and culture chamber frame from aluminum.

#### *Embryo culture chamber*

The culture chamber has a 180° window towards the illumination and detection objectives. A window on the back of the chamber allows monitoring of the sample during positioning with the camera mounted in the door of the Z.1 front system cavity. A 50 µm-thin FEP membrane (Katco) was glued around the three open sides of the culture chamber and a 11 mm round cover glass was glued into the window opening on the back side of the chamber using Silpuran 4200 biocompatible silicone glue (Wacker). The culture chamber was inserted into the chamber frame and both parts together were placed in the Z.1 sample chamber (Fig. 9B). With a screw on the back of the chamber frame the distance between front face of the culture chamber and the detection objective was adjusted to 0.5–1.0 mm.

#### *Perfusion system and temperature control*

An inlet and an outlet tube connected the embryo culture chamber with the perfusion system. A 0.7 x 1.7 mm (inner diameter; ID x outer diameter; OD) silicon tube (Pro Liquid, 4001015HG\_E) connected the chamber to a peristaltic tube pump (custom made) outside the Z.1 front system cavity. The medium was further pumped into a gas equilibration chamber (Fig. 9C) in which it was channeled through a coil of 140 cm thin-walled 0.7 x 1.1 mm (ID x OD) silicon tubing (Pro Liquid, 4001013HG). A thick-

walled, less gas permeable 1.3 x 3.00 mm (ID x OD) tube (Tygon; Pro Liquid, 3700015) carried medium back into the culture chamber.

The equilibration chamber was made from a 100 ml blue cap bottle (Duran). It was heated to 38°C with heating films (Telemeter Electronic, HKAP2x2R5.4L12) glued around the body of the bottle. Temperature was controlled with a temperature controller (Telemeter Electronic, TR12-G) and a Pt100 ceramic temperature probe (GHM-Greisinger, 602995) placed inside the equilibration chamber. The connecting tubes between equilibration chamber and embryo culture chamber were also heated by pumping warm water (40°C) through a spiral of tubing wrapped around them. The water was heated using the heating device Humidity S1 (Carl Zeiss Microscopy GmbH) that is usually used to preheat and humidify gas injected into the Z.1 sample chamber. The temperature sensor of the Z.1 sample chamber lies outside of the embryo culture chamber. Temperature inside the culture chamber was regularly checked. For a stable 37°C inside, the Z.1 temperature control was set to 38.0–38.5°C (depending on room temperature).

During experiments, medium was circulated at 0.5 ml min<sup>-1</sup>. During preparation, pumping was accelerated for quicker medium equilibration. Generally, starting the perfusion system 10 min before introducing embryos was enough to stabilize the pH inside the culture chamber (which depends on the CO<sub>2</sub> saturation).

### *Gas mix*

The equilibration chamber was fed with a defined gas mixture using an in-house developed gas mixer. E6.5 dissected embryos were first cultured with 6% O<sub>2</sub>, 8% CO<sub>2</sub> and 86% N<sub>2</sub> then O<sub>2</sub> was increased to 20% on day 7 while keeping CO<sub>2</sub> at 8%. E7.5 dissected embryos were directly cultured with 20% O<sub>2</sub>. A higher O<sub>2</sub> concentration increases the maturation rate of fluorescent proteins, resulting in a boost of fluorescent intensity and a better signal-to-noise ratio. To be able to detect the very first oscillations in LuVeLu embryos, O<sub>2</sub> had to be increased early morning on day 7, before the occurrence of the oscillations (Fig. 12F). 8% CO<sub>2</sub> were used because this concentration was measured to produce the desired pH of 7.4 inside the culture chamber.



### *Culture medium*

Prior to use in embryo culture, rat serum (male rats only; Envigo, S.R-0109D) was heat-inactivated for 30 min at 56°C and centrifuged at 20 000 x g for 1 h at 4°C to remove lipids which collect on the surface. Embryos dissected at E6.5, were cultured in 75% rat serum and 25% DMEM (DMEM with 1 g L<sup>-1</sup> glucose, no phenol red, 2 mM L-glutamine), supplemented with 1x Penicillin-Streptomycin. E7.5 dissected embryos were cultured in 50% rat serum, 50% DMEM, 1x Penicillin-Streptomycin. The culture chamber and perfusion system were filled with 3.8 ml culture medium. 200 µl mineral oil (Sigma, M8410) were layered on top of the medium inside the culture chamber to reduce evaporation. For DAPT treatment experiments on the microscope, mineral oil was omitted to prevent the lipophilic drug to preferentially dissolve in the oil. Instead, wet tissues were placed underneath the sample chamber to reduce evaporation.

### *Cleaning*

Cleaning of the culture chamber with FEP membrane was routinely done in an ultrasound bath with dish detergent first, then 70% ethanol and finally ddH<sub>2</sub>O, each treatment for 30 min. After 5–10 washes, the FEP membrane had to be replaced because of deteriorating optical properties. The perfusion system was flushed with water, 70% ethanol and water again after each experiment. Tubes were exchanged after drug experiments.

## **4. Light-sheet imaging**

All embryo live imaging experiments were done on the Lightsheet Z.1 (Carl Zeiss Microscopy GmbH) using a 20x 1.0NA Plan-Apochromat water immersion objective (Carl Zeiss Microscopy GmbH), sequential illumination with both light-sheets and 0.41x zoom. Images were taken with 1920 x 1920 pixels at 16-bit. 3D + time (3D+t) time-lapse datasets were generally recorded with 7.5 µm Z-spacing, 80–150 slices per sample, 300 ms exposure time and 12–20 min imaging interval (for imaging settings used

for *in toto* imaging and cell tracking, refer to Materials and methods, 6). Imaging intervals and laser intensities were adjusted to the age of the embryos as younger embryos showed generally a higher susceptibility to photodamage. The described imaging settings resulted in datasets of 100–440 GB per embryo, depending on the number of channels and duration of the experiment which was usually 20–40 h.

mVenus/Venus was routinely excited at 514 nm (50 mW internal laser power) and mCherry and RFP at 561 nm (20 mW internal laser power) or 514 nm if coexcited with Venus. Yellow and red fluorescence was detected with one camera each; the signal was split at 560 nm, narrowed with a 525/20 nm bandpass filter and a 585 nm longpass filter. For time-lapse experiments, LuVeLu<sup>+/-</sup> embryos were excited at 2.0–2.4% laser power, LuVeLu<sup>+/-</sup>;R26-H2BmCherry<sup>+/-</sup> double positive embryos were excited jointly at 514 nm, 2.0–2.4% power and fluorescence was imaged onto two cameras simultaneously. Some bleed-through of the Venus signal into the mCherry channel was evident but negligible because the mCherry channel was not used for quantitative data analysis. For LfngT2A3xVenus<sup>+/-</sup> live imaging, 2.8% laser power were used, snapshots of the *Lfng* expression domain at E6.5 were taken at 11.5% power and 120 ms exposure time, deviating from the standard settings described above. LfngT2A3xCherry<sup>+/+</sup> was excited at 7–8% laser power, Dusp4T2A3xVenus<sup>+/-</sup> and <sup>+/+</sup> at 2.4%, Axin2T2A3xVenus<sup>+/-</sup> and <sup>+/+</sup> at 3%. RFP of the R26R-Confetti<sup>+/-</sup> reporter was excited at 5% and 150 ms exposure time. For double reporter imaging of LfngT2A3xCherry with Dusp4T2A3xVenus or Axin2T2A3xVenus, fluorescence channels were recorded sequentially. To exclude that spectral bleed-through from the mCherry channel into the mVenus channel was responsible for the dynamics seen for *Dusp4*, I live-imaged gastrulating embryos only expressing Dusp4T2A3xVenus and could confirm the described pulse and gradient patterns.

## 5. Data analysis

Throughout the text, 3D image dimensions will be used as depicted in Fig. 9A and Fig. 11C: X=horizontal, perpendicular to the detection light path, Y=vertical, Z=horizontal, parallel to the detection light path.

## 5.1 Time series registration and embryo segmentation

### *Pre-processing*

Two images were acquired per image stack position with the two opposing light-sheets. During acquisition, both images were combined on the fly using a mean fusion algorithm provided with the microscope control and image processing software ZEN (Carl Zeiss Microscopy GmbH). For further processing, datasets were subsampled by a factor of two in X and Y to reduce data volume, also in ZEN.

### *Time series registration*

Rigid image registration (translation and rotation) of 3D+t datasets was done using an ImageJ/Fiji (Schindelin et al., 2012) script developed by Christian Tischer, providing a graphical user interface to the command line registration tool elastix (Klein et al., 2010; Shamonin et al., 2013). Registration was performed in a recursive manner: An initial reference time point was defined by the user. The transformation from the successive frame  $F_{n+1}$  to the reference frame  $F_n$  was calculated and applied to  $F_{n+1}$ . The resulting transformed frame served as new reference  $F_n$  for the transformation of the next  $F_{n+1}$  and so on. If the initial reference frame was not the first frame, the procedure was also propagated in the  $F_{n-x}$  direction. Loading and browsing of the large datasets before and after registration was done with an ImageJ plugin for streaming of Tiff and HDF5-based image stacks, also developed by Christian Tischer.

After registration, deviations of the embryo's proximodistal and anteroposterior axes from the Y and Z image axes, respectively, were adjusted, using an ImageJ macro I developed: Reorientation parameters were determined manually for a user-defined reference frame and subsequently applied globally to all time points. To cope with the large size of datasets, time points were loaded and processed sequentially.

### *Embryo segmentation*

Due to the drastic size and shape changes of the growing mouse embryo, morphological landmarks like the allantois or the position of segment formation change their absolute

position within the 3D+t dataset over time even after automatic registration. An additional step of landmark segmentation was performed to be able to follow relative positions in the embryo over time. The spatial extend of the LuVeLu/LfngT2A3xCherry-positive domain was manually marked with a rectangular bounding box in several reference frames of projections along Y and Z throughout the time series and the position and size change of the bounding box was linearly interpolated for the intermediate time points. This information was used to make intensity profiles and kymographs relative to the size of the *Lfng* expression domain.

## 5.2 Expression and oscillation dynamics

### *Transversal optical sections*

Transversal sections (XZ planes) of embryo 3D+t datasets were generated in Fiji. Sections were positioned relative to the manually segmented *Lfng* domain (Materials and methods, 5.1) for each time point at the relative proximodistal position specified in the figure legends (Fig. 12D; Fig. 18C). Each transversal section image represents a MIP of a 12  $\mu\text{m}$  thick slice through the embryo.

### *Kymographs and intensity profiles*

Intensity profiles and kymographs along the propagation direction of waves were generated in Fiji from spline curves in MIPs (projected along Y or Z) of 3D+t embryo datasets. For each time point, the spline curve was scaled and positioned relative to the manually segmented *Lfng* domain (Materials and methods, 5.1). MIPs were smoothed with a 2D Gaussian ( $\sigma=12 \mu\text{m}$ ) and intensity was averaged in a 25  $\mu\text{m}$ -wide corridor along the spline curve.

For horizontal line profiles in kymographs (along time; Fig. 12G; Fig. 17D–I), intensities in a 14  $\mu\text{m}$ -wide stripe were averaged. For normalized plots (Fig. 12G; Fig. 17D–F), profiles were processed with locally weighted scatter plot smoothing (LOWESS) in Matlab (Mathworks Inc.; bandwidth  $\alpha=0.06$ ), background was subtracted, and data was normalized to the maximum value. For de-trended plots (Fig. 17G–I), raw signal was

LOWESS-processed with a larger bandwidth ( $\alpha=0.18$ ) to remove oscillations but keep the low-frequency signal trend. The trend was subtracted from the raw signal and the resulting profiles were LOWESS-smoothed ( $\alpha=0.06$ ).

For vertical line profiles in kymographs (along space; Fig. 18G) intensities were averaged in a 14  $\mu\text{m}$ -wide stripe, background was subtracted, and data was normalized to the maximum value.

Kymographs of transversal optical sections were generated along a line from the center of the embryo to its periphery at a 45° angle in respect to the anteroposterior embryo axis (Fig. 18D,E; Fig. 19C). Intensity was averaged in a 35  $\mu\text{m}$ -wide corridor along the line. From these transversal section kymographs, intensity plots along time (Fig. 18F; Fig. 19D) were generated by plotting the maximum intensity value along the vertical (space) axis for each time point. Profiles were normalized and smoothed as described above for horizontal line profiles.

2D and 3D plots of intensity profiles over time (Fig. 20) were made in Matlab. Input kymographs were generated as described above and were smoothed again with a Gaussian over space ( $\sigma=17 \mu\text{m}$ ) and time ( $\sigma=10$  frames) for display.

*The following sections “Oscillation phase extraction”, “Phase Kymographs”, “Phase gradient slope, wave number  $q$  and oscillation periods”, and “Wave number computation from periods” were originally written by Gregor Mönke and are part of the manuscript draft Falk et al. (2017b), which was jointly written together with Alexander Aulehla and Gregor Mönke*

### *Oscillation phase extraction*

“To identify the oscillating, unsegmented LuVeLu-positive domain in kymographs, the sharp bright stripes marking the end of each wave in the distal embryo were used as a segmentation marker. For every time point in the kymographs, an interpolating spline was fitted to the corresponding intensity profile. To detect the distal intensity maxima, the zero-crossings of the first derivative of the splines were calculated. To filter out spurious low-intensity maxima outside of the domain of interest, these zero crossings were thresholded with the 25% quartile of the overall intensities of the respective kymograph.

The first detected maximum crossing the threshold when searching in proximodistal direction was taken as the result. This procedure was done for both distal domain limits present in a kymograph, yielding two boundary coordinates for every time point. These domain boundaries were subsequently smoothed in time with a moving average window of length 41 pixels. Finally, a binary mask specifying inside and outside of the segmented domain boundaries was constructed.”

### *Phase Kymographs*

“Phase extraction from the raw intensity kymographs was done using Wavelet transforms (Torrence et al., 1998). To remove low-frequency trends, every row (in the following called time-series) of a kymograph was convolved with a Sinc filter with a ‘cut-off-period’ of 240 min. Sinc filters are designed to be optimal low-pass filters in the frequency domain (Smith, 1997). The results from the convolution were then subtracted from the original time series. These de-trended time series were convolved with 100 complex Morlet Wavelets, scanning periods from 60 to 240 min. By tracing the power-maxima in the Wavelet spectra over time, the so called ‘ridges’ were identified. Evaluating the complex Wavelet transforms along the ridges gave a complex signal for every time series. Finally, by extracting the argument from these complex signals, the phase values over time were obtained. Re-stacking these phase-valued time series produced the phase kymographs. These were subsequently masked with the binary mask obtained from the procedure described in the paragraph above.”

### *Phase gradient slope, wave number $q$ and oscillation periods*

“The phases along a column of the masked phase kymographs were first unwrapped to obtain continuous phase values. The maximum of the unwrapped phases (the inflection point) was taken to identify the two proximodistal axes (in the following called phase profiles). An interpolating polynomial spline was then fitted to every phase profile. To prune out discontinuous phase jumps towards the distal end of the LuVeLu domain, the profiles were scanned for high first derivatives. An empirical threshold of 0.5 radians per pixel was taken as cut-off value. Finally, the average slope of the pruned phase profile spline was calculated to obtain the phase gradient slope. For the wave number  $q$ , the

respective phase difference between the maximal and minimal phase of the pruned phase profiles was calculated.

To calculate the distal periods in kymographs, the intensity values along the contour paths of the boundaries of the intensity mask were taken as input time series. To assure to be inside the oscillatory domain, the contour paths were shifted up or down towards the kymograph midline by 15 pixels. The intensities along the midline were taken as the proximal time series. These time series were subsequently analyzed by Wavelets as described above (*Phase Kymographs*). The periods were extracted along the maxima ridges of the Wavelet spectra.”

#### *Wave number computation from periods*

“The phase evolution of a non-autonomous phase oscillator can be written as:

$$\frac{d\varphi_{P,D}}{dt} = \omega_{P,D}(t) = \frac{2\pi}{T_{P,D}(t)}$$

Here  $\omega$  is the instantaneous angular frequency and  $T$  the instantaneous period, the subscripts denote proximal (P) and distal (D) respectively. After a spline interpolation of the measured periods (Fig. 14F) this differential equation can be solved via numerical quadrature. The wave number  $q$  is then given by the proximal-distal phase difference acquired over time:

$$q(t) = \frac{\varphi_P(t) - \varphi_D(t)}{2\pi} + q_0$$

The initial wavenumber  $q_0$  is computed from the initial measured phase difference.” (Falk et al., 2017b)

All computational steps described for phase kymograph generation and analysis were implemented in the Python programming language, making extensive use of the ‘SciPy’ library (Jones et al., 2001).

### *Temporal pulse profiles*

Temporal pulse delay measurements were done in Matlab from kymographs along the propagation direction of waves as described above (*Kymographs and intensity profiles*). Kymographs were smoothed with the LOWESS method (along space:  $\alpha=0.8$ , along time:  $\alpha=0.04$ ). For the time window of the peak, the intensity crest was determined (Fig. 15C). For each sample, the time difference between the crest position in the kymograph center (= proximal domain) and the average of the crest position at the intensity peaks above and below the midline (= distal domain) was calculated for control and DAPT-treated samples (Fig. 17J).

## **6. Mosaic labeling and single cell tracking**

Pregnant females carrying R26R-Confetti<sup>+/-</sup>;Cre-ERT2<sup>+/-</sup> embryos were injected with Tamoxifen (3 mg/40 g mouse; Sigma, T5648) dissolved in corn oil (Sigma, C8267) 15 h before dissection at E7.5. Single embryos were mounted on the Z.1 and imaged from three sides (left, right, posterior), with both light-sheets (no fusion on the fly), 3.7  $\mu\text{m}$  z-spacing, at 8 min interval for 15 h.

The six datasets (3 angles x 2 light-sheets) were subsampled by a factor two and fused using an algorithm developed by Marvin Albert based on the registration tool elastix. The fused 3D+t dataset was again subsampled by 0.6, converted from 16 to 8-bit and registered as described earlier (Materials and methods, 5.1). Subsequently, Ilastik (Sommer et al., 2011) was used to train a pixel classifier on the dataset to enhance cells as foreground objects. Object segmentation and tracking was then done with the spot creation wizard in Imaris 8 (Bitplane). Tracking was done using the Autoregressive Motion Model. Videos, figures and statistics were generated with Imaris (Fig. 10).



# Acknowledgements

I want to begin with thanking Alexander Aulehla, my supervisor who gave me the opportunity to earn my PhD in his group at EMBL Heidelberg. I am very grateful for his support throughout the ups and importantly also the downs of my time as PhD, for his trust, his guidance and his efforts to promote my development as responsible researcher.

Thanks to François Spitz and Christof Niehrs for support and advice throughout the development of my project as members of my thesis advisory committee and first and second referee of my thesis. Thanks to Lars Hufnagel as a member of my thesis advisory committee and examination committee and for his help with planning microscope component. His input was especially valuable on the design of multi-embryo holders for light-sheet microscopy. Thanks also to Alexis Maizel for being part of my examination committee.

Thanks to those I was lucky to collaborate with, namely Gregor Mönke, Christian Tischer and Marvin Albert for help and support with data processing and data analysis, Sonja Nowotschin for advice on mosaic cell labeling, and Katharina Sonnen for advice on sample mounting. I further want to thank all present and former members of the Aulehla Lab for the friendly atmosphere and good discussions. Thanks to Carina Vibe, Katharina Sonnen, Paul Gerald Sanchez, Emilia Esposito, Hidenobu Miyazawa and Nobuko Tsuchida-Straeten for their help with proofreading this thesis.

I want to express my gratitude to all members of Laboratory Animal Resources, the EMBL Mechanical Workshop, Electronic Workshop, and Scientific Instruments Maintenance for their support, especially Christian Kieser and Helmut Schaar for bigger and smaller, more or less last-minute solutions to embryo-culture related problems. I also want to use the opportunity to thank all EMBL staff from Kitchen Ladies over Purchase, Stores, Facility Management to Cafeteria and Canteen for being always friendly and extremely helpful—you all make EMBL such an awesome place to work at!

Thanks to all users of the Lightsheet Z.1, especially Laura Panavaite and Marvin for their patience and understanding when I excessively booked the microscope for weeks

in a row. Thanks to all friends and colleagues who made my time at EMBL a pleasant one. Thanks to Elisabeth Hillier and Anthi Papasavva for looking after the DB unit's coffee machine which fueled my work.

Thanks to the EMBL bike club for a good reason to leave work at 17:15 h on Wednesdays and the great experience of riding with you to Grenoble. Thanks to Matthias Helm-ling and Mikhail Savitski for the occasional Königsstuhl run.

I will certainly not forget to thank my parents and my sister for their incredible love and support throughout my life. It is great to know that I can count on you at any time.

I end with thanking Janne who has been an incredible support for me from setting up my thesis writing timeline to the extremely valuable discussion on my work in general and on the writing of the thesis—and beyond all this technical stuff I am just very glad we have each other.

# Supplementary movies

*Supplementary movies can be found on the enclosed CD. If not available, files can be requested directly from me. Please direct inquiries via email to [henning.falk@embl.de](mailto:henning.falk@embl.de).*

**Movie 1: Bright-field time-lapse movie following embryonic development from E6.5 for 40 h.** Movie related to the still frames shown in Fig. 9E. The embryo was cultured and imaged on the Z.1 light-sheet microscope using the customized culture and mounting methods described in this work. At 16:20 h the field of view was adjusted to account for the growth of the embryo. The video was captured with 20 min frame interval but is displayed with  $\sim 1$  h interval because image capture in several frames was compromised by a bug in the microscope software.

**Movie 2: *In toto* imaging of mosaic labeled Cre-ERT2;R26R-Confetti embryo at E7.5.** Movie related to images shown in Fig. 10A. RFP-whole cell fluorescence in the embryo is shown as MIP from three orientations: from the side (top left; anterior to the left), posterior (top right) and distal (bottom; anterior to the left). The embryo was recorded from three angles; the movie shows the dataset after fusion and registration.

**Movie 3: Cell tracking in a sparsely labeled Cre-ERT2;R26R-Confetti embryo.** Movie related to images shown in Fig. 10B,C. The movie shows in the left column the position of all cells (red spheres) segmented and tracked for  $>7$  h (side view at the top, distal view on the bottom; anterior to the left). Tracks are visualized as dragon tails for the last 20 time points and are color-coded according to the time color bar. In the right column the full tracks are overlaid with the enhanced cell signal after pixel classification. Cell trajectories in the anterior curve inwards, indicating the invagination of the forming head fold.

**Movie 4: LuVeLu;R26-H2BmCherry embryo from mid gastrulation to the first waves.** Movie related to the still frames shown in Fig. 12A. LuVeLu (cyan) and H2BmCherry (red) fluorescence is displayed as MIP from three orientations: from posterior (top left), the side (top right; anterior to the left) and distal (bottom; anterior down). Posterior view and side view were recorded separately, from different angles, the distal view shows the reoriented dataset recorded from posterior. At 12:00 h the  $O_2$  content in the culture environment was increased from 6 to 20% (Materials and methods, 3) resulting in a boost of fluorescence.

**Movie 5: The mesodermal expression pulse and very first LuVeLu oscillations.** Movie related to the kymograph shown in Fig. 12F. The embryo was imaged from LS stage onwards, LuVeLu fluorescence is displayed in cyan. The dataset was recorded from posterior and is shown as MIP from three orientations: from posterior (top left), the side (top right; anterior to the left) and distal (bottom; anterior down). The distortion of the embryo in the first few frames is an artefact of re-orientating the image stack to align the embryo to the image axes (Materials and methods, 5.1). Note the first, very faint oscillation occurring at 10:00 h.

**Movie 6: Early *Lfng* signaling dynamics monitored with the *LfngT2A3xVenus* knockin reporter.** Movie related to the still frames shown in Fig. 13C. *LfngT2A3xVenus* fluorescence (cyan) from EB stage onwards is displayed as MIP from three orientations: from posterior (top left), the side (top right; anterior to the left) and distal (bottom; anterior down). All views are generated from the same dataset which was recorded from posterior. The high autofluorescence of the VE partially masks the mesodermal pulse at the beginning of the movie.

**Movie 7: Somite boundary formation in relation to the first *LuVeLu* waves.** Movie related to images shown in Fig. 14A,B. *LuVeLu;R26-H2BmCherry* embryo (*LuVeLu*, cyan; *H2BmCherry*, red) was imaged from LB stage onwards and is displayed as MIP in distal orientation (anterior down). The embryo was mounted with its distal end facing the detection objective to have a good view on forming somites which become visible as clefts between nuclei.

**Movie 8: *LuVeLu* dynamics in control and *Hes7* knockout embryos.** Movie related to the kymographs shown in Fig. 16A,B. Recording of *LuVeLu* fluorescence (cyan) in a control embryo (left column) and a *Hes7<sup>-/-</sup>* embryo (right column), starting at MS stage. Embryos were recorded from posterior and are displayed as MIP from posterior (top row) and distal (bottom row). Similar to Movie 4,  $O_2$  was increased at 15:36 h resulting in a sudden increase of fluorescence. Note the complete absence of oscillations in the *Hes7<sup>-/-</sup>* embryo.

**Movie 9: *LuVeLu* dynamics in control, DAPT treated embryos and *Rbp-jk* knockout.** Movie related to the kymographs shown in Fig. 17A–C. *LuVeLu* fluorescence (cyan) is shown for a control embryo (left column) two different embryos treated with 50  $\mu$ M DAPT (middle columns), and an *Rbp-jk<sup>-/-</sup>* embryo (right column). Embryos were recorded starting at EB stage from posterior and are displayed as MIP from posterior (top row) and distal (bottom row). DAPT treated embryos were cultured in DAPT for a duration of 12 h prior to imaging and treatment was continued during imaging. Note the different degree of oscillation inhibition in the two embryos from the same experiment. The control and *Rbp-jk<sup>-/-</sup>* embryo were also imaged in the same experiment.

**Movie 10: Signaling dynamics in *Dusp4T2A3xVenus;LfngT2A3xCherry* double labeled embryos during pre-segment and early segment stages.** Movie related to the still frames shown in Fig. 18A,B. *LfngT2A3xCherry* (cyan) and *Dusp4T2A3xVenus* (red) fluorescence is shown as MIP from three orientations: from posterior (top left), the side (top right; anterior to the left) and distal (bottom; anterior down). Imaging starts at LS stage. Areas of co-expression of both reporters appear white with the chosen color maps as it is the case for the pre-segment pulse (4:00 h).

**Movie 11: Signaling dynamics in *Axin2T2A3xVenus;LfngT2A3xCherry* double labeled embryos during pre- and early segment stage.** Movie related to the still frames shown in Fig. 19A,B. *LfngT2A3xCherry* (cyan) and *Axin2T2A3xVenus* (red) fluorescence is shown as MIP from three orientations: from posterior (top left), the side (top right; anterior to the left) and distal (bottom; anterior down). Imaging starts at LS stage. The pre-segment pulse is visible at 6:00 h for the *Lfng* but not the *Axin2* reporter.

## Bibliography

- Abe, T., Kiyonari, H., Shioi, G., Inoue, K.-I., Nakao, K., Aizawa, S. and Fujimori, T.** (2011). Establishment of conditional reporter mouse lines at ROSA26 locus for live cell imaging. *Genesis* **49**, 579–590.
- Arnold, S. J. and Robertson, E. J.** (2009). Making a commitment: cell lineage allocation and axis patterning in the early mouse embryo. *Nat. Rev. Mol. Cell Biol.* **10**, 91–103.
- Arrenberg, A. B., Stainer, D. Y. R., Baier, H. and Huisken, J.** (2010). Optogenetic Control of Cardiac Function. *Science* **330**, 971–974.
- Aulehla, A. and Johnson, R. L.** (1999). Dynamic expression of lunatic fringe suggests a link between notch signaling and an autonomous cellular oscillator driving somite segmentation. *Dev. Biol.* **207**, 49–61.
- Aulehla, A. and Pourquié, O.** (2010). Signaling gradients during paraxial mesoderm development. *Cold Spring Harb. Perspect. Biol.* **2**, 1–18.
- Aulehla, A., Wehrle, C., Brand-Saberi, B., Kemler, R., Gossler, A., Kanzler, B. and Herrmann, B. G.** (2003). Wnt3a plays a major role in the segmentation clock controlling somitogenesis. *Dev. Cell* **4**, 395–406.
- Aulehla, A., Wiegraebe, W., Baubet, V., Wahl, M. B., Deng, C., Taketo, M., Lewandoski, M. and Pourquié, O.** (2008). A beta-catenin gradient links the clock and wavefront systems in mouse embryo segmentation. *Nat. Cell Biol.* **10**, 186–193.
- Beddington, R. S.** (1994). Induction of a second neural axis by the mouse node. *Development* **120**, 613–620.
- Bessho, Y., Sakata, R., Komatsu, S., Shiota, K., Yamada, S. and Kageyama, R.** (2001). Dynamic expression and essential functions of Hes7 in somite segmentation. *Genes Dev.* **15**, 2642–2647.
- Bessho, Y., Hirata, H., Masamizu, Y. and Kageyama, R.** (2003). Periodic repression by the bHLH factor Hes7 is an essential mechanism for the somite segmentation clock. *Genes Dev.* **17**, 1451–1456.
- Bone, R. A., Bailey, C. S. L., Wiedermann, G., Ferjentsik, Z., Appleton, P. L., Murray, P. J., Maroto, M. and Dale, J. K.** (2014). Spatiotemporal oscillations of Notch1, Dll1 and NICD are coordinated across the mouse PSM. *Development* **141**, 4806–4816.
- Boulet, A. M. and Capecchi, M. R.** (2012). Signaling by FGF4 and FGF8 is required for axial elongation of the mouse embryo. *Dev. Biol.* **371**, 235–245.
- Brückner, K., Perez, L., Clausen, H. and Cohen, S.** (2000). Glycosyltransferase activity of Fringe modulates Notch–Delta interactions. *Nature* **406**, 411–415.

- Cartharius, K., Frech, K., Grote, K., Klocke, B., Haltmeier, M., Klingenhoff, A., Frisch, M., Bayerlein, M. and Werner, T.** (2005). MatInspector and beyond: promoter analysis based on transcription factor binding sites. *Bioinformatics* **21**, 2933–2942.
- Chal, J. and Pourquié, O.** (2009). Patterning and differentiation of the vertebrate spine. In *The Skeletal System* (ed. Pourquié, O.), pp. 41–116. Cold Spring Harbor Laboratory Press.
- Chhetri, R. K., Amat, F., Wan, Y., Höckendorf, B., Lemon, W. C. and Keller, P. J.** (2015). Whole-animal functional and developmental imaging with isotropic spatial resolution. *Nat. Methods* **12**, 1171–1178.
- Christ, B. and Scaal, M.** (2008). Formation and differentiation of avian somite derivatives. *Adv. Exp. Med. Biol.* **638**, 1–41.
- Cole, S. E., Levorse, J. M., Tilghman, S. M. and Vogt, T. F.** (2002). Clock Regulatory Elements Control Cyclic Expression of Lunatic fringe during Somitogenesis. *Dev. Cell* **3**, 75–84.
- Conlon, R. A., Reaume, A. G. and Rossant, J.** (1995). Notch1 is required for the coordinate segmentation of somites. *Development* **121**, 1533–1545.
- Cooke, J. and Zeeman, E. C.** (1976). A clock and wavefront model for control of the number of repeated structures during animal morphogenesis. *J. Theor. Biol.* **58**, 455–476.
- Cox, G. and Sheppard, C. J. R.** (2004). Practical limits of resolution in confocal and non-linear microscopy. *Microsc. Res. Tech.* **63**, 18–22.
- de Luis Balaguer, M. A., Ramos-Pezzotti, M., Rahhal, M. B., Melvin, C. E., Johannes, E., Horn, T. J. and Sozzani, R.** (2016). Multi-sample Arabidopsis Growth and Imaging Chamber (MAGIC) for long term imaging in the ZEISS Lightsheet Z.1. *Dev. Biol.* **419**, 19–25.
- Del Barco Barrantes, I., Elia, A. J., Wünsch, K., Hrabe de Angelis, M., Mak, T. W., Rossant, J., Conlon, R. A., Gossler, A. and De la Pompa, J. L.** (1999). Interaction between Notch signalling and Lunatic fringe during somite boundary formation in the mouse. *Curr. Biol.* **9**, 470–480.
- Delaune, E. A., François, P., Shih, N. P. and Amacher, S. L.** (2012). Single-cell-resolution imaging of the impact of Notch signaling and mitosis on segmentation clock dynamics. *Dev. Cell* **23**, 995–1005.
- Dequéant, M.-L., Glynn, E., Gaudenz, K., Wahl, M., Chen, J., Mushegian, A. and Pourquié, O.** (2006). A complex oscillating network of signaling genes underlies the mouse segmentation clock. *Science* **314**, 1595–1598.
- Dias, A. S., de Almeida, I., Belmonte, J. M., Glazier, J. A. and Stern, C. D.** (2014). Somites Without a Clock. *Science* **343**, 791–795.
- Diez del Corral, R., Olivera-Martinez, I., Goriely, A., Gale, E., Maden, M. and Storey, K.** (2003). Opposing FGF and retinoid pathways control ventral neural pattern, neuronal differentiation, and segmentation during body axis extension. *Neuron* **40**, 65–79.

- Dovey, H. F., John, V., Anderson, J. P., Chen, L. Z., De Saint Andrieu, P., Fang, L. Y., Freedman, S. B., Folmer, B., Goldbach, E., Holsztynska, E. J., et al.** (2001). Functional gamma-secretase inhibitors reduce beta-amyloid peptide levels in brain. *J. Neurochem.* **76**, 173–181.
- Downs, K. M. and Davies, T.** (1993). Staging of gastrulating mouse embryos by morphological landmarks in the dissecting microscope. *Development* **118**, 1255–1266.
- Dubrulle, J., Mcgrew, M. J., Pourquie, O., Luminy, C. De and Cedex, M.** (2001). FGF Signaling Controls Somite Boundary Position and Regulates Segmentation Clock Control of Spatiotemporal Hox Gene Activation Julien. *Cell* **106**, 219–232.
- Dunty, W. C., Biris, K. K., Chalamalasetty, R. B., Taketo, M. M., Lewandoski, M. and Yamaguchi, T. P.** (2008). Wnt3a/beta-catenin signaling controls posterior body development by coordinating mesoderm formation and segmentation. *Development* **135**, 85–94.
- Echelard, Y., Epstein, D. J., St-Jacques, B., Shen, L., Mohler, J., McMahon, J. A. and McMahon, A. P.** (1993). Sonic hedgehog, a member of a family of putative signaling molecules, is implicated in the regulation of CNS polarity. *Cell* **75**, 1417–1430.
- Evrard, Y. A., Lun, Y., Aulehla, A., Gan, L. and Johnson, R. L.** (1998). Lunatic Fringe Is an Essential Mediator of Somite Segmentation and Patterning. *Nature* **394**, 377–381.
- Falk, H. J., Aulehla, A. and Hufnagel, L.** (2017a). A Sample Holder for Imaging a Plurality of Samples. Patent Application No. EP 17205938.8.
- Falk, H. J., Mönke, G. and Aulehla, A.** (2017b). *Manuscript in preparation.*
- Feller, J., Schneider, A., Schuster-Gossler, K. and Gossler, A.** (2008). Noncyclic Notch activity in the presomitic mesoderm demonstrates uncoupling of somite compartmentalization and boundary formation. *Genes Dev.* **22**, 2166–2171.
- Ferjentsik, Z., Hayashi, S., Dale, J. K., Bessho, Y., Herreman, A., De Strooper, B., Del Monte, G., De La Pompa, J. L. and Maroto, M.** (2009). Notch is a critical component of the mouse somitogenesis oscillator and is essential for the formation of the somites. *PLoS Genet.* **5**, e1000662.
- Filonov, G. S., Piatkevich, K. D., Ting, L.-M., Zhang, J., Kim, K. and Verkhusha, V. V.** (2011). Bright and stable near-infrared fluorescent protein for in vivo imaging. *Nat. Biotechnol.* **29**, 757–761.
- Galceran, J., Sustmann, C., Hsu, S.-C., Folberth, S. and Grosschedl, R.** (2004). LEF1-mediated regulation of Delta-like1 links Wnt and Notch signaling in somitogenesis. *Genes Dev.* **18**, 2718–2723.
- Gao, L., Shao, L., Chen, B.-C. and Betzig, E.** (2014). 3D live fluorescence imaging of cellular dynamics using Bessel beam plane illumination microscopy. *Nat. Protoc.* **9**, 1083–1101.
- Garcia, M. D., Udan, R. S., Hadjantonakis, A.-K. and Dickinson, M. E.** (2011). Live imaging of mouse embryos. *Cold Spring Harb. Protoc.* **2011**, pdb.top104.

- Giudicelli, F., Özbudak, E. M., Wright, G. J. and Lewis, J.** (2007). Setting the tempo in development: An investigation of the zebrafish somite clock mechanism. *PLoS Biol.* **5**, 1309–1323.
- Gomez, C., Özbudak, E. M., Wunderlich, J., Baumann, D., Lewis, J. and Pourquié, O.** (2008). Control of segment number in vertebrate embryos. *Nature* **454**, 335–339.
- Goodwin, B. C. and Cohen, M. H.** (1969). A phase-shift model for the spatial and temporal organization of developing systems. *J. Theor. Biol.* **25**, 49–107.
- Greger, K., Swoger, J. and Stelzer, E. H. K.** (2007). Basic building units and properties of a fluorescence single plane illumination microscope. *Rev. Sci. Instrum.* **78**, 23705.
- Hamburger, V. and Hamilton, H. L.** (1992). A series of normal stages in the development of the chick embryo. *Dev. Dyn.* **195**, 231–272.
- Han, H., Tanigaki, K., Yamamoto, N., Kuroda, K., Yoshimoto, M., Nakahata, T., Ikuta, K. and Honjo, T.** (2002). Inducible gene knockout of transcription factor recombination signal binding protein-J reveals its essential role in T versus B lineage decision. *Int. Immunol.* **14**, 637–645.
- Harada, N., Tamai, Y., Ishikawa, T. O., Sauer, B., Takaku, K., Oshima, M. and Taketo, M. M.** (1999). Intestinal polyposis in mice with a dominant stable mutation of the  $\beta$ -catenin gene. *EMBO J.* **18**, 5931–5942.
- Harima, Y., Takashima, Y., Ueda, Y., Ohtsuka, T. and Kageyama, R.** (2013). Accelerating the tempo of the segmentation clock by reducing the number of introns in the *Hes7* gene. *Cell Rep.* **3**, 1–7.
- Hayashi, S., Shimoda, T., Nakajima, M., Tsukada, Y., Sakumura, Y., Dale, J. K., Maroto, M., Kohno, K., Matsui, T. and Bessho, Y.** (2009). Sprout4, an FGF Inhibitor, Displays Cyclic Gene Expression under the Control of the Notch Segmentation Clock in the Mouse PSM. *PLoS One* **4**, e5603.
- Henrique, D., Abranches, E., Verrier, L. and Storey, K. G.** (2015). Neuromesodermal progenitors and the making of the spinal cord. *Development* **142**, 2864–2875.
- Hirata, H., Yoshiura, S., Ohtsuka, T., Bessho, Y., Harada, T., Yoshikawa, K. and Kageyama, R.** (2002). Oscillatory expression of the bHLH factor *Hes1* regulated by a negative feedback loop. *Science* **298**, 840–843.
- Hirata, H., Bessho, Y., Kokubu, H., Masamizu, Y., Yamada, S., Lewis, J. and Kageyama, R.** (2004). Instability of *Hes7* protein is crucial for the somite segmentation clock. *Nat. Genet.* **36**, 750–754.
- Holley, S. A., Jülich, D., Rauch, G.-J., Geisler, R. and Nüsslein-Volhard, C.** (2002). *Her1* and the Notch Pathway Function Within the Oscillator Mechanism That Regulates Zebrafish Somitogenesis. *Development* **129**, 1175–1183.
- Hori, K., Fostier, M., Ito, M., Fuwa, T. J., Go, M. J., Okano, H., Baron, M. and Matsuno, K.** (2004). *Drosophila deltex* mediates suppressor of Hairless-independent and late-endosomal activation of Notch signaling. *Development* **131**, 5527–5537.



- Horikawa, K., Ishimatsu, K., Yoshimoto, E., Kondo, S. and Takeda, H.** (2006). Noise-resistant and synchronized oscillation of the segmentation clock. *Nature* **441**, 719–723.
- Hoyle, N. P. and Ish-Horowicz, D.** (2013). Transcript processing and export kinetics are rate-limiting steps in expressing vertebrate segmentation clock genes. *Proc. Natl. Acad. Sci. U. S. A.* **110**, E4316–24.
- Hrabě de Angelis, M., McIntyre, J. and Gossler, A.** (1997). Maintenance of somite borders in mice requires the Delta homologue DII1. *Nature* **386**, 717–721.
- Hubaud, A.** (2016). Dynamique de la signalisation cellulaire au cours de la segmentation des Vertébrés.
- Hubaud, A. and Pourquié, O.** (2014). Signalling dynamics in vertebrate segmentation. *Nat. Rev. Mol. Cell Biol.* **15**, 709–721.
- Hubaud, A., Regev, I., Mahadevan, L. and Pourquié, O.** (2017). Excitable Dynamics and Yap-Dependent Mechanical Cues Drive the Segmentation Clock. *Cell* **171**, 1–15.
- Huisken, J. and Stainier, D. Y. R.** (2009). Selective plane illumination microscopy techniques in developmental biology. *Development* **136**, 1963–1975.
- Huisken, J., Swoger, J., Del Bene, F., Wittbrodt, J. and Stelzer, E. H. K.** (2004). Optical Sectioning Deep Inside Live Embryos by Selective Plane Illumination Microscopy. *Science* **305**, 1007–1009.
- Huppert, S. S., Hagan, M. X. G., De Strooper, B. and Kopan, R.** (2005). Analysis of notch function in presomitic mesoderm suggests a gamma-secretase-independent role for presenilins in somite differentiation. *Dev. Cell* **8**, 677–688.
- Ichikawa, T., Nakazato, K., Keller, P. J., Kajiura-Kobayashi, H., Stelzer, E. H. K., Mochizuki, A. and Nonaka, S.** (2013). Live imaging of whole mouse embryos during gastrulation: migration analyses of epiblast and mesodermal cells. *PLoS One* **8**, e64506.
- Ishimatsu, K., Takamatsu, A. and Takeda, H.** (2010). Emergence of traveling waves in the zebrafish segmentation clock. *Development* **137**, 1595–1599.
- Ivanovitch, K., Temino, S. and Torres, M.** (2017). Live imaging of heart tube development in mouse reveals alternating phases of cardiac differentiation and morphogenesis. *bioRxiv*.
- Jiang, Y. J., Aerne, B. L., Smithers, L., Haddon, C., Ish-Horowicz, D. and Lewis, J.** (2000). Notch signalling and the synchronization of the somite segmentation clock. *Nature* **408**, 475–479.
- Jones, E., Oliphant, T., Peterson, P. and others** (2001). SciPy: Open source scientific tools for Python.
- Jones, E. A. V., Baron, M. H., Fraser, S. E. and Dickinson, M. E.** (2005). Dynamic in vivo imaging of mammalian hematovascular development using whole embryo culture. *Methods Mol. Med.* **105**, 381–394.

- Jouve, C., Imura, T. and Pourquie, O.** (2002). Onset of the segmentation clock in the chick embryo: evidence for oscillations in the somite precursors in the primitive streak. *Development* **129**, 1107–1117.
- Jülich, D., Chiaw, H. L., Round, J., Nicolaije, C., Schroeder, J., Davies, A., Van Bebber, F., Busch-Nentwich, E., Dahm, R., Frank, O., et al.** (2005). beamter/deltaC and the role of Notch ligands in the zebrafish somite segmentation, hindbrain neurogenesis and hypochord differentiation. *Dev. Biol.* **286**, 391–404.
- Kageyama, R., Masamizu, Y. and Niwa, Y.** (2007). Oscillator mechanism of notch pathway in the segmentation clock. *Dev. Dyn.* **236**, 1403–1409.
- Kaufmann, A., Mickoleit, M., Weber, M. and Huisken, J.** (2012). Multilayer mounting enables long-term imaging of zebrafish development in a light sheet microscope. *Development* **139**, 3242–3247.
- Keller, P. J., Schmidt, A. D., Wittbrodt, J. and Stelzer, E. H. K.** (2008). Reconstruction of zebrafish early embryonic development by scanned light sheet microscopy. *Science* **322**, 1065–1069.
- Kinder, S. J., Tsang, T. E., Wakamiya, M., Sasaki, H., Behringer, R. R., Nagy, A. and Tam, P. P. L.** (2001). The organizer of the mouse gastrula is composed of a dynamic population of progenitor cells for the axial mesoderm. *Development* **128**, 3623–3634.
- Klein, S., Staring, M., Murphy, K., Viergever, M. A. and Pluim, J.** (2010). elastix: A Toolbox for Intensity-Based Medical Image Registration. *IEEE Trans. Med. Imaging* **29**, 196–205.
- Koizumi, K., Nakajima, M., Yuasa, S., Saga, Y., Sakai, T., Kuriyama, T., Shirasawa, T. and Koseki, H.** (2001). The role of presenilin 1 during somite segmentation. *Development* **1402**, 1391–1402.
- Kopan, R. and Ilagan, M. X. G.** (2009). The Canonical Notch Signaling Pathway: Unfolding the Activation Mechanism. *Cell* **137**, 216–233.
- Kopell, N. and Howard, L. N.** (1973). Horizontal bands in the belousov reaction. *Science* **180**, 1171–1173.
- Krol, A. J., Roellig, D., Dequeant, M.-L., Tassy, O., Glynn, E., Hattem, G., Mushegian, A., Oates, A. C. and Pourquie, O.** (2011). Evolutionary plasticity of segmentation clock networks. *Development* **138**, 2783–2792.
- Krzic, U., Gunther, S., Saunders, T. E., Streichan, S. J. and Hufnagel, L.** (2012). Multiview light-sheet microscope for rapid in toto imaging. *Nat. Methods* **9**, 730–733.
- Kusumi, K., Sun, E. S., Kerrebrock, A. W., Bronson, R. T., Chi, D. C., Bulotsky, M. S., Spencer, J. B., Birren, B. W., Frankel, W. N. and Lander, E. S.** (1998). The mouse pudgy mutation disrupts Delta homologue Dll3 and initiation of early somite boundaries. *Nat. Genet.* **19**, 274–278.
- Kusumi, K., May, C. M. and Eckalbar, W. L.** (2013). A large-scale view of the evolution of amniote development: Insights from somitogenesis in reptiles. *Curr. Opin. Genet. Dev.* **23**, 491–497.

- Lauschke, V. M., Tsiairis, C. D., François, P. and Aulehla, A.** (2013). Scaling of embryonic patterning based on phase-gradient encoding. *Nature* **493**, 101–105.
- Lawson, K. A., Meneses, J. J. and Pedersen, R. A.** (1991). Clonal analysis of epiblast fate during germ layer formation in the mouse embryo. *Development* **113**, 891–911.
- Lewis, J.** (2003). Autoinhibition with Transcriptional Delay. *Curr. Biol.* **13**, 1398–1408.
- Lewis, J., Hanisch, A. and Holder, M.** (2009). Notch signaling, the segmentation clock, and the patterning of vertebrate somites. *J. Biol.* **8**, 44.
- Livet, J., Weissman, T. a, Kang, H., Draft, R. W., Lu, J., Bennis, R. a, Sanes, J. R. and Lichtman, J. W.** (2007). Transgenic strategies for combinatorial expression of fluorescent proteins in the nervous system. *Nature* **450**, 56–62.
- Lucitti, J. L., Jones, E. A. V, Huang, C., Chen, J., Fraser, S. E. and Dickinson, M. E.** (2007). Vascular remodeling of the mouse yolk sac requires hemodynamic force. *Development* **134**, 3317–3326.
- Mansouri, A., Yokota, Y., Wehr, R., Copeland, N. G., Jenkins, N. A. and Gruss, P.** (1997). Paired-related murine homeobox gene expressed in the developing sclerotome, kidney, and nervous system. *Dev. Dyn.* **210**, 53–65.
- Masamizu, Y., Ohtsuka, T., Takashima, Y., Nagahara, H., Takenaka, Y., Yoshikawa, K., Okamura, H. and Kageyama, R.** (2006). Real-time imaging of the somite segmentation clock: revelation of unstable oscillators in the individual presomitic mesoderm cells. *Proc. Natl. Acad. Sci. U. S. A.* **103**, 1313–1318.
- Mickoleit, M., Schmid, B., Weber, M., Fahrbach, F. O., Hombach, S., Reischauer, S. and Huisken, J.** (2014). High-resolution reconstruction of the beating zebrafish heart. *Nat. Methods* **11**, 919–922.
- Moloney, D. J., Panin, V. M., Johnston, S. H., Chen, J., Shao, L., Wilson, R., Wang, Y., Stanley, P., Irvine, K. D., Haltiwanger, R. S., et al.** (2000). Fringe is a glycosyltransferase that modifies Notch. *Nature* **406**, 369–375.
- Morales, A. V, Yasuda, Y. and Ish-Horowicz, D.** (2002). Periodic Lunatic fringe expression is controlled during segmentation by a cyclic transcriptional enhancer responsive to notch signaling. *Dev. Cell* **3**, 63–74.
- Moreno, T. A. and Kintner, C.** (2004). Regulation of segmental patterning by retinoic acid signaling during *Xenopus* somitogenesis. *Dev. Cell* **6**, 205–218.
- Morimoto, M., Takahashi, Y., Endo, M. and Saga, Y.** (2005). The Mesp2 transcription factor establishes segmental borders by suppressing Notch activity. *Nature* **435**, 354–359.
- Müller, M., v Weizsäcker, E. and Campos-Ortega, J. A.** (1996). Expression domains of a zebrafish homologue of the *Drosophila* pair-rule gene hairy correspond to primordia of alternating somites. *Development* **122**, 2071–2078.
- Nagai, T., Ibata, K., Park, E. S., Kubota, M., Mikoshiba, K. and Miyawaki, A.** (2002). A variant of YFP with fast and efficient maturation for cell-biological applications. *Nature* **20**, 1585–1588.

- Naiche, L. A., Holder, N. and Lewandoski, M.** (2011). FGF4 and FGF8 comprise the wavefront activity that controls somitogenesis. *Proc. Natl. Acad. Sci.* **108**, 4018–4023.
- Nakatsuji, N., Snow, M. H. and Wylie, C. C.** (1986). Cinemicrographic study of the cell movement in the primitive-streak-stage mouse embryo. *J. Embryol. Exp. Morphol.* **96**, 99–109.
- Nakayama, K., Satoh, T., Igari, A., Kageyama, R. and Nishida, E.** (2008). FGF induces oscillations of *Hes1* expression and Ras/ERK activation. *Curr. Biol.* **18**, R332–R334.
- New, D. A. and Cockroft, D. L.** (1979). A rotating bottle culture method with continuous replacement of the gas phase. *Experientia* **35**, 138–140.
- Niwa, Y., Masamizu, Y., Liu, T., Nakayama, R., Deng, C. X. and Kageyama, R.** (2007). The Initiation and Propagation of *Hes7* Oscillation Are Cooperatively Regulated by Fgf and Notch Signaling in the Somite Segmentation Clock. *Dev. Cell* **13**, 298–304.
- Niwa, Y., Shimojo, H., Isomura, A., González, A., Miyachi, H. and Kageyama, R.** (2011). Different types of oscillations in notch and Fgf signaling regulate the spatiotemporal periodicity of somitogenesis. *Genes Dev.* **25**, 1115–1120.
- Nowotschin, S., Ferrer-Vaquer, A. and Hadjantonakis, A.-K.** (2010). Imaging Mouse Development with Confocal Time-Lapse Microscopy. In *Methods in enzymology*, pp. 351–377.
- Oates, A. C. and Ho, R. K.** (2002). Hairy/E(spl)-related (Her) genes are central components of the segmentation oscillator and display redundancy with the Delta/Notch signaling pathway in the formation of anterior segmental boundaries in the zebrafish. *Development* **129**, 2929–2946.
- Oka, C., Nakano, T., Wakeham, A., de la Pompa, J. L., Mori, C., Sakai, T., Okazaki, S., Kawaichi, M., Shiota, K., Mak, T. W., et al.** (1995). Disruption of the mouse RBP-J kappa gene results in early embryonic death. *Development* **121**, 3291–3301.
- Okubo, Y., Sugawara, T., Abe-Koduka, N., Kanno, J., Kimura, A. and Saga, Y.** (2012). *Lfng* regulates the synchronized oscillation of the mouse segmentation clock via trans-repression of Notch signalling. *Nat. Commun.* **3**, 1–9.
- Ozbudak, E. M. and Lewis, J.** (2008). Notch signalling synchronizes the zebrafish segmentation clock but is not needed to create somite boundaries. *PLoS Genet.* **4**, e15.
- Palmeirim, I., Henrique, D., Ish-Horowicz, D. and Pourquié, O.** (1997). Avian hairy gene expression identifies a molecular clock linked to vertebrate segmentation and somitogenesis. *Cell* **91**, 639–648.
- Pantazis, P. and Supatto, W.** (2014). Advances in whole-embryo imaging: a quantitative transition is underway. *Nat. Rev. Mol. Cell Biol.* **15**, 327–339.
- Perantoni, A. O. and Lewandoski, M.** (2005). Inactivation of FGF8 in early mesoderm reveals an essential role in kidney development. *Development* **132**, 3859–3871.

- Peterson, D. A.** (2010). Confocal Microscopy. In *Encyclopedia of Movement Disorders*, pp. 250–252. Elsevier.
- Power, R. M. and Huisken, J.** (2017). A guide to light-sheet fluorescence microscopy for multiscale imaging. *Nat. Methods* **14**, 360–373.
- Pursglove, S. E. and Mackay, J. P.** (2005). CSL: A notch above the rest. *Int. J. Biochem. Cell Biol.* **37**, 2472–2477.
- Pyrgaki, C., Trainor, P., Hadjantonakis, A.-K. and Niswander, L.** (2010). Dynamic imaging of mammalian neural tube closure. *Dev. Biol.* **344**, 941–947.
- Quandt, K., Frech, K., Karas, H., Wingender, E. and Werner, T.** (1995). MatInd and MatInspector: new fast and versatile tools for detection of consensus matches in nucleotide sequence data. *Nucleic Acids Res.* **23**, 4878–4884.
- Richardson, M. K., Allen, S. P., Wright, G. M., Raynaud, A. and Hanken, J.** (1998). Somite number and vertebrate evolution. *Development* **125**, 151–160.
- Riedel-Kruse, I. H., Müller, C. and Oates, A. C.** (2007). Synchrony dynamics during initiation, failure, and rescue of the segmentation clock. *Science* **317**, 1911–1915.
- Rivera-Pérez, J. A., Jones, V. and Tam, P. P. L.** (2010). Culture of whole mouse embryos at early postimplantation to organogenesis stages: developmental staging and methods. *Methods Enzymol.* **476**, 185–203.
- Rizzo, M. A. and Piston, D. W.** (2005). High-contrast imaging of fluorescent protein FRET by fluorescence polarization microscopy. *Biophys. J.* **88**, L14–L16.
- Ross, J., Müller, S. C. and Vidal, C.** (1988). Chemical Waves. *Science* **240**, 460–465.
- Saga, Y. and Takeda, H.** (2001). The making of the somite: molecular events in vertebrate segmentation. *Nat. Rev. Genet.* **2**, 835–845.
- Sakai, Y., Meno, C., Fujii, H., Nishino, J., Shiratori, H., Saijoh, Y., Rossant, J. and Hamada, H.** (2001). The retinoic acid-inactivating enzyme CYP26 is essential for establishing an uneven distribution of retinoic acid along the antero-posterior axis within the mouse embryo. *Genes Dev.* **15**, 213–225.
- Sauer, M. and Heilemann, M.** (2017). Single-Molecule Localization Microscopy in Eukaryotes. *Chem. Rev.* **117**, 7478–7509.
- Sawada, A., Shinya, M., Jiang, Y. J., Kawakami, A., Kuroiwa, A. and Takeda, H.** (2001). Fgf/MAPK signalling is a crucial positional cue in somite boundary formation. *Development* **128**, 4873–4880.
- Schindelin, J., Arganda-Carreras, I., Frise, E., Kaynig, V., Longair, M., Pietzsch, T., Preibisch, S., Rueden, C., Saalfeld, S., Schmid, B., et al.** (2012). Fiji: an open-source platform for biological-image analysis. *Nat. Methods* **9**, 676–682.
- Schmid, B., Shah, G., Scherf, N., Weber, M., Thierbach, K., Campos, C. P., Roeder, I., Aanstad, P. and Huisken, J.** (2013). High-speed panoramic light-sheet microscopy reveals global endodermal cell dynamics. *Nat. Commun.* **4**, 2207.
- Schröter, C., Herrgen, L., Cardona, A., Brouhard, G. J., Feldman, B. and Oates, A. C.** (2008). Dynamics of zebrafish somitogenesis. *Dev. Dyn.* **237**, 545–553.

- Serth, K., Schuster-Gossler, K., Cordes, R. and Gossler, A. (2003). Transcriptional oscillation of Lunatic fringe is essential for somitogenesis. *Genes Dev.* **17**, 912–925.
- Shamonin, D. P., Bron, E. E., Lelieveldt, B. P. F., Smits, M., Klein, S. and Staring, M. (2013). Fast parallel image registration on CPU and GPU for diagnostic classification of Alzheimer’s disease. *Front. Neuroinform.* **7**, 1–15.
- Shcherbo, D., Shemiakina, I. I., Ryabova, A. V., Luker, K. E., Schmidt, B. T., Souslova, E. A., Gorodnicheva, T. V., Strukova, L., Shidlovskiy, K. M., Britanova, O. V., et al. (2010). Near-infrared fluorescent proteins. *Nat. Methods* **7**, 827–829.
- Shu, X., Royant, A., Lin, M. Z., Aguilera, T. A., Lev-Ram, V., Steinbach, P. A. and Tsien, R. Y. (2009). Mammalian expression of infrared fluorescent proteins engineered from a bacterial phytochrome. *Science* **324**, 804–807.
- Siedentopf, H. and Zsigmondy, R. (1902). Über Sichtbarmachung und Größenbestimmung ultramikroskopischer Teilchen, mit besonderer Anwendung auf Goldrubingläser. *Ann. Phys.* **315**, 1–39.
- Sierra, J., Yoshida, T., Joazeiro, C. A. and Jones, K. A. (2006). The APC tumor suppressor counteracts beta-catenin activation and H3K4 methylation at Wnt target genes. *Genes Dev.* **20**, 586–600.
- Smith, S. W. (1997). *The Scientist and Engineer’s Guide to Digital Signal Processing*. San Diego, CA, USA: California Technical Publishing.
- Snippert, H. J., van der Flier, L. G., Sato, T., van Es, J. H., van den Born, M., Kroon-Veenboer, C., Barker, N., Klein, A. M., van Rheenen, J., Simons, B. D., et al. (2010). Intestinal crypt homeostasis results from neutral competition between symmetrically dividing Lgr5 stem cells. *Cell* **143**, 134–144.
- Solnica-Krezel, L. and Sepich, D. S. (2012). Gastrulation: Making and Shaping Germ Layers. *Annu. Rev. Cell Dev. Biol.* **28**, 687–717.
- Sommer, C., Straehle, C., Kothe, U. and Hamprecht, F. A. (2011). Ilastik: Interactive learning and segmentation toolkit. In *2011 IEEE International Symposium on Biomedical Imaging: From Nano to Macro*, pp. 230–233. IEEE.
- Sonnen, K. F. and Aulehla, A. (2014). Dynamic signal encoding-From cells to organisms. *Semin. Cell Dev. Biol.* **34**, 91–98.
- Sonnen, K. F., Lauschke, V. M., Franke, J., Falk, H. J., Petersen, Y., Funk, M. C., Beaupeux, M., Francois, P., Merten, C. A. and Aulehla, A. (2017). Control of mesoderm segmentation by phase-shifted Wnt- and Notch-signalling oscillations. Manuscript in press.
- Soroldoni, D., Jörg, D. J., Morelli, L. G., Richmond, D. L., Schindelin, J., Jülicher, F. and Oates, A. C. (2014). A Doppler effect in embryonic pattern formation. *Science* **345**, 222–225.
- Souilhol, C., Cormier, S., Tanigaki, K., Babinet, C. and Cohen-Tannoudji, M. (2006). RBP-J $\kappa$ -dependent Notch signaling is dispensable for mouse early embryonic development. *Mol. Cell. Biol.* **26**, 4769–4774.

- Stelzer, E. H. K.** (2015). Light sheet fluorescence microscopy for quantitative biology. *Nat. Methods* **12**, 23–26.
- Strnad, P., Gunther, S., Reichmann, J., Krzic, U., Balazs, B., de Medeiros, G., Norlin, N., Hiragi, T., Hufnagel, L. and Ellenberg, J.** (2016). Inverted light-sheet microscope for imaging mouse pre-implantation development. *Nat. Methods* **13**, 139–142.
- Strobl, F. and Stelzer, E. H. K.** (2014). Non-invasive long-term fluorescence live imaging of *Tribolium castaneum* embryos. *Development* **141**, 2331–2338.
- Szymczak, A. L., Workman, C. J., Wang, Y., Vignali, K. M., Dilioglou, S., Vanin, E. F. and Vignali, D. A. A.** (2004). Correction of multi-gene deficiency in vivo using a single “self-cleaving” 2A peptide-based retroviral vector. *Nat. Biotechnol.* **22**, 589–594.
- Takahashi, Y., Koizumi, K., Takagi, A., Kitajima, S., Inoue, T., Koseki, H. and Saga, Y.** (2000). *Mesp2* initiates somite segmentation through the Notch signalling pathway. *Nat. Genet.* **25**, 390–396.
- Takashima, Y., Ohtsuka, T., González, A., Miyachi, H. and Kageyama, R.** (2011). Intronic delay is essential for oscillatory expression in the segmentation clock. *Proc. Natl. Acad. Sci. U. S. A.* **108**, 3300–3305.
- Tam, P. P. L.** (1981). The control of somitogenesis in mouse embryos. *J. Embryol. Exp. Morphol.* **65**, 103–128.
- Tam, P. P. L.** (1998). Postimplantation mouse development: whole embryo culture and micro-manipulation. *Int. J. Dev. Biol* **42**, 895–902.
- Tam, P. P. L. and Beddington, R. S.** (1987). The formation of mesodermal tissues in the mouse embryo during gastrulation and early organogenesis. *Development* **99**, 109–126.
- Tam, P. P. L. and Behringer, R. R.** (1997). Mouse gastrulation: the formation of a mammalian body plan. *Mech. Dev.* **68**, 3–25.
- Tam, P. P. L. and Gad, J. M.** (2004). Gastrulation in the mouse embryo. In *Gastrulation: From Cells to Embryo* (ed. Stern, C. D.), pp. 233–262. Cold Spring Harbour, New York: Cold Spring Harbor Laboratory Press.
- Tang, S. H. E., Silva, F. J., Tsark, W. M. K. and Mann, J. R.** (2002). A Cre/loxP-deleter transgenic line in mouse strain 129S1/SvImJ. *Genesis* **32**, 199–202.
- Tomer, R., Khairy, K., Amat, F. and Keller, P. J.** (2012). Quantitative high-speed imaging of entire developing embryos with simultaneous multiview light-sheet microscopy. *Nat. Methods* **9**, 755–763.
- Torrence, C., Compo, G. P., Torrence, C. and Compo, G. P.** (1998). A Practical Guide to Wavelet Analysis. *Bull. Am. Meteorol. Soc.* **79**, 61–78.
- Tsiairis, C. D. and Aulehla, A.** (2016). Self-Organization of Embryonic Genetic Oscillators into Spatiotemporal Wave Patterns. *Cell* **164**, 656–667.
- Tzouanacou, E., Wegener, A., Wymeersch, F. J., Wilson, V. and Nicolas, J.-F.** (2009). Redefining the Progression of Lineage Segregations during Mammalian Embryogenesis by Clonal Analysis. *Dev. Cell* **17**, 365–376.

- Udan, R. S., Piazza, V. G., Hsu, C.-W., Hadjantonakis, A.-K. and Dickinson, M. E.** (2014). Quantitative imaging of cell dynamics in mouse embryos using light-sheet microscopy. *Development* **141**, 1–9.
- van Eeden, F. J., Granato, M., Schach, U., Brand, M., Furutani-Seiki, M., Haffter, P., Hammerschmidt, M., Heisenberg, C. P., Jiang, Y. J., Kane, D. A., et al.** (1996). Mutations affecting somite formation and patterning in the zebrafish, *Danio rerio*. *Development* **123**, 153–64.
- Ventura, A., Kirsch, D. G., McLaughlin, M. E., Tuveson, D. A., Grimm, J., Lintault, L., Newman, J., Reczek, E. E., Weissleder, R. and Jacks, T.** (2007). Restoration of p53 function leads to tumour regression in vivo. *Nature* **445**, 661–665.
- Vermot, J. and Pourquié, O.** (2005). Retinoic acid coordinates somitogenesis and left–right patterning in vertebrate embryos. *Nature* **435**, 215–220.
- Vettenburg, T., Dalgarno, H. I. C., Nylk, J., Coll-Lladó, C., Ferrier, D. E. K., Čížmár, T., Gunn-Moore, F. J. and Dholakia, K.** (2014). Light-sheet microscopy using an Airy beam. *Nat. Methods* **11**, 541–544.
- Voie, A. H., Burns, D. H. and Spelman, F. A.** (1993). Orthogonal-plane fluorescence optical sectioning: Three-dimensional imaging of macroscopic biological specimens. *J. Microsc.* **170**, 229–236.
- Wang, E., Babbey, C. M. and Dunn, K. W.** (2005). Performance comparison between the high-speed Yokogawa spinning disc confocal system and single-point scanning confocal systems. *J. Microsc.* **218**, 148–159.
- Weber, M. and Huiskens, J.** (2011). Light sheet microscopy for real-time developmental biology. *Curr. Opin. Genet. Dev.* **21**, 566–572.
- Wilkinson, D. G. and Nieto, M. A.** (1993). Detection of messenger RNA by in situ hybridization to tissue sections and whole mounts. *Methods Enzymol.* **225**, 361–373.
- Wolpert, L.** (1969). Positional information and the spatial pattern of cellular differentiation. *J. Theor. Biol.* **25**, 1–47.
- Wolpert, L.** (1971). Positional information and pattern formation. *Curr. Top. Dev. Biol.* **6**, 183–224.
- Yoon, J. K., Moon, R. T. and Wold, B.** (2000). The bHLH class protein pMesogenin1 can specify paraxial mesoderm phenotypes. *Dev. Biol.* **222**, 376–391.
- Zhang, N. and Gridley, T.** (1998). Defects in somite formation in lunatic fringe-deficient mice. *Nature* **394**, 374–377.



